Heriot-Watt University
School of Engineering and Physical Sciences

Peter Sebastian Benedek Szabo
M.Sc. Diplom-Wirtschafts.-Ing. (FH)

Heat transfer through thermomagnetic convection in magnetic fluids induced by varying magnetic fields

Thesis for the degree of Doctor of Philosophy in Mechanical Engineering
Institute of Mechanical, Process and Energy Engineering
Heriot Watt University, Edinburgh, UK
January 31, 2017

Author:	Peter S. B. Szabo
Registration number:	H00005642
Registration Date:	01.03.2013
Submission Date:	31.01.2017
Word Count:	49,999

First Academic Supervisor:	Dr. Wolf-Gerrit Früh School of Engineering and Physical Sciences Heriot-Watt University Edinburgh, United Kingdom
Second Academic Supervisor:	Dr. Yeaw Chu Lee School of Engineering and Physical Sciences Heriot-Watt University United Kingdom
Internal Examiner:	Dr. Tadhg O'Donovan School of Engineering and Physical Sciences Heriot-Watt University United Kingdom
External Examiner:	Dr. Alfonso Castrejóon-Pita Wadham College University of Oxford Oxford, United Kingdom

ACADEMIC REGISTRY

Research Thesis Submission

Name*:*	Peter Sebastian Benedek Szabo		
School:	School of Engineering and Physical Sciences		
Version: *(i.e. First, Resubmission, Final)*	Final	Degree Sought:	PhD in Mechnical Engineering

Declaration

In accordance with the appropriate regulations I hereby submit my thesis and I declare that:

1) the thesis embodies the results of my own work and has been composed by myself
2) where appropriate, I have made acknowledgement of the work of others and have made reference to work carried out in collaboration with other persons
3) the thesis is the correct version of the thesis for submission and is the same version as any electronic versions submitted*.
4) my thesis for the award referred to, deposited in the Heriot-Watt University Library, should be made available for loan or photocopying and be available via the Institutional Repository, subject to such conditions as the Librarian may require
5) I understand that as a student of the University I am required to abide by the Regulations of the University and to conform to its discipline.
6) I confirm that the thesis has been verified against plagiarism via an approved plagiarism detection application e.g. Turnitin.

* *Please note that it is the responsibility of the candidate to ensure that the correct version of the thesis is submitted.*

Signature of Candidate*:*		Date:	

Submission

Submitted By *(name in capitals):*	
Signature of Individual Submitting:	
Date Submitted:	

For Completion in the Student Service Centre (SSC)

Received in the SSC by *(name in capitals):*			
Method of Submission *(Handed in to SSC; posted through internal/external mail):*			
*E-thesis Submitted (**mandatory for final theses)***			
Signature:		Date:	

Please note this form should be bound into the submitted thesis.

Abstract

Magnetic fluid flow by thermomagnetic convection with and without buoyancy was studied in experiments and computational simulations. A mineral oil based ferro magnetic fluid was subjected to varying magnetic fields to induce thermomagnetic convection. As such fluids are mainly developed to increase heat transfer for cooling the fundamental effects on magnetic fluid flow was investigated using various magnetic field distributions. Computational simulations of natural and thermomagnetic convection are based on a Finite-Element technique and considered a constant magnetic field gradient, a realistic magnetic field generated by a permanent magnet and alternating magnetic fields. The magnetic field within the fluid domain was calculated by the magneto-static Maxwell equations and considered in an additional magnetic body force known as the Kelvin body force by numerical simulations. The computational model coupled the solutions of the magnetic field equations with the heat and fluid flow equations. Experiments to investigate thermomagnetic convection in the presence of terrestrial gravity used infrared thermography to record temperature fields that are validated by a corresponding numerical analysis. All configurations were chosen to investigate the response of the magnetic fluid to the applied body forces and their competition by varying the magnetic field intensity and its spatial distribution. As both body forces are temperature dependent, situations were analysed numerically and experimentally to give an indication of the degree by which heat transfer may be enhanced or reduced.

Results demonstrate that the Kelvin body force can be much stronger than buoyancy and can induce convection where buoyancy is not able to. This was evident in a transition area if parts of a fluid domain are not fully magnetically saturated. Results for the transition from natural convection to thermomagnetic convection suggest that the domain of influence of the Kelvin body force is aligned with the dominance of the respective body force. To characterise the transition a body force ratio of the Kelvin body force to buoyancy was developed that identified the respective driving forces of the convection cells. The effects on heat transfer was quantified by the Nusselt number and a suitable Rayleigh number. A modified Rayleigh number was used when both body forces were active to define an effective body force by taking the relative orientation of both forces into account. Results for the alternating magnetic field presented flow fields that altered with the frequency of the applied magnetic field but with varying amplitude. This affected the heat transfer that alternated with the frequency but failed to respond instantaneously and a phase lag was observed which was characterised by three different time scales.

Keywords: thermomagnetic convection, natural convection, magnetic fluid, Kelvin body force, magnetic Rayleigh number, modified Rayleigh number

Acknowledgements

This thesis was carried out between 2013 and 2017 at the Institute of Mechanical, Process and Energy Engineering, School of Engineering and Physical Sciences, Heriot-Watt University, Edinburgh, United Kingdom.

I would like to express my gratitude to Dr Wolf-Gerrit Früh my first supervisor. During this journey of my PhD I was very lucky to be supported by Wolf, a curios and very bright person. The constructive feedback and numerous conversation involved in the completion of this work was very beneficial not only in the preparation of this thesis but also to understand heat transfer processes within fluids. The kind support received and his great attitude made this journey to a very special privilege. I also would like to give a special thank you to my second supervisor Dr Yeaw Chu Lee. It was always a great pleasure to discuss new theories and ideas with you.

As a PhD scholar at Heriot-Watt University I was delighted to meet people around the world with different cultural backgrounds and was lucky to becomes friends of many. I am privileged to have received their support over 4 years. With the amount of friends found, it is impossible to enumerate all of them for their individual and special contribution. In terms of this I want to give a special thanks to the societies that showed me a world besides fluid dynamics, the Heriot-Watt Volleyball club, the Jets Volleyball club, the Cuban Salsa Society, the Committee of Early Career Researcher that I founded with the Head of Institute and the Konrad-Adenauer Fellows which I supported over their stay in Scotland made this experience very special. I also want to thank my formal teachers and colleagues which gave me support during my journey to be able to study abroad, Prof Stephan Sommer, Mrs Melanie Wenger, Mr Hartmut Hummel and Mr Rolf Lehmann.

This work was supported and funded by the Konrad-Adenauer Foundation with a stipend and a James-Watt fee waiver by Heriot-Watt University. The support received in computational facilities were provided by the Computational Engineering Research Laboratory at Heriot-Watt University and are gratefully acknowledged. I also want to acknowledge the staff of the University of Maribor, Slovenia that provided the facilities for the experiments. This results were essential to study and were very beneficial for this thesis. Especially, I want to express my gratitude to Dr Miloš Beković and his experience in ferrohydrodynamics. He made my stay a special experience and has turned from a colleague to a good friend.

I want to send my final words to Ilona Szabo that showed me a life besides my PhD and remembered me that there is so much else than research to discover. For the unconditional support and love received I am very grateful.

Edinburgh, 2017

Peter S. B. Szabo

Contents

List of Tables

List of Figures

Publications and presentations

Journal articles

1. Peter S. B. Szabo, Miloš Beković, Wolf-Gerrit Früh. Using infrared thermography to investigate thermomagnetic convection under spatial non-uniform magnetic field, International Journal of Thermal Sciences, 2017.

Proceedings

1. Peter S. B. Szabo, Wolf-Gerrit Früh, Enhanced and reduced natural convection using magnetic fluid in a square cavity, Proceedings in Applied Mathematics and Mechanics 16 (2016) 651-652

External presentations

1. Peter S. B. Szabo, Wolf-Gerrit Früh. Thermomagnetic convection under alternating magnetic fields. *88th GAMM Annual Meeting, Technical University of Ilmenau*, Ilmenau, 2017.

2. Wolf-Gerrit Früh, Peter S. B. Szabo, Michael Hoff, Thorsten Seelig. Identifying representative shapes in fields of temperature spectra in vacillating baroclinic waves. *EGU General Assembly 2017*

3. Peter S. B. Szabo, Yeaw-Chu Lee, Wolf-Gerrit Früh. Themomagnetic convection with alternating magnetic fields. *29th Scottish Fluid Mechanics Meeting, University of Edinburgh*, Edinburgh, 2016.

4. Wolf-Gerrit Früh, Peter S. B. Szabo, Michael Hoff, Thorsten Seelig. Spatial structure of local power spectra in Structural Vacillation in the baroclinic annulus. *29th Scottish Fluid Mechanics Meeting, University of Edinburgh*, Edinburgh, 2016.

5. Peter S. B. Szabo, Wolf-Gerrit Früh. Enhanced and suppressed natural convection using magnetic fluid in a square cavity. *Joint Annual Meeting of DMV and GAMM, Technical University of Brunswick*, Brunswick, 2016.

6. Wolf-Gerrit Früh, Peter S. B. Szabo, Michael Hoff, Thorsten Seelig. Transition to structual vacillation in the baroclinic annulus. *28th Scottish Fluid Mechanics Meeting, University of Glasgow*, Glasgow, 2015.

7. Peter S. B. Szabo, Wolf-Gerrit Früh. Enhancement and suppression of natural convection using a magnetic fluid in a square and cubic cavity. *28th Scottish Fluid Mechanics Meeting, University of Glasgow*, Glasgow, 2015.

8. Peter S. B. Szabo, Wolf-Gerrit Früh. Heat transfer enhancement with magnetic fluids in a 2D rectangular box. *27th Scottish Fluid Mechanics Meeting, University of St. Andrews*, St. Andrews, 2014.

Internal presentations

1. Peter S. B. Szabo, Wolf-Gerrit Früh. Heat transfer enhancement with magnetic fluids for cooling power transformers. *2nd IMPEE Internal Conference, Heriot-Watt University*, Edinburgh UK, 2014.

2. Peter S. B. Szabo, Miloš Beković, Wolf-Gerrit Früh. Using infrared thermography to investigate convection within magnetic fluids. *4th IMPEE Internal Conference, Heriot-Watt University*, Edinburgh UK, 2016.

1 Introduction

Commercial heat transfer fluids such as oil, water or ethylene glycol are primarily limited by their thermal conductivity for the development of energy efficient heat transfer fluids that is required in may industrial applications. With the capability to produce nano particles with a higher thermal conductivity and suspending them in a carrier fluid enables a new class of heat transfer fluids [1]. A great advantage of using nano fluids is not only the enhancement in thermal conductivity. With the dispersion of magnetic nano particles the nanofluid is equipped with a magnetic response that may additionally used to attract the fluid. Such nano fluids are magnetic fluids and the magnetic suspended nano particles follow Brownian motion. While the macroscopic magnetic fluid behaves as a homogeneous magnetisable fluid, it responds to magnetic fields. The Curie law states, that the magnetisation is inversely proportional to temperature and a net acceleration of colder, therefore higher magnetised fluid in the direction of the applied magnetic fluid is observed. This feature may be used to create thermomagnetic convection that increases heat transfer significantly.

The present thesis has analysed the fundamentals of thermomomagnetic convection for the use in heat transfer applications. For this purpose a commercial manufactured mineral oil based magnetic fluid with dispersed magnetite nano particles was used to investigate the features of thermomagnetic convection as a cooling fluid. The studies conducted computational simulations and experimental investigations via infrared thermogrpahy by considering the latest theories in ferrohydrodynamics. To numerical simulate the fluid flow under real conditions various fields distributions of realistic magnetic fields were considered and solved using the magneto-static Maxwell equations. The magnetic polarisation of the fluid was considered in an additional magnetic body force named the Kelvin body force and was calculated via Maxwell's equations and by using the respective the fluids properties.

1.1 Aims and Objectives

The main aim of this thesis studied the use of magnetic fluids in heat transfer applications especially with focus on the fundamental fluid behaviour in varying magnetic field distributions. Studying the fundamentals of magnetic convection such as natural and thermomagnetic convection lead to several objectives that need to be achieved to understand the complete phenomena observed in experiments and computations simulations.

The structure of the thesis was to characterise and analyse the thermomagnetic effects by considering the established theories to describe the resulting magnetic convection in

presence or absence of buoyancy. Chapter 2 gives a brief description of magnetic fluids, the preparation of magnetic nano particles with dispersion in a carrier fluid, the magnetisation of such fluids and their physical properties. Chapter 3 provides an overview of the current stage of research of thermomagnetic convection under various magnetic field distributions and their effect on heat transfer. The fundamental and numerical methods to study the theory of magnetic convection are introduced in Chapter 4 and the corresponding computational and experimental approach is described in Chapter 5. The contents of the following chapters are considered to analyse certain flow phenomena to fulfil several objectives of the thesis which are as follows:

I) Chapter 6 is used as a benchmark chapter. Here, a first analysis of heat transfer by convection using magnetic fluids is regular natural convection which is compared with thermomagnetic convection by computational simulation. This is followed by a combined natural and thermomagnetic convection case that characterises the effects of magnetic forces on natural convection. Here, the interactions of the Kelvin body force and buoyancy were analysed first by varying the intensity of the magnetic field that effect heat transfer significantly.

II) To give an indication of the effect of different boundary conditions such as temperature and direction of the spatial non-uniform magnetic field, experiments accompanied by computational simulation were carried out in Chapter 7. The realistic magnetic field provided by a permanent magnet indicated the possibility of enhanced or reduce heat transfer within application that exhibit electromagnetic fields. Following the computational models that were validated against experiments found the origin of enhanced and reduced heat transfer in the competing body forces with the respect of their different dependence on temperature under certain limitations.

III) Active or passive cooling of may electromagnetic applications involves the consideration of alternating magnetic fields. Chapter 8 provides a better understating of these processes when a magnetic fluid is used as a coolant and subjected to alternating magnetic fields. Thus, a parametric study was carried out to investigate the response of the magnetic fluid as a function of its temperature and viscous dissipation for a certain frequency range and different magnetic field intensities. The objective is to analyse the spatial time-varying alternating magnetic field and its effect on convective heat transfer induced by magnetic and gravitational forces.

Chapter 9 brings the theory, experiments and computational studies together into a global context and concludes the discussions and summaries provided by the individual chapters.

This is followed by Chapter 10 which presents aspects that need to considered in further analysing the potential of thermomagnetic convection for heat transfer application where magnetic fluids are used as coolant.

2 Magnetic fluids

Magnetic fluids are industrial manufactured colloidal suspensions of magnetic particles in a liquid and contain about 10^{23} particles per cubic metre. The single domain magnetic particles with an equivalent diameter of approximately 10 nm are coated with a dispersant to prevent coagulation and agglomeration by maintaining an adequate spacing between the magnetic particles. This provides colloidal stability when the particles are dispersed in a carrier fluid such as water, kerosene or a silicone based carrier fluid. As a result, the magnetic particles follow Brownian motion while the macroscopic fluid behaves as a homogeneous magnetisable fluid [2,3]. The following sections will give a brief introduction to the stability requirements, the preparation and the physical properties of magnetic fluids.

2.1 Colloidal stability requirements

Colloidal stability refers to a phenomenon of random continuous motion of small solid particles in a carrier fluid. It was first discovered by botanist Robert Brown in 1827 within water and named Brownian motion. The theory behind is based on translation kinetic energy caused by thermal agitation of molecules within a carrier fluid that is equally partitioned between particles. In general a colloidal suspension remains stable if any applied energy is smaller than the energy of Brownian motion and particles do not form agglomerates. The same applies to a colloidal magnetic fluid that is subjected to various field forces such as gravitation, magnetic fields and thermal forcing. It is therefore necessary to keep it stable to guarantee its best performance wherever it is used. For this purpose particle sedimentation and/or agglomeration must be avoided at all cost. To begin, it is useful to summarise the energy terms that are acting on a dispersed particle in a magnetic colloidal suspension and may be written as

$$\text{thermal energy} \qquad E_{th} = k_B T \tag{2.1}$$

$$\text{magnetic energy} \qquad E_m = \mu_0 M H V \tag{2.2}$$

$$\text{gravitational energy} \qquad E_g = \Delta\rho\, V g z \tag{2.3}$$

where $k_B = 1.384 \times 10^{-23}\mathrm{NmK}^{-1}$ is the Boltzmann's constant, T the temperature, $\mu_0 = 4\pi \times 10^{-7}\mathrm{Hm}^{-1}$ the vacuum permeability, M the magnetisation of the magnetic material, H the magnetic field, V the volume of a spherical particle of a diameter d, $\Delta\rho$ the density difference between the magnetic particle, ρ_s, and the carrier fluid, ρ_f, g the local acceleration due to terrestrail gravity and z the elevation in the gravitational field [2].

As each energy ratio to Brownian motion leads to a non-dimensional quantity it is more convenient to evaluate the maximum particle diameter, d_{max}, to keep colloidal stability. This is carried out in the remains of this section.

2.1.1 Stability in a gravitational field

Gravitational acceleration pulls all suspended particles downwards to create sedimentation. It is obvious that particles should not settle under the influence of gravity. An energy ratio may be written of thermal energy to gravitational energy to preserve colloidal stability by $k_B T/\left(\Delta\rho V g z\right)$. Hence, an equivalent diameter of a particle may be written as an upper limit to preserve stability by

$$d_{max} < \left(\frac{6k_B T}{\Delta\rho\, \pi g z}\right)^{1/3}. \tag{2.4}$$

However, the distribution of particles follow the barometric law in a state of thermodynamic equilibrium written as

$$n\left(z\right) \sim \exp\left[-\frac{\Delta\rho\, V g z}{k_B T}\right]. \tag{2.5}$$

Thus, the container must be sufficiently small so that concentration differences of gravitational origin within the fluid does not occur. The maximum height of the container may be written as

$$h_{max} < \frac{k_B T}{\Delta\rho g V}. \tag{2.6}$$

To preserve equilibrium distribution of colloidal particles within the container of height, h, the time t' must be very large such that the fluid remains stable over the life cycle $t < t'$. The magnitude of t' is a function of the diffusion coefficient, D, and the hight of the container, h, written as $t' = h^2/D$ where D is the diffusion coefficient of the suspended particle which is proportional to $k_B T/\left(\mu d\right)$ [4]. Numerical simulations and experiments for gravitational sedimentation were carried out by Bazhko and Tynjälä [5, 6] in a cylindrical magnetic fluid layer. The convective flow was studied by a numerical finite volume method using a two phase mixture of carrier fluid and solid nano particles having a size of approximately 10 nm. A single and two phase computational simulation of gravitational sedimentation was studied by Jafari et al. in 2008 [7, 8]. Results suggested that initial concentration gradients lead to oscillatory convection which increase with barometrical height of the container. The observed concentration gradients in the presence of a temperature gradient exceeded those of thermo-diffusion and have gravitational origins.

2.1.2 Stability in a magnetic field

External applied magnetic fields can cause phase separation of a magnetic fluid into magnetic particles and carrier fluid. A destabilisation of the magnetic fluid is the consequence as particles are dragged out of suspension towards higher magnetic field intensity. It is therefore necessary to avoid magnetic phase separation by evaluating a maximum equivalent diameter written as

$$d_{max} < \left(\frac{6 k_B T}{\mu_0 \pi M H} \right)^{1/3} \tag{2.7}$$

for a particle of a specific applied magnetic field intensity [2].

2.1.3 Stability against magnetic agglomeration

Magnetic particle agglomeration is in addition to gravity and magnetic phase separation a stability requirement due to the amount of suspended particles in the carrier fluid where inter-particle interactions are frequent. As particles are permanently magnetised it is necessary to know the energy to separate a pair of particles if they form agglomerates. To disrupt magnetic agglomeration the ratio of thermal agitation over dipole-dipole contact energy must be greater than unity. Following this a maximum equivalent diameter of

$$d_{max} < \left(\frac{72 k_B T}{\mu_0 \pi M^2} \right)^{1/3} \tag{2.8}$$

is developed to prevent magnetic agglomeration [2].

2.1.4 Stability against the van der Waals forces

Magnetic agglomeration is not the only possible case of particle agglomerates. Dipole-dipole interactions related to the van der Waals forces may combine particles to each other and form aggregates. The force arises spontaneously between neutral particles and is caused by quantum-mechanical interactions. Fortunately, there are ways to prevent agglomeration due to the van der Waals forces. Surfactants and the Steric repulsion mechanism method form long chain molecules and are used to prevent particles from approaching so close to one another that they cannot form aggregates [2,9]. The agglomeration of particles and their role in changing fluid properties were experimentally and theoretically studied by Charles and Odenbach [3,10].

2.2 Magnetic particles and their preparation

Magnetic particles are based on magnetic materials like ferrite or other metallic based chemical structures and are sensitive to magnetic fields. In general magnetic particles may be divided into two major groups such as ferrite particles and metal particles [11].

2.2.1 Ferrite nano particles

Ferrite nano particles such as magnetite (Fe_3O_4) and maghemite (γ-Fe_2O_3) are the most common magnetic particles. These particles are predominantly used in technological or biomedical applications and are dispersed in most commercial manufactured magnetic fluids. Details of magnetic properties and structure are given by [12–14]. The first ferrite particles were manufactured in 1965 by Papell [15]. The method was based on size reduction by wet-grinding in a ball-mill in the presence of a surfactant. However, this process takes up to 1,000 hours and has been, mainly for this reason, replaced by the co-precipitation method developed in 1974 by Khalafalla and Reimers for magnetite and maghemite [16]. The principle is based on a chemical reaction that removes a solute from a solution by adding a suitable substance. An example is the synthesis of Fe_3O_4 developed by Hariani et al. [17]. These methods are usually carried out between 0 and 100°C to establish a particle size of about 3 to 20 nm [11]. Other co-precipitation methods are used to produce suitable nano particles and are given by [13, 18–20]. A further method of creating ferrite nano particles is the micro-emulsion technique. This method is based on mixing aqueous solutions of metal salt or a mixture of metal salts with an aqueous solution of an alkali in the appropriate ratio [21, 22].

2.2.2 Metal nano particles

Metal particles such as iron or cobalt have two major advantage compared to ferrite particles. Firstly, metal particles can be produced more easily and, secondly, they have a higher saturation magnetisation. However, the disadvantage compared to ferrite particles must be considered as well. Subsequent loss of magnetic properties and the poor resistance to oxidation which has restricted their uses in most commercial applications are the major weakness. To achieve a good extended lifetime the particles can be maintained by an inert atmosphere. For the preparation of metal particles two major techniques are used. First the decomposition via thermolysis and second the inverse microemulsion technique. The decomposition by thermolysis of organometallic compounds is the most common, versatile and easiest method to produce metal particles for magnetic fluids [11]. Thomas [23], Hess and Packer [24] described a method in 1966 of preparing cobalt particles by thermoly-

sis. However, this process is relatively complex in terms of many parameters that need to be controlled. Therefore, this method was further developed in 1973 by Mailfert and Martinet [25] and 1978 by Chantrell et al. [26]. Thermolysis is also used to create cobalt and iron nano particles [27]. A great advance was the discovery by Papirer et al. [28, 29] which found a process where the surfactant was used as a catalyst for the decomposition to create cobalt nano particles. Pure nickel particles are produced via irradiation of nickel carbonyl with ultraviolet light which is shown by Hoon et al. [30]. Lambrick's [31] research demonstrated that it is possible to prepare magnetic fluids with mixed metals like Ni-Fe or Fe-Co via thermolysis. A combination of iron-nitride particles can be prepared either by plasma chemical vapour deposition reaction or vapour-liquid reaction [32, 33]. The second major technique of preparing metal nano particles is the inverse microemulsion technique and is similar to the microemulsion technique of the preparation of ferrite particles. The only difference is that the aqueous solution of an alkali is replaced by an emulsion containing a reduced agent such as sodium borohydride or sodium hypophosphite. An overview of the preparation of metal particles obtained in microemulsion such as Platinum, Cadmium, Palladium, Silver, Copper, Nickel and Gold is given by [34–36] and for the reduction of metal salts in aqueous solution by [11, 34, 37–40].

2.3 Magnetic fluid preparation

The essentials of magnetic fluid manufacturing are their stability requirements regarding the applied temperature, the applied magnetic field forces and/or gravity. In most applications chemical inertness of the carrier fluid and surfactant are desirable. For maintaining adequate flow properties low vapour pressure and low viscosity are appreciated [11]. A review of advantages and disadvantages of physical and chemical problems in magnetic fluids is given by Scholten [41].

2.3.1 Fluids containing ferrite particles

The preparation of magnetic fluids contains the stabilisation of ferrite colloids and their dispersion in a suitable carrier fluid. In general two methods are used to provide colloidal stability for ferrite particles. The surfactant coating with oleic acid is used to produce stable colloids for carrier fluids with low vapour pressure such as diesters [42], polyphenylesthers [43], silicone oils [44], hydrocarbons [16] perfluorocarbons and perfluoropolyethers [11]. For water based fluids a variety of secondary surfactants need to be added to achieve colloidal stability. Ionically-stabilized ferrite particles are used as an alternative method to surfactants. The principle is to charge the particles with low-

polarizing counter-ions that flocculate the ferrite surface to form small surface-charged stable ferrite colloids [20, 45]. Manufactured particles by those methods are macro-ions. A commercial manufactured magnetic fluid based on ferrite colloids has a saturation magnetisations in a range of 0.1 to 0.5 Tesla at 20°C depending on the volume concentration of dispersed particles [11].

2.3.2 Fluids containing metal particles

The stabilisation of metal particles in a suitable carrier fluid is a more complex task as ferrite particles. Using a manufacturing process of thermal decomposition for metal particles in the presence of a surfactant as a catalyst may not be compatible with the carrier fluid for a particular application. In addition the used surfactant can be removed prior to dispersion in a carrier fluid. Alternatively a second surfactant is used to achieve stable colloids in the carrier fluid of choice. The same problems are faced with the inverse-microemulsion and the reduction of metal salt in aqueous solutions particle manufacturing process. Magnetic fluids based on metal particles with a volume fraction between 10 to 20 % have saturation magnetisations of about 0.2 Tesla 20°C [11].

2.4 Fluid magnetisation

Magnetic fluids are analogues to paramagnetic materials. In the absence of magnetic fields the dispersed particles with a dipole moment[1], $\mathbf{m}$, form open-loop structures with no particular spatial orientation obeying Brownian motion. However, in the presence of a magnetic field the particles form long chains oriented along the magnetic field direction if the field intensity overcomes thermal agitation. The clustering and alignment of dispersed particles are presented in Fig. 2.1, left in the absence of a magnetic field and right in the presence of a magnetic field with an intensity of 1 Tesla in the vertical direction.

2.4.1 Equilibrium magnetisation model

In the following the magnetisation, $\mathbf{M}$, of a magnetic fluid is derived by using Langevin's classical theory to give the *superparamagnetisation law* with emphasis that inter-particle and fluid-particle interactions are negligible and magneto-dissipation does not occur [2]. The torque, $\delta\boldsymbol{\tau}$, acting on a magnetic particle with volume, δV, and magnetisation, $\mathbf{M}$, in the presence of a uniform magnetic field, $\mathbf{H}$, may be written as

$$\delta\boldsymbol{\tau} = \mu_0 \mathbf{M} \times \mathbf{H} \delta V \tag{2.9}$$

[1] with the dimension J·m/A

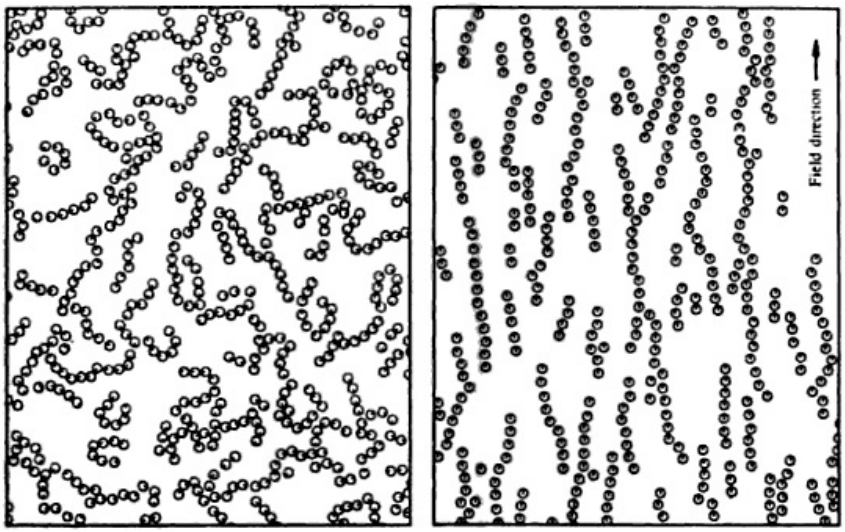

Figure 2.1: Monte Carlo simulation of dispersed magnetic particles left in absence of a magnetic field and right in presence of a magnetic field Fig. 1 in [46].

and its magnitude by

$$\tau = mH \sin\theta \tag{2.10}$$

where m is the magnetic dipole moment of a single magnetic particle and equals to $\mu_0 MV$ and θ the angle between the magnetic field, $\mathbf{H}$, and magnetisation, $\mathbf{M}$, of the magnetic particle [2]. To evaluate the energy that a particle expended by rotation the torque is integrated over angle θ taking a parallel alignment ($\theta = 0$) into account with

$$E_m = \int_0^\theta \tau \, \mathrm{d}\theta = mH \int_0^\theta \sin\theta \, \mathrm{d}\theta = mH \left(1 - \cos\theta\right). \tag{2.11}$$

In the absence of a magnetic field all dispersed particles are oriented in the configuration between the angles θ and $\theta + \mathrm{d}\theta$ and may be expressed with an angular distribution function of a quantity $n(\theta)$ for an assembly of N independent "rods" written as

$$n(\theta)\,\mathrm{d}\theta = N \frac{(2\pi \sin\theta)\,(\mathrm{d}\theta)}{4\pi\,(1)^2} = \frac{N}{2} \sin\theta \, \mathrm{d}\theta. \tag{2.12}$$

The probability of finding a given orientation of a magnetic particle within the colloidal suspension in the presence of an applied magnetic field at a given absolute temperature, T, is proportional to the Boltzmann factor $e^{(-E_m/k_B T)}$ so that the configuration of angle θ and $\theta + \mathrm{d}\theta$ may be written as

$$n(\theta)\,\mathrm{d}\theta \propto \frac{N}{4\pi} e^{-E_m/k_B T} 2\pi \sin\theta \, \mathrm{d}\theta = \frac{N}{2} e^{-E_m/k_B T} \sin\theta \, \mathrm{d}\theta. \tag{2.13}$$

To calculate the proportionality constant the number of rods need to be equal to N so that

$$N = \int_0^{\pi} n\left(\theta\right)\ \mathrm{d}\theta. \tag{2.14}$$

The effective dipole moment of a magnetic particle may be expressed as a vector component along the magnetic field direction written as $m\cos\theta$. For N rods the mean magnetic moment, $\overline{m}$, may be given from the distribution function in eq.(2.14) and may be written as

$$\overline{m} = \frac{\int_0^{\pi} m\cos\theta\, n\left(\theta\right)\ \mathrm{d}\theta}{\int_0^{\pi} n\left(\theta\right)\ \mathrm{d}\theta}. \tag{2.15}$$

By putting the resultant of the magnetic energy from eq.(2.11) into the eq.(2.13) and substituting $n\left(\theta\right)\ \mathrm{d}\theta$ into eq.(2.15) gives

$$\overline{m} = \frac{\int_0^{\pi} m\cos\theta e^{\zeta\cos\theta}\ \mathrm{d}\cos\theta}{\int_0^{\pi} e^{\zeta\cos\theta}\ \mathrm{d}\cos\theta} \tag{2.16}$$

where $\zeta = mH/k_BT$ presents the magnetic to thermal energy ratio. By carrying out the integration one obtains

$$\frac{\overline{m}}{m} = \coth\zeta - \frac{1}{\zeta} = \mathcal{L}\left(\zeta\right) \tag{2.17}$$

known as *Langevin's function* [2]. The magnitude of the magnetisation may be written as the total amount of magnetic moments of each dispersed magnetic particle in a unit volume of the mixture as

$$M = n\frac{\overline{m}}{\mu_0} \tag{2.18}$$

The saturation magnetisation, M_s, is given by the same principle for each magnetic particle with magnitude, m, by

$$M_s = n\frac{m}{\mu_0} \tag{2.19}$$

or by the saturation moment, M_d, of the bulk magnetic solid through the solid volume fraction, ϕ, by

$$M_s = \phi M_d. \tag{2.20}$$

Substituting ϕM_d in eq.(2.19) and combining eq.(2.17), (2.18) and (2.19) gives

$$M = \phi M_{\mathrm{d}}\mathcal{L}\left(\zeta\right), \quad \zeta = \frac{mH}{k_BT} = \frac{\pi}{6}\frac{\mu_0 M_d H d^3}{k_BT} \tag{2.21}$$

known as the *superparamagnetisation law* for a mono-dispersed colloidal magnetic fluid [2]. Assuming, the magnetisation vector, $\mathbf{M}$, for a mono-dispersed colloidal magnetic fluid[2] has the direction of the applied magnetic field one can calculate its magnitude as a function of the applied magnetic field intensity, the temperature and the solid volume fraction of dispersed magnetic particles as

$$\mathbf{M} = \frac{\mathbf{H}}{H} M\left(H, T, \phi\right). \tag{2.22}$$

Combining eq.(2.21) and eq.(2.22) one obtains the Langevin magnetisation vector

$$\mathbf{M} = \frac{\mathbf{H}}{H} \phi M_{\mathrm{d}} \mathcal{L}\left(\zeta\right). \tag{2.23}$$

As inter-particle interactions in a concentrated magnetic fluid are common, Pshenichnikov and Mekhonoshin [47, 48] performed an extension to eq.(2.23) written as

$$\mathbf{M_P} = \frac{\mathbf{H}}{H} \phi M_{\mathrm{d}} \mathcal{L}\left(\zeta_{\mathrm{p}}\right), \quad \zeta_{\mathrm{p}} = \frac{m\left(H + M/3\right)}{k_B T} \tag{2.24}$$

where ζ_{p} is the extended energy ratio of magnetic to thermal energy and M the Langevin magnetisation presented in eq.(2.21). It was proven to be more accurate than the traditional one-particle method where inter-particle interactions are neglected. However, this change in magnetisation also reflects on the initial Langevin susceptibility $\chi = nm^2/\left(3\mu_0 k_B T\right)$ and gives the following extended equation

$$\chi_P = \chi\left(1 + \chi/3\right) \tag{2.25}$$

where χ_P is the initial susceptibility after Pshenichnikov and Mekhonoshin.

2.4.2 Linearised magnetisation model

The magnetisation of a magnetic fluid may be expressed as a linearised function according to *Finlayson's equation of state* [49] extended by the variation in solid volume fraction

$$M = M^* + \left(\frac{\partial M}{\partial H}\right)_{T,\phi} (H - H^*) + \left(\frac{\partial M}{\partial T}\right)_{H,\phi} (T - T^*) + \left(\frac{\partial M}{\partial \phi}\right)_{H,T} (\phi - \phi^*) \tag{2.26}$$

where the superscript (*) denotes the values at the equilibrium state where the linearisation is performed. The variation in magnetisation due to the magnetic field intensity,

[2] By assuming that the magnetic fluid is free of inter-particle interactions and magneto-dissipation does not occur.

temperature and solid volume fraction may be derived from eq.(2.21) and written as

$$K \equiv \left(\frac{\partial M}{\partial T}\right)_{H,\phi} = -\phi M_d \frac{\zeta}{T}\left(1 - \coth^2(\zeta) + \frac{1}{\zeta^2}\right) \tag{2.27}$$

$$\chi \equiv \left(\frac{\partial M}{\partial H}\right)_{T,\phi} = \phi M_d \frac{\zeta}{H}\left(1 - \coth^2(\zeta) + \frac{1}{\zeta^2}\right) \tag{2.28}$$

$$\left(\frac{\partial M}{\partial \phi}\right)_{H,T} = M_d\left(\coth\zeta - \frac{1}{\zeta}\right) \tag{2.29}$$

where χ denotes the susceptibility and K is known as the pyromagnetic coefficient. A relative pyromagnetic coefficient, β_m, may be expressed by

$$\beta_m \equiv -\frac{1}{M}K \tag{2.30}$$

and presents the relative dependence of the magnetic fluid to temperature. In high magnetic fields where the fluid is close to saturation and far away from the Curie temperature the thermal expansion coefficient, β, of the magnetic fluid is determined as that of the carrier fluid [6, 50].

2.4.3 Magnetic relaxation

Magnetic relaxation can occur by two phenomena in which the magnetisation of a magnetic fluid relaxes after an applied initially magnetic field is removed. The first phenomenon is based on relaxation by particle rotation within the fluid and the second phenomenon occurs due to rotation of the magnetic vector within the particle [2].

The process of particle rotation caused by thermal agitation is characterised by a Brownian rotational diffusion time, τ_B, given by [51]

$$\tau_B = \frac{3V\mu}{k_B T} \tag{2.31}$$

where μ is the dynamic viscosity of the carrier fluid. In the presence of a magnetic field a rate of Brownian rotation relaxation is provided by the *Fokker-Planck equation* for a single-domain magnetic particle [52, 53].

The second relaxation mechanism is magnetic relaxation caused by Néel relaxation and occurs in single-domain uni-axial magnetic particles with a magnetisation that has two stable orientations anti parallel to each other along the easy axis. By overcoming an energy barrier given by $K_a V$ where, K_a is the anisotropy constant of the material, and fulfilling the condition of $K_a V \ll k_B T$, the magnetisation vector flips and reverse its

direction within the particle. The time between two induced magnetisation fluctuations is calculated by the Néel-Arrhenius written as [2, 54, 55]

$$\tau_N = \frac{1}{f_0}\exp\left(\frac{K_a V}{k_B T}\right) \tag{2.32}$$

where f_0 is a frequency having the value of approximately 10^9 Hz which was confirmed for a magnetic fluid by McNab et al. [56].

Brownian and Néel relaxation in magnetic fluids lead to a superparamagnetic behaviour and can be classified into two types of superparamagnetism. Extrinsic superparamagnetism exhibits a material when $\tau_B \ll \tau_N$ and the relaxation occurs by Brownian motion. For $\tau_N \ll \tau_B$ the material posses intrinsic superparamagnetism and Néel relaxation is dominat within the fluid. The transition between Brownian and Néel relaxation may be considered for a particle size with an equivalent diameter, d_e, for the condition $\tau_N = \tau_B$ [2].

2.5 Physical properties of magnetic fluids

As most magnetic fluids have limited information about their temperature dependent physical properties it is common to use a single phase model to estimate those by numerical approximation if experimental data are not available. The following section will demonstrate the numerical approach to estimate the density, specific heat capacity, thermal expansion coefficient, thermal conductivity and viscosity of a magnetic fluid where the solid dispersed particles are denoted with the subscript (s) and the carrier fluid as (f) respectively.

2.5.1 Density

The density of magnetic fluids may be estimated based on the volume fraction by

$$\rho = \phi\rho_s + (1-\phi)\,\rho_f \tag{2.33}$$

for temperature independent values [2], and is in line with [57–60].

2.5.2 Specific heat capacity

The effective specific heat capacity of a magnetic fluid may be estimated according to the same approach as the density based on the volume fraction of the fluid by

$$c_p = \phi c_{p_s} + (1 - \phi)\, c_{p_f} \tag{2.34}$$

and is in line with [57–62]. However, an alternative approach based on the heat capacity concept may be formulated [63, 64] as

$$c_p = \frac{\phi c_{p_s} \rho_s + (1 - \phi)\, c_{p_f} \rho_f}{\rho}. \tag{2.35}$$

As both formulations of an effective specific heat capacity lead to different results and due to a lack of experimental data, both formulations are considered equivalent in estimating an effective specific heat capacity of the magnetic fluid [65].

2.5.3 Thermal expansion coefficient

The thermal expansion coefficient of a magnetic fluid is developed after the same principle of the specific heat capacity and based on the mass fraction of the fluid [66] written as

$$\beta = \frac{\phi \rho_s \beta_s + (1 - \phi)\, \rho_f \beta_f}{\rho}. \tag{2.36}$$

2.5.4 Thermal conductivity

Low thermal conductivity in conventional heat transfer fluids such as oil, water and ethylene glycol are a primary limitation for the development of energy-efficient heat transfer which is required in may industrial and engineering applications. The capability to produce suspensions by adding nano particles with a higher thermal conductivity such as magnetic fluids in the early and mid 1960s added a new class of heat transfer fluids. A higher conductivity compared to currently used heat transfer fluids is the result that enhance heat transfer significantly. The improvement of thermal conductivity is measured by the ratio of the thermal conductivity of the magnetic fluid to the carrier fluid [1, 50]. An effective thermal conductivity of a magnetic fluid may be estimated by

$$k = \phi k_s + (1 - \phi)\, k_f. \tag{2.37}$$

As the thermal conductivity of magnetic fluids depends on various factors such as volume fraction, particle size, temperature, particle shape, carrier fluid, nano particle material,

Table 2.1: Fluid thermal conductivity models, estimated for simulations.

Model	Equation
Bruggeman [69]	$k = (3\phi - 1)\, k_s + [3\,(1-\phi) - 1]\, k_f + \sqrt{\Delta}$ $\Delta = (3\phi - 1)^2\, k_s^2 + [3\,(1-\phi) - 1]^2\, k_f^2 + 2\,[2 + 9\phi\,(1-\phi)]\, k_s k_f$
Chon and Kihm [70][3]	$k = k_f \left[1 + 64.7\phi^a \left(\frac{d_f}{d_p}\right)^b \left(\frac{k_s}{k_f}\right)^c \mathrm{Pr}^e\, \mathrm{Re}^g\right]$
Hamilton and Crosser [71]	$k = k_f \frac{k_s + 2k_f - 2\phi\left(k_f - k_s\right)}{k_s + 2k_f + \phi\left(k_f - k_s\right)}$
Jang and Choi [72]	$k = k_f\,(1-\phi) + k_s + 3C_1 \frac{d_f}{d_s} k_f \mathrm{Re}_{d_s}^2 \mathrm{Pr}\ \phi$
Koo and Kleinstreuer [73][4]	$k = k_f \frac{k_s + 2k_f - 2\phi\left(k_f - k_s\right)}{k_s + 2k_f + \phi\left(k_f - k_p\right)} + 5 \times 10^4 f_1\,(\phi)\, \phi_f c_{p_f} \sqrt{\frac{k_B T}{\rho d_p}} f_2\,(\phi, T)$
Maxwell-Garnett [74]	$k = k_f \frac{(1-\phi)\left(k_s + 2k_f\right) + 3\phi k_s}{(1-\phi)\left(k_s + 2k_f\right) + 3\phi k_f}$
Wasp [75]	$k = k_f \frac{k_s + 2k_f - 2\phi\left(k_f - k_s\right)}{k_s + 2k_f + \phi\left(k_f - k_p\right)}$

additives, pH, sonication and aggregation [67] and the absence or presence of magnetic fields [50] various models of estimating thermal conductivity were developed. The present thesis has used the above mixture model thermal conductivity to be consistent with the physical fluid property estimations of the other parameters and to be in line with [60]. Further estimation models of the thermal conductivity of magnetic fluids are presented in Tab. 2.1. In general, reports show a change of conductivity enhancement by 40 % to a 150 % enhancement [67, 68]. A more detailed review of thermal properties and conductivity enhancement of magnetic fluid is given by Philip and Shima [67] in 2012 and for the absence and the presence of magnetic fields by Nkurikiyimfura [50] in 2013. Magnetic fluids have due to their thermal properties a remarkable potential for heat transfer applications.

2.5.5 Viscosity

Magnetic fluids are liquids even when magnetised to saturation. However, the presence of magnetic fields affects the fluidity [2]. The difference in rheology in the absence and the presence of magnetic field forces are now introduced below.

[3] $a = 0.7460,\ b = 0.3690,\ c = 0.7476,\ e = 0.9955,\ g = 1.2321$

[4] functions f_1 and f_2 are found in the referenced work.

No magnetic field

Magnetic or non-magnetic colloids affect the viscosity when dispersed in a carrier fluid. The presence of particles increases the rate of energy dissipation so that the mixture viscosity of a colloidal suspension is grater than the carrier fluid viscosity. A relationship of the mixture's viscosity, μ, to carrier fluid viscosity, μ_f, may be written as

$$\mu = \mu_f \left(1 + \frac{5}{2}\phi\right) \tag{2.38}$$

by assuming a small particle concentration, ϕ, and no particle coating [76,77]. For higher concentrations eq.(2.38) may be extended to

$$\begin{aligned} \mu &= \frac{\mu_f}{1 + a\phi + b\phi^2} \\ \text{with} \quad a &= -\frac{5}{2}, \qquad b = -\frac{1 + a\phi_c}{{\phi_c}^2} \end{aligned} \tag{2.39}$$

where ϕ_c equals 0.74 and presents the particle concentration where the suspension becomes effectively rigid due to close packing of spheres [78]. Bear in mind that magnetic colloids with radius, r, are coated with a dispersant thickness of δ occupying a fraction of the fluid volume. The total volume concentration of the magnetic particle including the dispersant equals to $\phi' = \phi\,(1 + \delta/r)^3$ and eq.(2.39) may be written as

$$\mu = \frac{\mu_f}{1 + a\phi' + b\phi'^2}. \tag{2.40}$$

If colloids tend to cluster ϕ_c may be reduced from 0.74 [2].

In the presence of a magnetic field

In the presence of an external magnetic field an increase in viscous dissipation is noted [2]. The phenomenon is known as the magneto-viscous effect or also referred to as magneto-dissipation and was first discovered in 1968 by McTauge [79] and accompanied by Hall and Busenberg [80]. Magneto-viscous effects emerge out of the influence of shear flow where colloidal particles tend to rotate in the flow according to the mechanical torque produced by viscous friction and the presence of an external magnetic field that tends to align colloidal particles in the field direction. In other words, if the vorticity of the flow and the magnetic field direction are collinear the influence on an increase in viscosity does not appear. The situation changes if the vorticity of the flow and field direction are perpendicular. A torque produced by shear flow will misalign the magnetic particle

Table 2.2: Fluid Viscosity models, estimated for simulations.

Model	Equation
Batchelor [83]	$\mu = \mu_f \left(6.5\phi^2 + 2.5\phi + 1\right)$
Brinkman [84]	$\mu = \mu_f / \left(1-\phi\right)^{2.5}$
Brownian model [85][5]	$\mu = \mu_f \left(5.2\phi^2 + 2.5\phi + 1\right)$
[6]	$\mu = \mu_f \left[\left(5.2 + 0.97\right)\phi^2 + 2.5\phi + 1\right]$
Graham [86]	$\mu = \mu_f \left(\frac{4.5}{\frac{h}{d_p}\left(2+\frac{h}{d_p}\right)\left(1+\frac{h}{d_p}\right)} \right) + 2.5\phi + 1$
Jang et al. [87]	$\mu = \left(2.5\phi + 1\right)\mu_f \left[1 + \eta \left(d_p/D\right)^{-2\epsilon} \phi^{2/3} \left(\epsilon + 1\right)\right]$
Maiga et al. [88][7]	$\mu = \mu_f \left(123\phi^2 + 7.3\phi + 1\right)$
[8]	$\mu = \mu_f \left(306\phi^2 + 0.19\phi + 1\right)$
Masoumi et al. [89]	$\mu = \mu_f + \rho_p V_B d_p^2 / \left(72 C \delta\right)$
Nguyen et al. [90]	$\mu = \mu_f 0.904 e^{0.1483\phi}$
	$\mu = \mu_f \left(0.015\phi^2 + 0.025\phi + 1\right)$

whereas the magnetic torque eq.(2.9) tries to realign it in the field direction. An angle, γ, between the magnetic moment of a particle and the actual field direction arises. Thus, a free particle rotation towards the magnetic field will be disturbed by shear flow and cause a resistance in the flow so that the fluid exhibits an increase in viscosity [81]. An
390 expression to describe the change in viscosity was developed by Shliomis [82] in 1972 which included the effect of Brownian motion by deriving an expression of the strength of the magnetic field and its direction written as

$$\mu_r = \frac{3}{2}\phi' \mu \frac{\zeta - \tanh\zeta}{\zeta + \tanh\zeta} < \sin^2\gamma > \tag{2.41}$$

known as the rotational viscosity where $< \sin^2\gamma >$ is the spatial average of the angle, γ.

[5] Semidiluted $0.01 < \phi < 0.10$.
[6] Semidiluted and Brownian motion.
[7] for water-γ Al_2O_3
[8] for Ethylene Glycol-γ Al_2O_3

3 Current state of research

Thermomagnetic convection refers to convective heat transfer based on local variation in fluid's magnetisation imposed by a temperature gradient in the presence of a magnetic field. A key feature is that cooler fluid is more magnetised than a hotter fluid resulting in a magnetisation gradient within the fluid that establishes flow fields where cooler fluid moves towards higher magnetic field regions to displace warmer fluid resulting in a thermomagnetic convective flow. Thus, non-isothermal perturbations of the fluid's magnetisation always (or almost always)[9] leads to convection [52, 91, 92]. The resulting thermomagnetic convection may be controlled by changing the fluid's composition, the temperature distribution, the intensity or direction of the applied external magnetic field [93].

3.1 Thermomagnetic convection under external uniform magnetic field

A first analytical approach to characterise thermomagnetic convection was obtained by Finlayson [49] in the late 1960s. His study analysed the onset of convection of a magnetic fluid in the presence of an external uniform magnetic field. For this purpose a magnetic Rayleigh number was developed equivalent to the conventional Rayleigh number to quantify the onset of thermomagnetic convection under a uniform external magnetic field and to characterise the strength of magnetic forces over heat and viscous diffusion written as

$$\mathrm{Ra_m} = \frac{\mu_0 K^2 \left(\Delta T\right)^2 L^2}{\rho \nu \kappa \left(1+\chi\right)} \tag{3.1}$$

where μ_0 is the vacuum permeability, K the pyromagnetic coefficient, T the temperature, L the characteristic length, ρ the density of the magnetic fluid, ν the kinematic viscosity, κ the thermal diffusivity and χ the magnetic susceptibility. Finlayson found that the critical value of the magnetic Rayleigh number approaches 1,708 and the problem reduced to the classical Rayleigh problem for the onset of convection. His analytical approach was later proven experimentally by Schwab et al. [94, 95] in the mid 1980s that presented a fairly good agreement. Results consistent with Finlayson and Schwab were obtained experimentally by Stiels [96] and numerically by Blennerhassett et al. [97] and Stiles and Kagan [98] using a magnetic fluid in a very strong magnetic field. Their approach included

[9] In the cause where the magnetic Rayleigh number is not above its critical value so that internal forces are dominate or other body force terms may act against the Kelvin force so that flow fields may not establish.

the temperature dependent viscosity and rotational viscosity effects. One could now conclude that the fluid composition may have an impact on the onset of convection. This particular case was invetstigated by Heckert et al. [93] who found different critical Rayleigh numbers of two kerosene based magnetic fluids. As the main difference of both fluids was in particle size distribution they assumed that particle size may play an important role for the onset of thermomagnetic convection which is yet not investigated.

The onset of thermomagnetic convection within a cylindrical fluid layer was studied by Lange [99] for dilute and non-dilute magnetic fluids. Results presented that it was possible to decide whether a magnetic fluid is dilute or not by measuring the onset of convection. The form of the Kelvin body force used was discussed in [100]. A comparison of numerical and experimental results on thermomagnetic convection were performed by Krakov et al. [101–103] in a square cavity and cubic cavity. They reported that uniform applied external magnetic fields on a magnetic fluid became non-uniform within the fluid domain. Thus, the temperature dependent magnetisation of the magnetic fluid had significant influence on the magnetic field distribution within the fluid that affected the structure of convective heat transfer. This was also observed by Yamaguchi et al. [104–106] who investigated combined natural and thermomagnetic convection experimentally and numerically by a Lattice Boltzmann model. The experiments were conducted such that natural convection of a magnetic fluid was subjected to an external uniform magnetic field that influenced convective heat transfer significantly. It was proven by Yamaguchi et al. that the Kelvin body force was much stronger than buoyancy and heat transfer increased compared to that without a magnetic field. Moreover, if the magnetic field intensity was increased heat transfer increased further.

Experiments with an aqueous glycerol based magnetic fluid with suspended gadolinium nitrate hexahydrate particles under the influence of external magnetic fields were studied by Bednarz et al. [107–110]. They utilised liquid-crystal thermography to visualise temperature fields within magnetic fluids. The heat transfer across the vertical heated boundaries was measured by a set of thermocouples. Results obtained by experiments were used as input parameters for a computational developed model that obtained sufficient accurate results accordring to the corresponding convective flow patterns and temperature fields for magnetic field intesities up to 10 Tesla. By changing the boundary conditions to a Rayleigh-Bénard configuration, Bednarz et al. found that natural convection is suppressed by applying a sufficient strong external uniform horizonatal magnetic field [111] and enhanced by a vertical field direction [112]. Further experiments that utilised liquid-crystal thermography to investigate thermomagnetic convection were conducted in a Hele-Shaw cell by Wen et al. [113, 114] and by Fronalik [115] in a verti-

cal cylinder using a Rayleigh-Bénard configuration. Fronalik et al. obtained consistent results to Bednarz et al. and Yamaguchi et al. e.g. that an increase in magnetic field intensity having a vertical direction increases the Rayleigh number resulting in an increase in Nusselt number. Analogous results were obtained by changing the thermal boundary conditons to a vertical heated cylinder [116].

Buoyancy and thermomagnetically driven convection in a cylindrical fluid layer was also experimentally investigated with liquid-crystal thermography and a finite volume numerical simulation by Bozhko et al. [117–119]. Two case scenarios of a horizontal and inclined vertical orientation of the cylindrical geometry was studied under the influence of a longitudinal homogeneous magnetic field which was able to control the shape of flow patters at an inclined orientation within the cylindrical cavity. The numerical simulation performed according to the system setup qualitatively reproduced the flow patterns. A quantitative comparison was not conducted as only limited information of the fluid's properties was available.

Cylindrical geometries were also studied by Jafari et al. [8,120] who investigated thermomagnetic convection in nano-scale and full-scale using a kerosene based magnetic fluid containing magnetite particles. The aim was to examine thermomagnetic convection and magneticphoresis caused by the Soret effect[10] at different parameters such as the volume fraction of magnetic phase, the aspect ratio of the fluid domain, the temperature difference across the fluid layer and the intensity of the uniform applied magnetic field. The results obtained that the temperature had the most significant impact on convective flow and on the magnetic Soret effect among others which was significantly enhanced when the magnetic field strength increased. Numerical results of the computational simulations were verified by experiments conducted by Völer et al. [121] which showed good agreement. A theoretical investigation of the Soret effect in convective magnetic fluid instability was performed by Shliomis et al. [122]. They concluded that thermomagnetic convection is affected by magneto- and thermophoretic transfer of magnetic particles due to the Soret effect. Thus, concentration differences imposed by a temperature gradient following the Soret effect and the Kelvin body force which leads to an additional redistribution of magnetic particles following magnetophoresis will cause oscillatory instabilities within the fluid.

Concentration differences of magnetic phase within magnetic fluids caused by a temperature gradient was also observed by Krakov and Nikiforov [123] in a porous medium

[10]Magnetophresis refers to thermodiffusion or also named thermophoresis caused by the Soret effect. This effect refers to the movement of particles within a fluid caused by a temperature gradient. In most cases particles move from warm to cold but also reverse motions are observed.

by thermomagnetic convection. They reported a complex dependence with hysteresis effects on the competition of buoyancy and Kelvin body force by which an increase in magnetic field intensity could either result in a reduced or enhanced heat transfer. Jin and Zhang's [124–126] numerical studies extended Krakov and Nikiforov by including the thermosensitive dependence of the magnetic fluid, different porosities and Darcy number. Magnetic convection in other media such as air and water was performed numerically by Tagawa et al. [127, 128] in a shallow cylinder and cubic cavity, respectively.

3.2 Thermomagnetic convection with constant magnetic field gradient

Thermomagnetic convection in spatial non-uniform magnetic field but with constant field gradient was first obtained analytically by Curtis [129] and accompanied by Lalas and Carmi [130] in the early 1970s. Both groups developed a magnetic Rayleigh number to quantify the onset of thermomagnetic convection under a constant magnetic field gradient. To characterise the driving force over viscous and thermal diffusion the magnetic Rayleigh number may be written as

$$\mathrm{Ra_m} = \frac{\mu_0 K \Delta T L^3}{\rho \nu \kappa} |\nabla H| \tag{3.2}$$

which is also given by Shliomis review of magnetic fluids in 1974 and includes magnetocaloric cooling and adiabatic expansion [4]. This magnetic Rayleigh number is equivalent to the conventional Rayleigh number eq.(4.65) and the magnetic Rayleigh number eq.(3.1) for constant magnetic field developed by Finlayson [49]. Since then, the literature has grown and thermomagnetic convection with constant magnetic field gradient was studied numerically by Jue [131], Tangthieng et al. [132] in a square cavity and by Berkovsky et al. [133] in a vertical fluid layer. Their experiments proposed that heat transfer is either enhanced or decreased depending on the external field direction. Experiments that are consistent with Berkovsky et al. were conducted by Sawada et al. [134]. Based on those experimental studies, Snyder et al. [135] developed a numerical model that introduced a combination of natural and thermomagnetic convection where buoyancy and Kelvin body force acted vertical such that the net force of both was expressed as an effective gravity term. As a positive gravity term did not agree with the experiments but was consistent with the literature Snyder et al. failed to explain the discrepancy between the experiments and numerical simulations. Similar results for a positive gravity term that did not agree with Sawada et al. were observed by Bouhrour and Kalache [136] that provided in addition to Berkovsky et al. a more detailed overview about flow and heat

transfer phenomena within magnetic fluids for different field directions.

3.3 Thermomagnetic convection with spatial non-uniform magnetic field

An overview of experimental investigation of thermomagnetic convection under microgravity conditions was performed by Odenbach [137]. Facilities such as space stations, drop towers and parabola flights may be used for experiments that provide different time frames under microgravity conditions. Experiments of the onset of thermomagnetic convection under microgravity conditions and in the presence of a magnetic field gradient were observed by Odenbach [138] in a drop tower.

Numerical studies of thermomagnetic convection under a non-uniform magnetic field performed by a permanent magnet in the absence of gravity was studied by Ganguly et al. [91,139] who used a numerical approach of a temperature dependant magnetic susceptibility in the Kelvin body force. The numerical results were consistent with literature such that the convection increased by increasing magnetic field intensity and temperature difference. They also found an empirical equivalence between magnetically and buoyancy induced convection which was based on their respective Rayleigh numbers. Further numercial studies with a temperature depended susceptibility were obtained by Mukhopadhyay et al. [140] in a square cavity and in a shallow enclosure by Banerjee et al. [141] for heat transfer applications. To give a quantitative measure of heat transfer performed by thermomagnetic convection within a magnetic fluid Ashouri et al. [142] presented numerical results of convective flow upon the correlating Nusselt number. The numerical equations in this study were non-dimensional and characterise the full dependence of Nusselt number along the non-dimensional characteristic length scale of the square cavity, the magnetic Rayleigh number, the rational temperature difference, the Prandtl number and the non-dimensional length of the magnet, its thickness and the gap between the cavity. Analogous studies of non-dimensional numerical models to characterise magnetic convection in a tube and in a rectangular duct were obtained by Aminfar et al. [58–60].

Heat transfer enhancement by thermomagnetic convection in the present of buoyancy was investigated by Früh [68]. His study analysed different temperature boundary conditions of a rectangular box filled with a commercial water based magnetic fluid. To induce a magnetic convection a permanent magnet was placed at three different configurations on the top, beneath and to the side of the box. The experimental and numerical results presented good agreement and concluded that thermomagnetic convection can either increase or reduce convection by means of the applied temperature boundary conditions

and the magnetic field direction. Früh also used magnetic fluids to analyse convection in geophysical processes by replacing the central force field with a magnetic field. His approach was to make use of the temperature dependant magnetisation of the magnetic fluid that was expressed by the pyromagnetic coefficient which was implemented in the Kelvin body force. The results suggested that such experiments may present a useful tool to model thermal convection in planetary interiors [143].

Identical to Früh's studies Zablocky et al. [144, 145], Blums [146] and Tynjälä and Ritvanen [147] made use of the pyromagnetic coefficient in their numerical approach to calculate the Kelvin body force. Their numerical results performed in a rectangular cell and cylinders, showed good agreement with their experimental investigations. Thermal flow of magnetic fluids in the presence of magnetic field with the focus upon particle size, mass fraction and the strength of external applied magnetic field was investigated by Chang et al. [148]. The results provided by numerical investigation indicate that magnetic fluids with a higher mass fraction have a higher response to external magnetic fields and convection is increased. Furthermore, the smaller the dispersed magnetic particles the better is the ability to dissipate heat of the macroscopic magnetic fluid. This was confirmed by Sheikholeslami and Gorji-Bandpy [149] who utilised a Lattice Boltzmann model to study the effect of particle size, volume fraction of dispersed cobalt particles at different Rayleigh numbers. Results consisted with Sheikholeslami and Gorji-Bandpy were performed by Kefayati using a kerosene based magnetic fluid with cobalt particles [150–152]. However, both studies showed confusion about ferrohydrodynamics (FHD) and magnetohydrodynamics (MHD). It must be clearly stated that FHD and MHD are two separate disciplines and cannot be mixed together if the fluid is considered non-conductive and the Lorenz force is absent. A study more focussed on practical applications was carried out by Selimefendigil et al. in a partially heated square enclosure [153] and within a triagular shape [154]. Both studies presented an increase in heat transfer with increasing Rayleigh number. However, local variations in the enclosures were observed which could either increase or decrease the overall heat transfer.

In general reports show a range of a reduction of 40% to about 140% enhancement in heat transfer [68]. As can be seen thermomagnetic convection is a useful tool to enhance heat transfer where natural convection may not be possible or is not sufficient enough. The ability to adjust external magnetic fields may be used to control the flow of a heated magnetic fluid. Qi et al. [155] and Wang and Wakayama [156] demonstarted this by using external fields to control the flow of natural convection. A potential application of thermomagnetic convection is presented by Strek [157, 158] in channel flow which may be used in a loop to pump magnetic fluid [159] using its thermosensitive property to provide

an active system cooling [160].

3.4 Thermomagnetic convection with alternating magnetic field

After the success of manufacturing magnetic fluids in the mid-1960 when ferrohydrodynamic began to develop, magnetic fluid research was far from being complete. Since then the direction of studies followed towards the applications of magnetic fluid and to smaller and smaller systems such as the investigation of the microscopic fluid behaviour [6]. The focus was in general to understand the theories of the microscopic phenomena such as inter-particle, fluid particle interactions and their response to magnetic fields in terms of magneto-dissipation, spin of magnetic particles to alternating magnetic fields and the thermal heating effect within magnetic fluid. Hence, the literature of the macroscopic study of convection with magnetic fluids under alternating magnetic field is sparse. However, some applications are still of interest especially the heat transport within heated channels using forced convection under alternating magnetic fields [161–167]. Reports present that the forced flow within the channels was significantly influenced by the thermomagnetic force induced by external alternating magnetic fields. The degree in which heat transfer was enhanced varied between 13.5% and 62.7%.

Thermomagnetic convection under alternating magnetic fields was studied theoretically and numerically by Kaloni and Lou [168] in a thin horizontal layer of a magnetic fluid heated from the bottom. The model considered internal rotations, particle-particle interactions and magnetising relaxation. Results showed that at higher frequencies, of more than 10^4 Hz the Nusselt number and Rayleigh number increased significantly and convection was increased. A horizontal layer of magnetic fluid was also studied by Belyaev and Smorodin [169]. The parametric study of convective instability of a magnetic fluid analysed the behaviour and response of the magnetic fluid to alternating magnetic fields with a zero mean value. The perturbations found had a synchronous character and were divided into different classes with respect on the temperature difference applied on the boundaries, the frequency and amplitude of the alternating external magnetic field by considering the physical properties of the magnetic fluid.

Time-periodic combined natural and thermomagnetic convection was studied in a cubical enclosure under alternating magnetic field by Kim and Hyun [170]. The numerical results showed a resonant internal gravity oscillation that affected the heat transport. The Nusselt number and velocity fields responded to the applied external magnetic field and alternated with the same frequency but with different amplitude. Equivalent results were found by Kang and Hyun [171]. The magnetic fluid responded to the alternating magnetic

fields and gravity oscillations affected the fluid flow. The flow patterns were characterised in counter-clockwise and clockwise convection cells that developed over a short time such that the system's spatial temperature distribution underwent periodic variations.

All these theoretical, numerical and experimental studies validated the possibility to use magnetic fluids in heat transfer applications. The ability to use such fluids e.g. in power transformers enables a new generation of intelligent cooling fluids. The studies conducted for natural convection in power transformers [172–176] may be extended by prototyping a magnetic fluid cooled transformer as was studied numerically and in experiments by Morega et al. [177, 178] and Pislaru and Danescu [179].

4 Fundamentals and theory

This chapter gives an introduction to the fundamentals and theory of thermomagnetic convection. It is split into the magneto-statics field equations, the fundamentals of fluid dynamics and heat transfer, the resulting non-dimensional numbers and the governing equations of thermomagnetic convection.

4.1 Magnetostatic field equation

A magnetic field, $\mathbf{H}$, is generated by a pair of magnetic poles of strength p and $-p$ separated by a distance, r. The field surrounding the pole is expressed after *Columb's law* of magnetisation and written as

$$\mathbf{H} = \frac{p}{4\pi\mu_0}\frac{\mathbf{r}}{|\mathbf{r}|^3} \tag{4.1}$$

where $\mathbf{r}$ is the position vector from p to $-p$. The magnetic field lines through a control surface, $\mathrm{d}S$, are given by

$$\mathbf{H}\cdot\mathbf{n}\,\mathrm{d}S \tag{4.2}$$

where $\mathbf{n}$ is the outward pointing unit norm vector. For an arbitrary enclosed surface the outward field flux is then

$$\oint_S \mathbf{H}\cdot\mathbf{n}\,\mathrm{d}S \tag{4.3}$$

and for N pole pairs, where each pole contributes to the magnitude of the total field $\mathbf{H}$ may be written as

$$\sum_{i=1}^{N}\oint_S \mathbf{H_i}\cdot\mathbf{n}\,\mathrm{d}S = \sum_{i=1}^{N}\frac{p_i}{\mu_0}. \tag{4.4}$$

As N pole pairs may have positive or negative magnitudes they can be generalised of a continuous distribution and characterised by a volume pole density, ρ_V. The number of pole pairs in an arbitrary control volume, $\mathrm{d}V$, is $\rho_V\,\mathrm{d}V$ and the total magnetic field may be expressed as

$$\oint_S \mathbf{H}\cdot\mathbf{n}\,\mathrm{d}S = \int_V \frac{\rho_V}{\mu_0}\,\mathrm{d}V. \tag{4.5}$$

Applying the divergence theorem one obtains

$$\oint_S \mathbf{H}\cdot\mathbf{n}\,\mathrm{d}S = \int_V \nabla\cdot\mathbf{H}\,\mathrm{d}V \tag{4.6}$$

and for an infinitesimal volume element

$$\nabla\cdot\mathbf{H} = \frac{\rho_V}{\mu_0} \tag{4.7}$$

which is applicable in all regions of space. As the magnitude of a magnetic field, $\mathbf{H}$, refers to the strength of polarisation, p, of the magnetised material the volume pole density, ρ_V, is given by

$$\rho_V = -\mu_0 \nabla \cdot \mathbf{M} \tag{4.8}$$

where M is the magnetisation of a magnetic material. Combining eq.(4.7) and eq.(4.8) it must be true that $\nabla \cdot \mathbf{H} = -\nabla \cdot \mathbf{M}$ and the magnetic induction field, $\mathbf{B}$, is defined as

$$\mathbf{B} = \mu_0 \left(\mathbf{H} + \mathbf{M}\right) \tag{4.9}$$

and satisfies the relationship

$$\nabla \cdot \mathbf{B} = 0 \tag{4.10}$$

which is one of Maxwell's equation. In magneto-statics where no electric current flows *Ampére's law* results in

$$\nabla \times \mathbf{H} = 0 \tag{4.11}$$

as the cross product of parallel vectors is zero [2].

4.2 Fluid dynamics

4.2.1 The continuity equation

The continuity equation represents the conservation of mass. It states the process where a mass flow into a system must equal the mass flow out of the same system. For a control volume, $\mathrm{d}V$, the mass, m, can be evaluated by integration

$$\int_V \rho \, \mathrm{d}V \tag{4.12}$$

where ρ is the density. The rate of change in mass is the mass flux through the control surface, $\mathrm{d}S$, given by

$$\frac{\mathrm{d}}{\mathrm{d}t} m = \oint_S \rho \mathbf{u} \cdot \mathbf{n} \, \mathrm{d}S \tag{4.13}$$

where t is the time step and $\mathbf{u}$ the velocity. For an increasing mass the mass flux is negative trough the control surface and positive by decreasing mass. Thus,

$$\frac{\mathrm{d}}{\mathrm{d}t} m = \frac{\mathrm{d}}{\mathrm{d}t} \int_V \rho \, \mathrm{d}V + \oint_S \rho \mathbf{u} \cdot \mathbf{n} \, \mathrm{d}S \tag{4.14}$$

675 applying the divergence theorem eq.(4.14) may be written as

$$\int_V \left(\frac{\mathrm{d}}{\mathrm{d}t}\rho + \nabla \cdot (\rho \mathbf{u}) \right) \, \mathrm{d}V = 0. \tag{4.15}$$

As the control volume is considered independent in time the only time derivative is the change of density. To satisfy mass conservation for the arbitrary infinitesimal control volume the continuity equation must equal to zero and is written as

$$\frac{\mathrm{d}}{\mathrm{d}t}\rho + \nabla \cdot (\rho \mathbf{u}) = 0. \tag{4.16}$$

A special cases may be considered when ρ is constant and/or the fluid is considered
680 incompressible. The continuity equation reduces to

$$\nabla \cdot \mathbf{u} = 0 \tag{4.17}$$

for incompressible flow [180].

4.2.2 The equation of motion

The change of momentum of an object that is equal to the applied forces and is described by *Newton's second law of motion* is written as

$$\mathbf{F} = m\mathbf{a} = \mathrm{d}\left(m\mathbf{v}\right)/\mathrm{d}t. \tag{4.18}$$

685 *Newtons second law* can also be applied on fluid motion by rephrasing it to an infinitesimal fluid element in place of a solid object through which fluid is flowing. The overall force acting on the finite element is characterised over a control volume, $\mathrm{d}V$, written as

$$\mathbf{F} = \int_V \rho \, \mathrm{d}V \frac{\mathrm{d}\mathbf{u}}{\mathrm{d}t}. \tag{4.19}$$

In the following *Newton's second law* may be formulated to discuss the rate of change of momentum and rate of flow of momentum. For this purpose and to simplify let us first
690 consider a scalar quantity e.g. the temperature, T, of a fluid element moving with the fluid. The change in temperature produced by a small time step, t, and the changes in Cartesian postion, $\mathbf{P}$, $\in \mathbb{R}^3$ may be written as

$$\mathrm{d}T = \frac{\partial T}{\partial t}\mathrm{d}t + \frac{\partial T}{\partial x}\mathrm{d}x + \frac{\partial T}{\partial y}\mathrm{d}y + \frac{\partial T}{\partial z}\mathrm{d}z \tag{4.20}$$

and the rate of change can be written by dividing by $\mathrm{d}t$

$$\frac{\mathrm{d}T}{\mathrm{d}t} = \frac{\partial T}{\partial t} + \frac{\partial T}{\partial x}\frac{\mathrm{d}x}{\mathrm{d}t} + \frac{\partial T}{\partial y}\frac{\mathrm{d}y}{\mathrm{d}t} + \frac{\partial T}{\partial z}\frac{\mathrm{d}z}{\mathrm{d}t}. \tag{4.21}$$

Considering the distance, $\mathrm{d}x$, $\mathrm{d}y$, $\mathrm{d}z$ of the infinitesimal fluid element in a time step, t, the components $\mathrm{d}x/\mathrm{d}t$, $\mathrm{d}y/\mathrm{d}t$, $\mathrm{d}z/\mathrm{d}t$ present the three velocity components of the fluid element and eq.(4.21) may be written as

$$\frac{\mathrm{D}T}{\mathrm{D}t} = \frac{\partial T}{\partial t} + u\frac{\partial T}{\partial x} + v\frac{\partial T}{\partial y} + w\frac{\partial T}{\partial z} \tag{4.22}$$

where $\mathrm{D}/\mathrm{D}t$ is the total or material derivative. The rate of change in temperature, T, eq.(4.22) can be summarised in vector notation as

$$\frac{\mathrm{D}T}{\mathrm{D}t} = \frac{\partial T}{\partial t} + \mathbf{u}\cdot\nabla T \tag{4.23}$$

and the general operator as

$$\frac{\mathrm{D}}{\mathrm{D}t} = \frac{\partial}{\partial t} + \mathbf{u}\cdot\nabla. \tag{4.24}$$

The total derivative can also be applied to vectors i.e. the change of velocity, $\mathbf{u}$, following the flow written as

$$\frac{\mathrm{D}\mathbf{u}}{\mathrm{D}t} = \frac{\partial \mathbf{u}}{\partial t} + \mathbf{u}\cdot\nabla\mathbf{u} \tag{4.25}$$

where the velocity has two quantities, the change of the fluid flow and the intensity of the change. Extending the rate of change of momentum following the fluid per unit volume eq.(4.25) extends to

$$\rho\frac{\mathrm{D}\mathbf{u}}{\mathrm{D}t} = \rho\left(\frac{\partial \mathbf{u}}{\partial t} + (\mathbf{u}\cdot\nabla)\,\mathbf{u}\right) \tag{4.26}$$

know as the advection of momentum [180]. After introducing the rate of change of momentum of a infinitesimal fluid element the forces that may act on the fluid, in the context of ferrohydrodynamic are introduced. The forces that maybe act on a fluid element are divided into those which act on the control surface of the infinitesimal fluid element, '*surface forces*', and those who apply at the bulk of the fluids volume, '*body forces*'. For thermomagnetic convection those forces are pressure, internal forces from viscous dissipation, gravity and electromagnetic forces which are introduced next.

4.2.3 Surface forces

4.2.3.1 The pressure force

The pressure, p, is a force acting perpendicular on the control surface of an infinitesimal fluid element. If a pressure acts on the left surface of a volume element $\in \mathbb{R}^3$ the force in the x-direction is written as

$$F_{p,xleft} = pA = p \, \mathrm{d}y\mathrm{d}z \tag{4.27}$$

it follows that the element moves according to *Newton's second law of motion* to the right in the x-direction with

$$F_{p,xright} = -\left(p + \frac{\partial p}{\partial x}\right) \mathrm{d}y\mathrm{d}z. \tag{4.28}$$

The overall pressure force experienced by an infinitesimal fluid element in the x-direction is

$$F_{p_x} = F_{p_{xleft}} + F_{p_{xright}} = -\frac{\partial p}{\partial x} \mathrm{d}y\mathrm{d}z. \tag{4.29}$$

Thus, the general form of the pressure gradient may be written as

$$\mathbf{f_p} = -\nabla p \tag{4.30}$$

by dividing with the volume of the infinitesimal fluid element.

4.2.3.2 The viscous shear force

Real fluids are viscous and experience stress that is irreversible. The viscous stress is described by the viscous stress tensor, $\boldsymbol{\tau}$, that acts on an infinitesimal volume element with surface, $\mathrm{d}S$, given by

$$\boldsymbol{\tau} = \oint_S \boldsymbol{\tau} \cdot \mathbf{n} \, \mathrm{d}S. \tag{4.31}$$

By applying the divergence theorem one obtains

$$\boldsymbol{\tau} = \int_V \nabla \cdot \boldsymbol{\tau} \, \mathrm{d}V. \tag{4.32}$$

Assuming a Newtonian fluid with constant dynamic viscosity, μ, so that the shear stress is proportional to the rate of deformation[11] and may be written as

$$\tau_{ij} = \mu \left(\frac{\partial u_i}{\partial x_j} + \frac{\partial u_j}{\partial x_i}\right). \tag{4.33}$$

[11] In other words the stress is proportional to the change in velocity in the direction of stress.

By applying the divergence theorem and writing the stress tensor in a 3×3 matrix gives

$$\nabla \cdot \boldsymbol{\tau} = \mu \nabla \cdot \begin{pmatrix} \tau_{xx} & \tau_{xy} & \tau_{xz} \\ \tau_{yx} & \tau_{yy} & \tau_{yz} \\ \tau_{zx} & \tau_{zy} & \tau_{zz} \end{pmatrix} = \mu \nabla \cdot \begin{pmatrix} 2\frac{\partial u}{\partial x} & \frac{\partial u}{\partial y} + \frac{\partial v}{\partial x} & \frac{\partial u}{\partial z} + \frac{\partial w}{\partial x} \\ \frac{\partial u}{\partial y} + \frac{\partial v}{\partial x} & 2\frac{\partial v}{\partial y} & \frac{\partial v}{\partial z} + \frac{\partial w}{\partial y} \\ \frac{\partial u}{\partial z} + \frac{\partial w}{\partial x} & \frac{\partial v}{\partial z} + \frac{\partial w}{\partial y} & 2\frac{\partial w}{\partial z} \end{pmatrix} \tag{4.34}$$

and the viscous force per unit volume acting in the x-direction may be written as

$$\begin{aligned} (\nabla \cdot \boldsymbol{\tau})_x &= \frac{\partial}{\partial x}\left(2\mu\frac{\partial u}{\partial x}\right) + \frac{\partial}{\partial y}\left(\mu\left(\frac{\partial u}{\partial y} + \frac{\partial v}{\partial x}\right)\right) + \frac{\partial}{\partial z}\left(\mu\left(\frac{\partial u}{\partial z} + \frac{\partial w}{\partial x}\right)\right) \\ &= 2\mu\frac{\partial^2 u}{\partial x^2} + \mu\frac{\partial^2 u}{\partial y^2} + \mu\frac{\partial^2 v}{\partial y \partial x} + \mu\frac{\partial^2 u}{\partial z^2} + \mu\frac{\partial^2 w}{\partial z \partial x} \\ &= \mu\frac{\partial^2 u}{\partial x^2} + \mu\frac{\partial^2 u}{\partial y^2} + \mu\frac{\partial^2 u}{\partial z^2} + \mu\frac{\partial^2 u}{\partial x^2} + \mu\frac{\partial^2 v}{\partial y \partial x} + \mu\frac{\partial^2 w}{\partial z \partial x} \\ &= \mu\nabla^2 u + \mu\frac{\partial}{\partial x}\left(\frac{\partial u}{\partial x} + \frac{\partial v}{\partial y} + \frac{\partial w}{\partial z}\right). \end{aligned} \tag{4.35}$$

Applying the continuity eq.(4.17) for incompressible flow the last therm in eq.(4.35) vanishes. The y- and z-components are corresponding to the x-component, and the vectorial viscous force per unit volume is written as

$$\mathbf{f_v} = \mu\nabla^2\mathbf{u} \tag{4.36}$$

for an incompressible Newtonian fluid with constant viscosity [180].

4.2.4 Body forces

4.2.4.1 Gravitation

Gravity is experienced as an acceleration in a gravitational field and may be written as a body force term with

$$\mathbf{f_g} = \rho\mathbf{g} \tag{4.37}$$

where $\mathbf{g}$ is the gravitational acceleration and derivable from a potential $-\nabla\Phi$. In circumstances where density variations are important such as in convection caused by temperature differences, the density may be expressed as a function of temperature by

$$\rho(T) = \rho_0 + \Delta\rho \tag{4.38}$$

where $\Delta\rho$ can be linearised with a Boussineq approximation. Thus,

$$\Delta\rho = -\rho_0 \beta \Delta T. \tag{4.39}$$

Hence, the change in gravitational acceleration due to the change of the temperature dependent density may be written as

$$\mathbf{f_g} = \rho\beta\Delta T \mathbf{g} \tag{4.40}$$

known as the buoyancy force [12] [180].

4.2.4.2 Kelvin body force

If a magnetic material with a magnetisation vector, $\mathbf{M}$, aligned with its geometric axis, $\mathbf{d}$, is subjected to an external applied magnetic field, $\mathbf{H}$, it experiences a force (Fig. 4.1). The magnitude of the magnetisation vector is expressed as a pole surface density of $\rho_a = \mu_0 M$ having an area, a_d. The arbitrary volume of the element is δV and equals to $a_d d$. Thus, the force experienced by the magnetic material may be written as

$$-\mathbf{H}\rho_a a_d + (\mathbf{H} + \delta\mathbf{H})\,\rho_a a_d = \delta\mathbf{H}\rho_a a_d \tag{4.41}$$

where $\delta\mathbf{H}$ is the change of the magnetic field in direction, $\mathbf{d}$. Hence, $\delta\mathbf{H} = (\mathbf{d}\cdot\nabla)\,\mathbf{H} = (d/M)\,(\mathbf{M}\cdot\nabla)\,\mathbf{H}$ so that the Kelvin force is given by

$$\mathbf{f_K} = \mu_0\,(\mathbf{M}\cdot\nabla)\,\mathbf{H} \tag{4.42}$$

which represents the magnetic force acting on a magnetic fluid as a vector moment per unit volume [2]. In the case when a magnetic fluid is filled in a cavity and a temperature gradient is absent the fluid remains stable due to its magnetisation and adiabatic compression such that convection does not occur. However, in the presence of a temperature gradient the magnetisation changes due to the *Currie law* and non-isothermal perturbations of the magnetising field result in a net driving force. This force can be linearised and eq.(4.42) written as

$$\mathbf{f_K} = \mu_0 K\ \Delta T\ \nabla H \tag{4.43}$$

where $K = -\left(\partial M/\partial T\right)_{\phi,H}$ is the pyromagnetic coefficient presented in eq.(2.27) and ΔT the temperature difference across the system investigated.

[12] where ρ is reverted to the quantities temporarily written by ρ_0

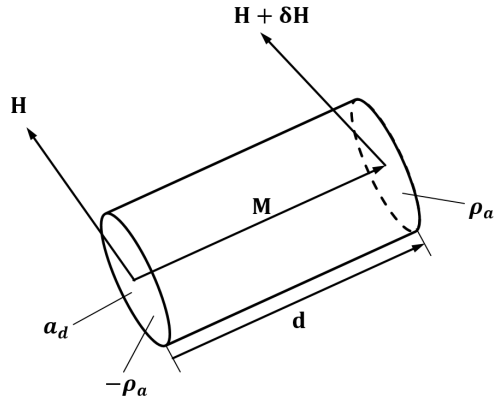

Figure 4.1: Development of the Kelvin body force on a small magnetised material Fig. 1.6 in [2].

4.2.4.3 Magneto-dissipation

The origins of magneto-viscous effects are internal rotations of magnetic particles that increase viscosity in presence of a magnetic field. This phenomenon emerges out of the mechanical torque produced by viscous friction that colloidal particles experience in a shear flow in the presence of an external magnetic field that tends to align the particles in field direction. The magneto-viscous effects in a single-domain colloidal magnetic fluid maybe written as

$$\mathbf{f_{MD}} = \frac{\mu_0}{2} \nabla \times (\mathbf{M} \times \mathbf{H}) \tag{4.44}$$

assuming spherical particles [52, 181]. In the case of natural and thermomagnetic convection where fluid velocities are small and with stationary applied magnetic field, one can assume that the magnetic moment of the magnetic fluid is always aligned with the external applied magnetic field. Under these conditions the magnetic fluid may be considered to be free from magneto-viscous effects and $\mathbf{f_{MD}}$ may be neglected as it was done in [91, 139–141, 182, 183].

4.2.5 The Navier-Stokes equation

In combining equation eq.(4.26), (4.30) and (4.36) one obtains

$$\rho \left(\frac{\partial \mathbf{u}}{\partial t} + (\mathbf{u} \cdot \nabla) \mathbf{u} \right) = -\nabla p + \mu \nabla^2 \mathbf{u} + \mathbf{f} \tag{4.45}$$

known as the dynamic form of the Navier-Stokes equation for incompressible fluids, where $\mathbf{f}$ represents any additional body force term that acts on the infinitesimal fluid element e.g. gravity. The equation conserves momentum and may be rewritten in its kinematic

form by dividing by the density presented as

$$\frac{\partial \mathbf{u}}{\partial t} + (\mathbf{u} \cdot \nabla)\,\mathbf{u} = -\frac{1}{\rho}\nabla p + \nu \nabla^2 \mathbf{u} + \frac{1}{\rho}\mathbf{f} \tag{4.46}$$

where $\nu = \mu/\rho$ and is the kinematic viscosity.

4.3 Heat transfer

A general definition of heat transfer is the transit of thermal energy caused by a spatial temperature difference. This transit may occur between media or within a medium when a temperate difference is present. To consider heating or cooling effects the process of heat transfer as modes need to be defined.

The first mode is heat conduction that occurs in stationary media such as solid objects or fluids. The empirical expression refers to *Fourier's law of heat conduction* and quantifies the relation of the heat transfer process across a medium or media that is proportional to the contact surface area, A, the thermal conductivity, k, and the temperature gradient, ∇T. Following this one arrives to *Fourier's law of heat conduction* written as

$$\mathbf{Q} = -k_s A \nabla T \tag{4.47}$$

where k_s is the thermal conductivity of the solid object. The heat flux across the surface area, A, may be written as

$$\mathbf{q} = \frac{\mathbf{Q}}{A} = -k_s \nabla T. \tag{4.48}$$

A further mode of heat transfer is convection and is based on an energy transfer cause by conduction and bulk fluid motion. A empirical relation may be formulated after *Newtons law of cooling* written as

$$Q = hA\,\mathrm{d}T \tag{4.49}$$

where h is the convective heat transfer coefficient. The bulk fluid motion refers to advection within the fluid and is cause by a temperature sensitive fluid property in presence of a body force such as buoyancy and may be written as

$$\mathbf{q} = \rho c \mathbf{u}\,\mathrm{d}T \tag{4.50}$$

where c is the heat capacity.

Thermal energy can not only be transferred by conduction and convection alone. The thermal energy emitted by matter at non-zero temperature requires a formulation of heat

transfer by radiation that can occur both in vacuum and in media. A relationship may be formulated after the *Stefan-Boltzmann law* that takes the total emitted amount of thermal energy emitted by a black body in to account and is may be given by

$$Q = \sigma A T^4 \tag{4.51}$$

where $\sigma = 5.6704 \times 10^{-8}$ is the Stefan-Boltzmanns's constant. A more detailed introduction to radiative heat transfer is provided in §5.3 that focus on the experimental methodology of recording temperature fields with infrared thermography.

4.3.1 The lumped capacity solution

A common approximation in transient heat transfer is the lumped capacity solution which is based on the problem to predict convective cooling of solid objects at their solid-fluid interface. The approximation assumes a uniform spatial temperature distribution of the solid object during a transient heat transfer process across the solid-fluid interface. Hence, the internal conduction processes of the solid object is not of importance as the heat transfer within the solid object is assumed to be much faster than across the solid-fluid interface. The solid object may then be treated analogues to an electrical capacitative reservoir within the transient process until it reaches thermal equilibrium in time. This implicit an infinite thermal conductivity when a temperature gradient is absent within the solid which is after *Fourier's law* clearly impossible. However, the condition closely approximates when the conductive thermal resistance within the soil object is small compared to the convective resistance of the the surroundings of the solid. Thus, it is important to determine under what condition the lumped capacity solution is reasonable accurate.

To develop a suitable criterion one can considered a steady-state conduction solution through a plane wall like the experimental setup in § 7.2.1 where two opposite side walls of a cavity filled with a magnetic fluid are kept at two different constant temperatures. Choosing one of the walls that is maintained at a temperature, $T_{s,1}$, whereas the other surface is exposed to the magnetic fluid with temperature $T_\infty < T_{s,1}$ gives an intermediate surface temperature, $T_{s,2}$, at the solid-fluid interface and one can write the following temperature relationship $T_\infty < T_{s,2} < T_{s,1}$. Assuming a steady-sate condition one can write for the surface energy balance

$$hA\left(T_{s,2} - T_\infty\right) = \frac{k_s A_s}{L}\left(T_{s,1} - T_{s,2}\right) \tag{4.52}$$

where A_s is the surface of the solid-fluid interface. Rearranging eq.(4.52) one obtains

$$\frac{R_{cond}}{R_{conv}} = \frac{T_{s,1} - T_{s,2}}{T_{s,2} - T_\infty} = \frac{Lh}{k_s} = \mathrm{Bi} \tag{4.53}$$

where R_{conv} and R_{cond} are the convective and conductive thermal resistance. The ratio of both as written above gives the non-dimensional Biot number, Bi, that describe the temperature drop within a solid object relatively to the temperature of the solid-fluid interface [184]. The lumped capacity approximation may then be true for systems where $\mathrm{Bi} < 1$ or the solution to assume an absent temperature gradient within a solid object is not reasonable accurate [185].

4.3.2 Heat transfer in fluids

To consider heating or cooling effects either at a boundary or within fluids requires an equation for the change in temperature. However, the variation in temperature also changes the physical properties of the fluid. Thus, a full analysis of all temperature dependent fluid properties is a difficult task and approximations become essential. In the Boussinesq approximation, as used to evaluate the variation of the density in the buoyancy force, all other temperature dependent fluid properties are ignored so that the fluid is considered with a constant heat capacity, c_p, per unit volume[13]. As the fluid within this thesis is considered incompressible the heat capacity, $c = c_p = c_v$, and the heat capacity for a constant pressure process with index p is used in this thesis. Hence, the rate of change in temperature derived in eq.(4.23) is expanded by the constant heat capacity per unit volume to count for heat advection within the fluid corresponding to eq.(4.50) written as

$$\rho c_p \frac{\mathrm{D}T}{\mathrm{D}t} = \rho c_p \left(\frac{\partial T}{\partial t} + \mathbf{u} \cdot \nabla T \right). \tag{4.54}$$

The heat within the fluid is transferred by internal heat generation or heat conduction of the neighbouring fluid elements after *Fourier's law* eq.(4.47) that is rearranged for an infinitesimal fluid element by dividing with the fluid volume, V, to

$$q_{cond} = -k \nabla^2 T. \tag{4.55}$$

[13] In the Boussinesq approximation the heat capacity for constant pressure is used. For more details see Tritton chapter 14 Appendix [180].

Combining eq.(4.54) and eq.(4.55) the energy equation, solving for temperature, T, may then be formulated as

$$\rho c_p \left(\frac{\partial T}{\partial t} + (\mathbf{u} \cdot \nabla) T \right) = k \nabla^2 T + Q \tag{4.56}$$

where Q represents any internal or external heat sources. If the thermal conductivity is considered constant eq.(4.56) may be rewritten as

$$\frac{\partial T}{\partial t} + (\mathbf{u} \cdot \nabla) T = \kappa \nabla^2 T + \frac{Q}{\rho c_p} \tag{4.57}$$

where $\kappa = k/(\rho c_p)$ is the thermal diffusivity, also refereed to thermometric conductivity [180].

4.4 Non-dimensional numbers

In this section, the main non-dimensional numbers are introduced to characterise heat transfer by convection and to derive the non-dimensional equations. A quantitative non-dimensional parameter to characterise different flow conditions such as laminar or turbulent flow is given by the Reynolds number, Re, and found as a ratio of inertial forces to viscous forces written as

$$\mathrm{Re} = \frac{\text{inertial force}}{\text{viscous force}} = \frac{\rho u L}{\mu} = \frac{u L}{\nu} \tag{4.58}$$

where L is the characteristic length scale. The Reynolds number maybe used to predict similar flow conditions in different flow simulations. In convective flow the velocity distribution is governed by the temperature. However, the temperature distribution depends also on the advection of heat which makes convective flow a more complex task [180]. As the temperature difference in presence of gravitational acceleration is the driving force in natural convection two non-dimensinal parameters are derived from eq.(4.46) and eq.(4.57) the Grashof number

$$\mathrm{Gr} = \frac{\text{buoyancy force}}{\text{viscous force}} = \frac{\beta \, \Delta T g L^3}{\nu^2} \tag{4.59}$$

and the Prandtl number

$$\mathrm{Pr} = \frac{\nu}{\kappa}. \tag{4.60}$$

The Prandtl number is a physical property of the fluid written as the ratio of the kinematic viscosity to thermal diffusivity. It is an indication of the relative role of the viscous and thermal boundary layer and presents the ratio of momentum and vorticity diffusion to heat

diffusion. The Grashof number is the ratio of buoyancy to viscous force and indicates the type of flow such as laminar or turbulent in convective flow regimes. Thus, the Reynolds number for convective flow depends on the fluid's Prandtl number and Grashof number and one obtains

$$\mathrm{Re} = f\left(\mathrm{Gr}, \mathrm{Pr}\right). \tag{4.61}$$

A further non-dimensional parameter is the Nusselt number, Nu, which quantifies the heat transfer by convection and is found as a ratio of total heat transfer to the conductive heat transfer written as

$$\mathrm{Nu} = \frac{\text{total heat transfer}}{\text{conductive heat transfer}} = \frac{hL}{k} \tag{4.62}$$

where h is the convective heat transfer coefficient and k the thermal conductivity of the fluid and should not be confused with the Biot number, Bi, eq.(4.53) that is a ratio of the heat transfer resistance inside and at the surface of a solid object. A Nusselt number $\mathrm{Nu} = 1$ would indicate a heat transfer by conduction alone and $\mathrm{Nu} > 1$ an enhanced heat transfer by convection. Hence,

$$\mathrm{Nu} = f\left(\mathrm{Gr}, \mathrm{Pr}\right) \tag{4.63}$$

and is proportional to the applied temperature difference. As heat transfer may exhibit local variation in intensity, an overall or surface averaged Nusselt number is obtained by integrating the heat flux, q_{total}, over a surface area, A, written as

$$\mathrm{Nu} = \frac{L}{k\ \Delta T}\ \frac{1}{A} \int q_{total}\, \mathrm{d}A. \tag{4.64}$$

As in convective cases the process of determining the temperature distribution and the dynamic processes within a fluid are of importance, an additional non-dimensional number is formulated and written as

$$\mathrm{Ra} = \mathrm{Gr}\ \mathrm{Pr} = \frac{\beta\ \Delta T g L^3}{\nu\kappa} \tag{4.65}$$

known as the Rayleigh number [180]. The Rayleigh number is found as a product of the Grashof and Prandtl number and characterises the form of heat transfer. If $\mathrm{Ra} > \mathrm{Ra}_c$ heat transfer is primarily in form of convection and if $\mathrm{Ra} < \mathrm{Ra}_c$ heat transfer is primarily in form of conduction where R_c is the critical Rayleigh number of the system. Hence, the Nusselt number is a function of the Rayleigh number and one would expect that an increasing Ra increases Nu which is stated in literature [180, 186].

4.5 Governing equations of thermomagnetic convection

This section contains the governing equations of thermomagnetic convection in the presence of buoyancy for an incompressible magnetic fluid where magneto viscous effects are neglected and the magnetic fluid is assumed to be free of electric effects and considered non-conductive. Thus, the continuity equation is written as

$$\nabla \cdot \mathbf{u} = 0 \tag{4.66}$$

and momentum equation represented in kinematic form as

$$\frac{\partial \mathbf{u}}{\partial t} + (\mathbf{u} \cdot \nabla)\,\mathbf{u} = -\frac{1}{\rho}\nabla p + \nu \nabla^2 \mathbf{u} + \beta\ \Delta T\ \mathbf{g} + \frac{\mu_0}{\rho} K \Delta T\ \nabla H \tag{4.67}$$

and uses the Bossinesq approximation for buoyancy eq.(4.40) and the Kelvin body force eq.(4.43) as body forces. The pyromagnetic coefficient, K, is written as

$$K \equiv -\left(\frac{\partial M_P}{\partial T}\right)_{H,\phi} \tag{4.68}$$

where M_P is the extended Langevin magnetisation after Pshenichinkov presented in eq.(2.24) and includes the effect of inter-particle interactions in the magnetisation term. The heat equation, solving for temperature, T, is presented as

$$\frac{\partial T}{\partial t} + (\mathbf{u} \cdot \nabla)\, T = \kappa \nabla^2\ T \tag{4.69}$$

and solved simultaneously with the continuity and momentum equation.

4.5.1 Non-dimensional form of equations

A quantitative non-dimensional parameter for natural convection was introduced in eq.(4.65) and represents the conventional Rayleigh number which is found as a ratio of buoyancy to viscous dissipation and heat diffusion. To attempt a quantitative comparison of natural and thermomagnetic convection a magnetic Rayleigh number may be developed by using a ratio of the Kelvin body force to viscous dissipation and heat diffusion and may be written as

$$\mathrm{Ra_m} = \frac{\mu_0 K\ \Delta T H L^2}{\rho \nu \kappa} \tag{4.70}$$

By introducing further non-dimensional parameters the governing equations for natural and thermomagnetic convection may be considered in dimensionless form by using an

appropriate velocity scale expressed through the viscosity of the fluid given by the characteristic length, L, of the system investigated and the kinematic viscosity, ν, as ν/L. Using this approach one obtains the following non-dimensional variables

$$u' = \frac{uL}{\nu}, \quad \nabla' = \nabla L, \quad p' = \frac{pL^2}{\rho\nu^2}, \quad T' = \frac{T - T_c}{T_h - T_c}, \quad M' = \frac{M_p}{M_s}, \quad H' = \frac{\mu_0 H}{B} \tag{4.71}$$

Thus, eq.(4.66), eq.(4.67) may be expressed in non-dimensional form as

$$\nabla' \cdot \mathbf{u}' = 0 \tag{4.72}$$

$$(\mathbf{u}' \cdot \nabla')\,\mathbf{u}' = -\nabla' p' + \nabla'^2 \mathbf{u}' + \frac{T'}{\mathrm{Pr}}\left[\mathrm{Ra}\ \mathbf{e_g} + \mathrm{Ra_m}\ (\mathbf{M}' \cdot \nabla')\,\mathbf{H}'\right] \tag{4.73}$$

and the non-dimensional heat eq.(4.69) as

$$(\mathbf{u}' \cdot \nabla')\,T' = \mathrm{Pr}\ \nabla'^2\ T' \tag{4.74}$$

where $\mathbf{e_g}$ is the unit norm vector in direction of gravity.

5 Computational and experimental approach

This chapter focusses on the systems investigated to study thermomagnetic convection with and without buoyancy. The research approach and configuration used for experiments and simulations are introduced in §5.1 followed by the computational methodology in §5.2 used for numerical simulations. An introduction to the experimental methodology is given in §5.3.

5.1 Research approach and configurations used for simulation

The main focus of this thesis is the study of thermomagnetic convection by varying magnetic fields for heat transfer applications. This included the response of the magnetic fluid to magnetic and thermal forces with and without buoyancy by considering several different geometries. To study this the system geometry was split into two temperature boundary conditions that allowed a number of situations with distinct types of forcing. The temperature boundary configuration for the first panel (A) is heating form above and the second panel (B) heating from the side. These are classified into cases of distinct relative orientations of the temperature gradient, buoyancy, and Kelvin body force shown in Tab. 5.1 by varying the temperature difference, the external applied magnetic field direction and strength. The configurations with a stable thermal stratification with heating at the top (A0) and that with a horizontal temperature gradient through heating and cooling of the side walls (B0) were chosen as the non-magnetic reference cases.

Table 5.1: Configurations and parameters used for the experiment and simulations are split into two groups (A) and (B) whereas the symbols $|$, $\parallel$ and $\perp$ present the direction of applied the variables ∇H and $\mathbf{g}$ respectively.

Label	Configuration	ΔT (K)	Magnet position
A	Heated Top, cooling at bottom ∇T		
A0	Stably stratified with $\vert -\mathbf{g}$	$1 \ldots 80$	none
A1	with $\nabla H \parallel -\mathbf{g}$	$1 \ldots 80$	bottom
A2	with $-\nabla H \parallel -\mathbf{g}$	$1 \ldots 80$	top
A3	with $\nabla H \perp -\mathbf{g}$	$1 \ldots 80$	side
B	Heating and cooling at sides ∇T		
B0	Natural convection with $\vert -\mathbf{g}$	$1 \ldots 100$	none
B1	with $\nabla H \parallel -\mathbf{g}$	$1 \ldots 80$	bottom
B2	with $-\nabla H \parallel -\mathbf{g}$	$1 \ldots 80$	top
BG	with constant $\nabla H \vert$	$1 \ldots 100$	constant ∇H
BC	with constant $\nabla H \parallel -\mathbf{g}$	$1 \ldots 100$	constant ∇H

5.2 Computational methodology

The physical disciplines such as fluid flow, heat transfer and electromagnetic fields that are essential to model ferrohydrodynamic problems needed to be coupled. This thesis has therefore used a commercial solver developed by COMSOL Multiphysics [187] that was able to couple easily different physical problems and the relevant equations. This enabled not only an easy switching between the modular physical environments within COMSOL Multiphysics but additionally the option to solve equations simultaneously if needed. The used numerical method in COMSOL Multiphysics is based on the Galerkin formulation of the finite element method which will be introduced in the following sections.

5.2.1 The description of fluid motion

For the description of fluid motion, a fluid particle is defined as an element of fluid of volume, V, which contains a very large number of molecules. If this case is applicable the fluid is treated as a continuous medium. The velocity of a fluid is then the velocity of the fluid particles which is the average of the velocities of the molecules within the fluid particle. A set of velocities, $\mathbf{u}$, of fluid particles with their individual location, $\mathbf{r}$, and at time, t, a vector field $\mathbf{u}(\mathbf{r}, t)$ maybe defined. The Eulerian description of fluid motion observes the velocity, $\mathbf{u}$, of fluid particles at time, t, at a fixed position, $\mathbf{P}$. At each time step the field $\mathbf{u}(\mathbf{P}, t)$ describes the velocity of different fluid particles that pass point $\mathbf{P}$. At a later time step, t', the velocity at the same point, $\mathbf{P}$, becomes $\mathbf{u}(\mathbf{P}, t')$. The Eulerian description of fluid motion is therefore that of an observer at a fixed position in which the velocity, $\mathbf{u}$, is measured. Experimental measurements of fluid velocities corresponds to sensors that are fixed relative to the fluid flow. The fluid's velocity measured is therefore a function of time at which the measurement or observation is conducted, and of the fixed point $\mathbf{P}$ where the sensor/observer is located. In the Lagrangian description of fluid motion the observer follows the fluid particle as it moves. This is been done by specifying its position $\mathbf{P}$ at a given reference time t_0. Thus, the fluid's velocity[14], $\mathbf{v}$, is characterised as a function of the two variable position, $\mathbf{P_0}$, and time, t as $\mathbf{v}(\mathbf{P_0}, t)$. Experimental investigation that correspond to the Lagrangian description of fluid motion are carried out with instrumentations that moves with the fluid particle such as marker particles used in Particle Image Velocimetry [188]. The numerical approach to model fluid motion is introduced next.

[14]The velocity field in the Lagrangian perspective is detonated by $\mathbf{v}$ to distinguish it from the Eulerian velocity field

5.2.2 Finite-Element method

The Finite-Element method was initially developed to solve stress and displacement calculation in structural analysis. However, conjugate heat transfer problems can be solved by using the Finite Element Formulation (FEM) which uses COMSOL Multiphysics. The key feature of FEM compared to the traditional Galerkin method is the approximate solution at the nodal points written as

$$T\left(x,y,z,t\right)=\sum_{i=1}^{I}T_{i}S_{i}\left(x,y,z,t\right) \tag{5.1}$$

where T_i is the interpolated solution at the local nodal point and S_i the approximating function named shape function. A further important feature of FEM is that shape functions may be chosen from low order piecewise polynominal restricted to contiguous elements [189, 190].

Using the weighted residual method (WRM) where the interpolated solution is assumed to be represented analytically one can write e.g. for the heat conduction equation

$$L\left(\overline{T}\right)=\frac{\partial\overline{T}}{\partial t}-k\frac{\partial^{2}\overline{T}}{\partial x^{2}}=0 \tag{5.2}$$

where $\overline{T}$ is the exact solution. Using the interpolated approximation eq.(5.2) equals not zero. For the interpolated solution one can write $L\left(T\right)=R$, where R represents a continuous function of x, y, z and t from the errors caused by the approximation through interpolation. If I is sufficiently large R is small over the computational domain and the coefficient T_i is determined by

$$\int_{V}W\left(x,y,z,t\right)R\,\mathrm{d}V=0 \tag{5.3}$$

where W is the weighting function which is, by using the Galerkin method the same as the approximation function written as

$$W\left(x,y,z\right)=S_{i}\left(x,y,z\right). \tag{5.4}$$

In case where the approximation functions form a set of polynomials such as $1, x^2, x^3, ..., x^n$ indicates orthogonality of each variable in the set. Consequently the result will converge to the exact solution, $\overline{T}$ [190].

5.2.2.1 Linear interpolation

For a one-dimensional linear element the first order interpolated solution, T, between two nodes is now demonstrated. As T varies linearly between the nodal points a first order polynomial may be formulated as

$$T(x) = a + bx. \tag{5.5}$$

For the two nodel points i and $(i+1)$ one can write

$$T_i = a + bx_i \tag{5.6}$$

$$T_{i+1} = a + bx_{i+1}. \tag{5.7}$$

The coefficient a may be written as

$$a = \frac{T_i x_{i+1} - T_{i+1} x_i}{x_{i+1} - x_i} \tag{5.8}$$

and b as

$$b = \frac{T_{i+1} - T_i}{x_{i+1} - x_i}. \tag{5.9}$$

By substitution eq.(5.8) and eq.(5.9) in eq.(5.5) one obtains

$$T(x) = \frac{T_i x_{i+1} - T_{i+1} x_i}{x_{i+1} - x_i} + x\left(\frac{T_{i+1} - T_i}{x_{i+1} - x_i}\right). \tag{5.10}$$

This equation maybe re-written as

$$T(x) = T_i\left(\frac{x_{i+1} - x}{x_{i+1} - x_i}\right) + T_{i+1}\left(\frac{x - x_i}{x_{i+1} - x_i}\right) \tag{5.11}$$

where

$$S_i = \left(\frac{x_{i+1} - x}{x_{i+1} - x_i}\right) \tag{5.12}$$

$$S_{i+1} = \left(\frac{x - x_i}{x_{i+1} - x_i}\right) \tag{5.13}$$

are the interpolated linear shape functions S_i and S_{i+1}. The interpolated solution, T, at the nodal point, x, maybe written as

$$T(x) = S_i T_i + S_{i+1} T_{i+1}. \tag{5.14}$$

The use of linear interpolation imposes constraints on the approximated solutions. To obtain smaller interpolation errors a quadratic interpolation is used and introduced in the following section [190].

5.2.2.2 Quadratic interpolation

For a one-dimensional quadratic element the interpolated solution, T_x^e, has a second order polynomial written as

$$T(x) = a + bx + cx^2. \tag{5.15}$$

The quadratic interpolated solution for eq.(5.15) maybe written as

$$T(x) = S_i T_i + S_{i+1} T_{i+1} + S_{i+2} T_{i+2} \tag{5.16}$$

where the shape functions may be expressed with the used of the Lagrange interpolation function and are written as

$$S_i = \left(\frac{x - x_{i+1}}{x_i - x_{i+1}}\right)\left(\frac{x - x_{i+2}}{x_i - x_{i+2}}\right) \tag{5.17}$$

$$S_{i+1} = \left(\frac{x - x_i}{x_{i+1} - x_i}\right)\left(\frac{x - x_{i+2}}{x_{i+1} - x_{i+2}}\right) \tag{5.18}$$

$$S_{i+2} = \left(\frac{x - x_i}{x_{i+2} - x_i}\right)\left(\frac{x - x_{i+1}}{x_{i+2} - x_{i+1}}\right). \tag{5.19}$$

The use of a quadratically interpolated solution increases accuracy with the same amount of nodal points compared to the linear interpolation. By increasing the amount of quadratic elements the rms[15] error decreases. Consequently the solution of a quadratic interpolation is more accurate as a linear interpolation by using a refined element grid. However, higher-order interpolations give more accurate solutions but are in practice more expensive in computational time. To achieve a good balance of accuracy and computational resources a second order interpolation is in most applications sufficient [190].

5.3 Experimental methodology

As magnetic fluids are opaque it is challenging to visualise flow structures in them. A powerful optical tool to visualise complex flow patters, such as evaluating wall convective heat flux or surfaces flow fields, is utilised by infrared thermography. In general thermal imaging of a fluid's temperature field is easily accomplished in convection experiments with

[15] rms: Root-mean-square deviation is the average of the square of the measured difference between the observed values and the calculated values of a model.

free surface and can be used for complex fluid flows [191]. The experimental methodology of infrared thermography is based on the principle of radiative heat transfer which is an energy transport mechanism that appears in the form of electromagnetic waves. Those electromagnetic waves travel through free space and may be absorbed, reflected or even transmitted through a body. The law that describes radiative energy flux per wavelength, λ, is the *Planck's law of radiation* emitted by a black body and written as

$$I_b(\lambda) = \frac{C_1}{\lambda^5 \left(e^{C_2/\lambda T} - 1\right)} \tag{5.20}$$

where λ is the wavelength in metre, $C_1 = 3.7417 \times 10^{-16}$ Wm^2 and $C_2 = 1.4388 \times 10^{-2}$ mK are the first and second universal constants respectively and T the temperature. Thus, the temperature of a black body is a function of the wavelength and its emitted maximum spectral emissive power may be represented by *Wien's displacement law* written as

$$\lambda_b \, T = 2897.8 \mu\text{m-K} \tag{5.21}$$

where λ_b is the wavelength of radiation emitted by a black body. The law states if a body's temperature increases the wavelength reduces. As the total emitted energy by a black body depends on its temperature alone the total emissive power may be calculated by the *Stefan-Boltzmann law* given by

$$E_b = \sigma T^4. \tag{5.22}$$

However, infrared thermography only captures a limited electromagnetic spectrum as in most cases real objects only emit a fraction of the radiation of a black body. Thus, *Planck's law* needs to be considered by introducing the spectral emissivity coefficient, ϵ, written as

$$\epsilon(\lambda) = \frac{I(\lambda)}{I_b(\lambda)} \tag{5.23}$$

and the *Planck's law* may be extended for real objects to

$$I(\lambda) = \epsilon(\lambda) \frac{C_1}{\lambda^5 \left(e^{C_2/\lambda T} - 1\right)}. \tag{5.24}$$

As the environmental conditions at which the experiment is carried out may lead to measurement errors in the process of recording thermography images the detected radiation, I', by the infrared radiometer need to be corrected. By considering the uncertainties, the

camera may be calibrated by using the following equation

$$I' = \tau_r \, \epsilon \, I_{b,\, obj} + \tau_r \ (1 - \epsilon) \, I_{b,\, amb} + (1 - \tau_r) \, I_{b,\, atm} \tag{5.25}$$

where τ_r is the transmissivity of the atmosphere between the objects surface and the radiometer, $\tau_r \, \epsilon \, I_{b,\, obj}$ the surface emission captured by the infrared radiometer, $\tau_r \ (1 - \epsilon) \, I_{b,\, amb}$ is the emission reflected by ambient sources and $(1 - \tau_r) \, I_{b,\, atm}$ the atmospheric emission. The emissive power received by the radiometer per square metre may be written as

$$E' = \tau_r \, \epsilon \, \sigma T_{obj}^4 + \tau_r \, (1 - \epsilon) \, \sigma T_{amb}^4 + (1 - \tau_r) \, \sigma T_{atm}^4 \tag{5.26}$$

where T_{obj} is the object's temperature, T_{amb}^4 the ambient temperate and T_{atm}^4 is assumed as a constant temperature of the emitted surface from the half sphere of the object. As the electromagnetic spectra of wavelength intervals is divided into bands it is important to select the correct radiation detector that is sensitive for the specific band. The infrared band is found at a wavelength of 0.75 to 1,000 μm and presents a temperatre range of 3-3864 K [192]. A thermal camera detector that is sensitive to the band is then used to record the incident energy flux to generate the thermal images.

6 Natural and thermomagnetic convection

A commercial magnetic fluid was used to study natural and thermomagnetic convection with constant magnetic field gradient by numerical simulation in a square cavity. The working fluid was a mineral oil based magnetic fluid with dispersed magnetite particles. As only limited information was available, the physical properties of the working fluid had to be estimated. Thus, the numerical model used a mixture magnetic fluid model to estimate the physical properties of the nano particles and the carrier fluid. The density, ρ, of the fluid was estimated by eq.(2.33), the thermal conductivity, k, by eq.(2.37), the heat capacity, c_p, by eq.(2.34) the thermal expansion coefficient, β, by eq.(2.36) and the kinematic viscosity, ν by eq.(2.38). All individual physical properties of the dispersed magnetic particles, the carrier fluid and the mixture magnetic fluid are summarised in Tab. 6.1 where the solid dispersed particles are denoted with the subscript (s) and the carrier fluid as (f), respectively.

6.1 Model formulation

The system investigated was a non-dimensional square cavity filled with the mixture magnetic fluid. The cavity was thermally forced at the two opposite vertical walls which were kept at two constant temperatures of T_h and T_c respectively with $T_h > T_c$ following configuration (B). All remaining walls were thermally insulated. Figure 6.1 presents the problem geometry and its temperature and velocity boundary conditions. To compare natural convection and thermomagnetic convection under a constant magnetic field gradient three configurations were studied. In the first configuration (B0) the magnetic fluid was only subjected to buoyancy to study natural convection whereas in the second configuration (BG) the fluid was only subjected to the Kelvin body force to study thermomagnetic convection. The third study with configuration (BC) combined natural and thermomangetic convection and both buoyancy and Kelvin body force were active. A set of non-dimensional parameters were used to characterise heat transfer by natural and

Table 6.1: Fluid properties, estimated for numerical simulations.

Property	Value	Property	Value	Property	Value
ρ_s	5175 kg/m^3	ρ_f	838 kg/m^3	ρ	1272 kg/m^3
k_s	0.29 W/(m·K)	k_f	0.1107 W/(K·m)	k	0.129 W/(m·K)
$c_{p.s}$	151 J/(kg·K)	$c_{p.f}$	1710 J/(kg·K)	c_p	1554 J/(kg·K)
β_s	0.13×10^{-4} K^{-1}	β_f	6.4×10^{-4} K^{-1}	β	3.85×10^{-4} K^{-1}
m	2.93×10^{-25} J·m/A	μ_f	2.0912×10^{-2} Pa·s	μ	2.614×10^{-2} Pa·s
M_d	423 kA/m	ν_f	2.495×10^{-5} m^2/s	ν	2.055×10^{-5} m^2/s
ϕ	0.1	$\mathrm{Pr_f}$	323	Pr	316

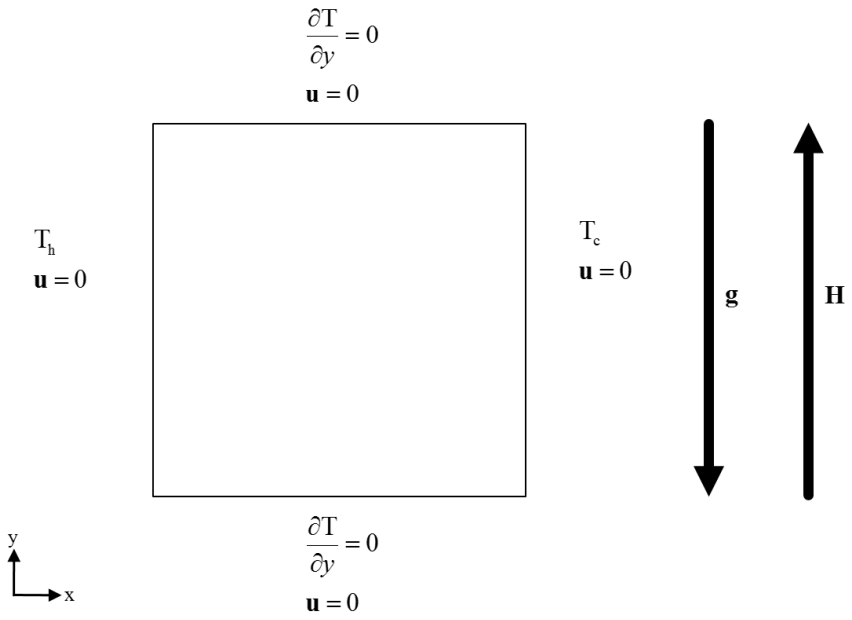

Figure 6.1: Problem geometry with boundary conditions for temperature and velocity.

thermomagnetic convection which are now introduced in the following section.

6.1.1 Governing equations

The governing equations for natural and thermomagnetic convection eq.(4.66-4.69) may be considered in non-dimensional form by introducing a suitable reference scale as men-
1095 tioned in §4.5.1. Using the following approach the resulting non-dimensional eq.(4.72-4.74) maybe rearrange from their vector notation and one obtains for the non-dimensional continuity equation

$$\frac{\partial u'}{\partial x'} + \frac{\partial v'}{\partial y'} = 0 \tag{6.1}$$

the non-dimensional momentum equation

$$u'\frac{\partial u'}{\partial x} + v'\frac{\partial u'}{\partial y} = -\frac{\partial p'}{\partial x} + \left(\frac{\partial^2 u'}{\partial x^2} + \frac{\partial^2 u'}{\partial y^2}\right) + \frac{T'}{\mathrm{Pr}}\,\mathrm{Ra_m}\left(M'_x\frac{\partial H'_x}{\partial x} + M'_y\frac{\partial H'_x}{\partial x}\right) \tag{6.2}$$

$$u'\frac{\partial v'}{\partial x} + v'\frac{\partial v'}{\partial y} = -\frac{\partial p'}{\partial y} + \left(\frac{\partial^2 v'}{\partial x^2} + \frac{\partial^2 v'}{\partial y^2}\right) + \frac{T'}{\mathrm{Pr}}\left[\mathrm{Ra} + \mathrm{Ra_m}\left(M'_x\frac{\partial H'_y}{\partial y} + M'_y\frac{\partial H'_y}{\partial y}\right)\right] \tag{6.3}$$

and the non-dimensional heat equation

$$u'\frac{\partial T'}{\partial x} + v'\frac{\partial T'}{\partial y} = \mathrm{Pr}\left(\frac{\partial^2 T'}{\partial x^2} + \frac{\partial^2 T'}{\partial y^2}\right) \tag{6.4}$$

Table 6.2: Numerical benchmark for natural convection [193].

Input value Rayleigh no	Vahl Davis Nusselt no	Mesh Size Normal Nusselt no	difference	Mesh Size Finer Nusselt no	difference
10^3	1.116	1.1177	0.15%	1.1178	0.16%
10^4	2.234	2.2489	0.67%	2.2453	0.51%
10^5	4.510	4.5447	0.76%	4.5245	0.32%
10^6	8.798	8.8734	-0.18%	8.8573	0.67%

where Ra is the conventional Rayleigh number in eq.(4.65), $\mathrm{Ra_m}$ the magnetic Rayleigh number in eq.(4.70) and Pr the Prandtl number in eq.(4.60). The heat transfer was quantified by the Nusselt number, Nu, and is presented in eq.(4.64).

6.2 Computational methodology and numerical input

The numerical model was solved by using a Finite-Element technique. Two triangular meshes were generated by COMSOL Multiphysics [187] using the inbuilt physical controlled sequence type. The normal mesh size had a total of 1,264 elements and the finer mesh size a total of 5,998 elements repectively. Both meshes were tested by comparison with de Vahl Davis [193] benchmark solution of natural convection of air with a Prandtl number of 0.71. The numerical solutions were performed by solving the non-dimensional eq.(6.1), eq.(6.2) and eq.(6.4) using the Rayleigh number, Ra, as an input value presented in Tab. 6.2. As no magnetic forces were applied to the benchmark model and only gravity was present the magnetic Rayleigh number, $\mathrm{Ra_m}$, was kept at zero value. The velocity and thermal boundary conditions were expressed in non-dimensional form such that the temperature for the left wall was $T' = 1$ and $T' = 0$ for the right wall. Velocity conditions were no-slip at all side walls. Initial conditions for all numerical simulations were a stagnant fluid with a uniform distributed temperature of $T' = 0$ and a dimensionless gauge pressure of $p_0 = 1$ applied on the bottom left corner of the cavity. The numerical simulation of the finer mesh size obtained sufficient accurate results for an adequate computational time and are presented for both meshes distributions in Tab. 6.2.

As the benchmark test obtained sufficiently accurate results the simulation with the magnetic fluid was investigated for all study cases. In the first configuration (B0) natural convection of a magnetic fluid was investigated. To solve the dimensionless continuity eq.(6.1), momentum eq.(6.2) and heat eq.(6.4) a set of different temperature differences across the system was studied. The fluid temperature, T, written as

$$T = \Delta T\, T' + T_0 \tag{6.5}$$

where T_0 is the reference temperature defined as the temperature of the cold side wall, was used to calculate the dimensionless Rayleigh number which was used as an input parameter.

An equivalent approach was used for study case (BG) where only the Kelvin body force was present. The temperature, T, and a set of different constant magnetic field gradients provided the magnetisation, M_p, eq.(2.24) and the pyromagnetic coefficient, K, eq.(4.68) to calculate the magnetic Rayleigh number eq.(4.70) to study thermomagnetic convection. In the combined natural and thermomagnetic case (BC) both conventional Rayleigh and magnetic Rayleigh numbers were calculated simultaneously as was written above and used as input parameters to solve the non-dimensional equations (6.1-6.4).

6.3 Results

This section presents the computed results of temperature and velocity fields for natural convection (B0) in §6.3.1 and thermomagnetic convection (BG) in §6.3.2 followed by combined natural and thermomangetic convection (BC) in §6.3.3. An analysis of the resulting heat transfer is addressed in §6.4.

6.3.1 Natural convection of magnetic fluid

The results for the first configuration (B0) are obtained in the absence of magnetic forces and only gravity is active. The resulting natural convection is presented in Fig. 6.2. The computed results present the dimensionless temperature and velocity profiles for $\mathrm{Ra} = 3.5 \times 10^5$ in the top row and $\mathrm{Ra} = 3.5 \times 10^6$ in the bottom row. This solution is then used to benchmark the effect of magnetic forces for configurations (BG) and (BC). Figure 6.2(a) with a contour map of the temperature shows the magnetic fluid heated at the left side wall where regular natural convection is present. The corresponding velocity magnitude shown in Fig. 6.2(b) presents a single domain-filling convection cell. The arrows indicate that the fluid ascends at the heated side wall and descends near the cold side wall whereas the fluid in the centre of the domain is relatively quiescent. An increase in Ra presented in Fig. 6.2(c) shows a decrease in the temperature boundary layers and a more stratified fluid interior. This is also evident by the velocity profile presented in Fig. 6.2(d) where an increase in convective flow is observed.

6.3.2 Thermomagnetic convection with constant magnetic field gradient

The second configuration (BG) simulated thermomagnetic convection in the absence of gravitational forces. As only the Kelvin body force is active a set of different constant

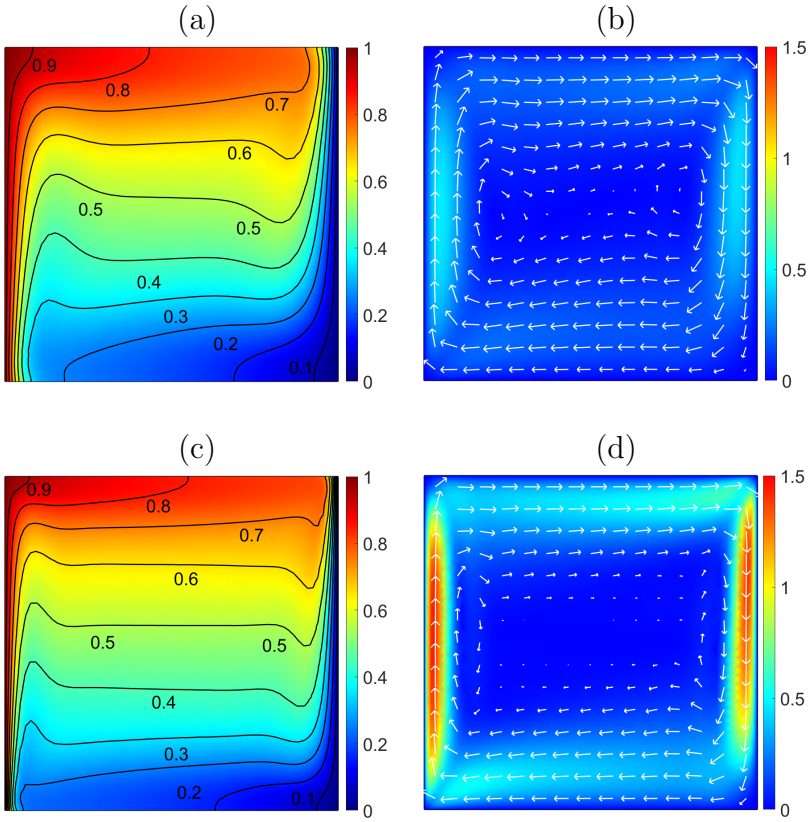

Figure 6.2: Non-dimensional temperature fields (left) and velocity fields (right) for Ra= 3.5×10^5 in the top row and Ra= 3.5×10^6 in the bottom row using configuration (B0).

magnetic field gradients are investigated to study the response and fluid flow patterns of the magnetic fluid. Results presented in Fig. 6.3 are in their non-dimensional form for temperature (left) and velocity (right). Figure 6.3 (a) presents the temperature profile for a constant magnetic field gradient of 10^3 A/m^2 that is indicative of convective heat transfer. The velocity magnitude together with a set of arrows shown in Fig. 6.3 (b) correspond to the temperature profile and present a counter-rotating single convective cell compared to the natural convection case (B0) in Fig. 6.2 (b, d). The observed thermoconvective flow can be interpreted such that colder more magnetised fluid from the cold side wall moves towards higher magnetic field intensity to displace less magnetised warmer fluid. By increasing the magnetic field gradient to 10^4 A/m^2 seen in the second row of Fig. 6.3 thermomagnetic convection increases in the top of the fluid domain whereas the bottom is little affected. The difference arises out of the intensity of the magnetic field gradient that magnetise the fluid and creates a corresponding magnetisation gradient across the cavity. As the magnetic field intensity decreases with distance the magnetic fluid at the bottom of the cavity is less magnetised and does not achieve magnetic saturation such that the convective cell is unable to developed through the full domain. A further in-

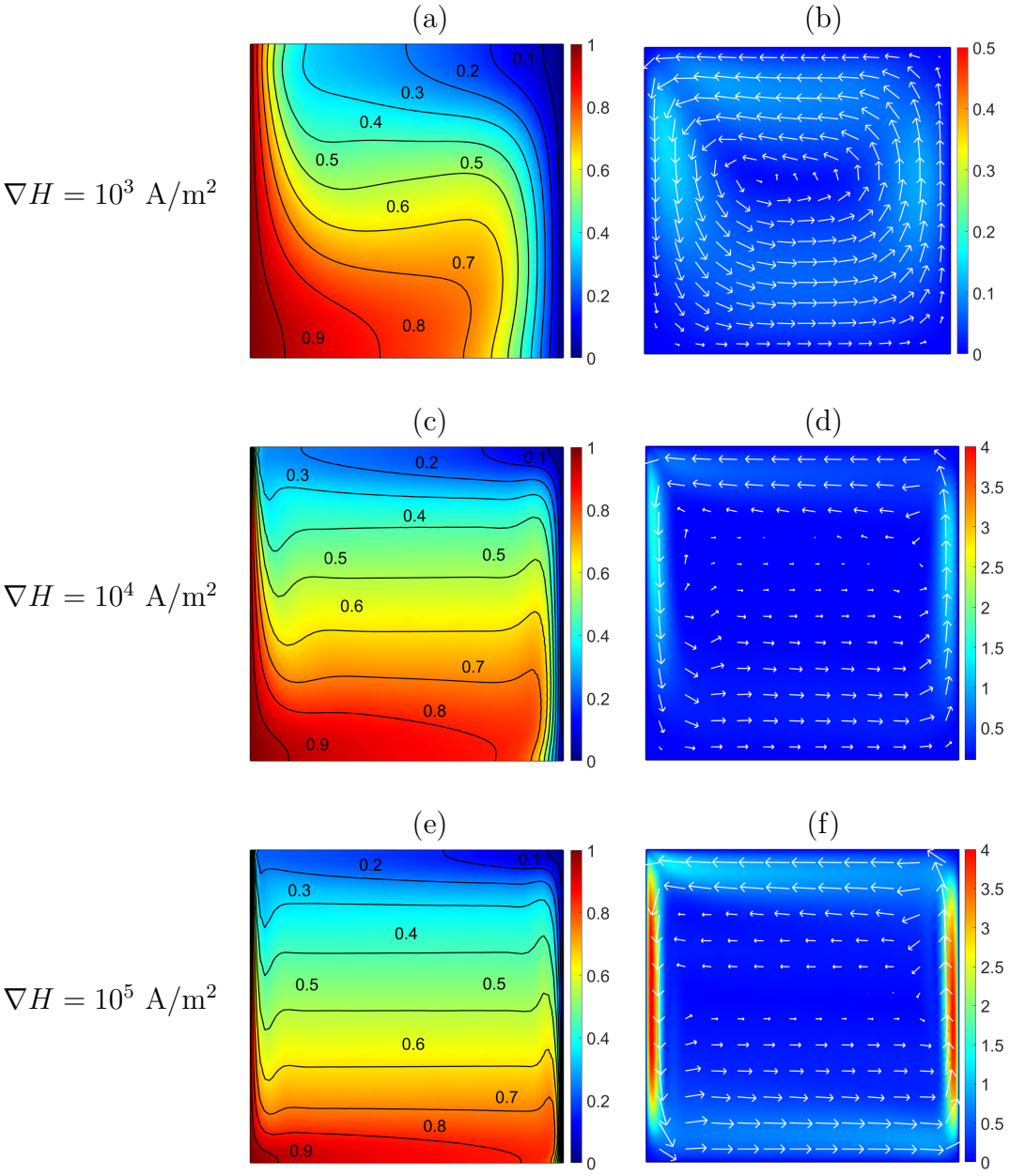

Figure 6.3: Non-dimensional temperature fields (left) and velocity fields (right) for $\mathrm{Ra}_m = 1 \times 10^5$ (top row), $\mathrm{Ra}_m = 8.5 \times 10^5$ (middle row) and $\mathrm{Ra}_m = 3.4 \times 10^7$ (bottom row) at a temperature difference of 10 K using configuration (BG).

crease in magnetic field gradient to 10^5 A/m^2 presented in the bottom row of Fig. 6.3 increases the magnetic field intensity and the overall fluid domain is closer to its saturation point and the convective cell expands through the whole cavity resulting in a stronger thermoconvective flow.

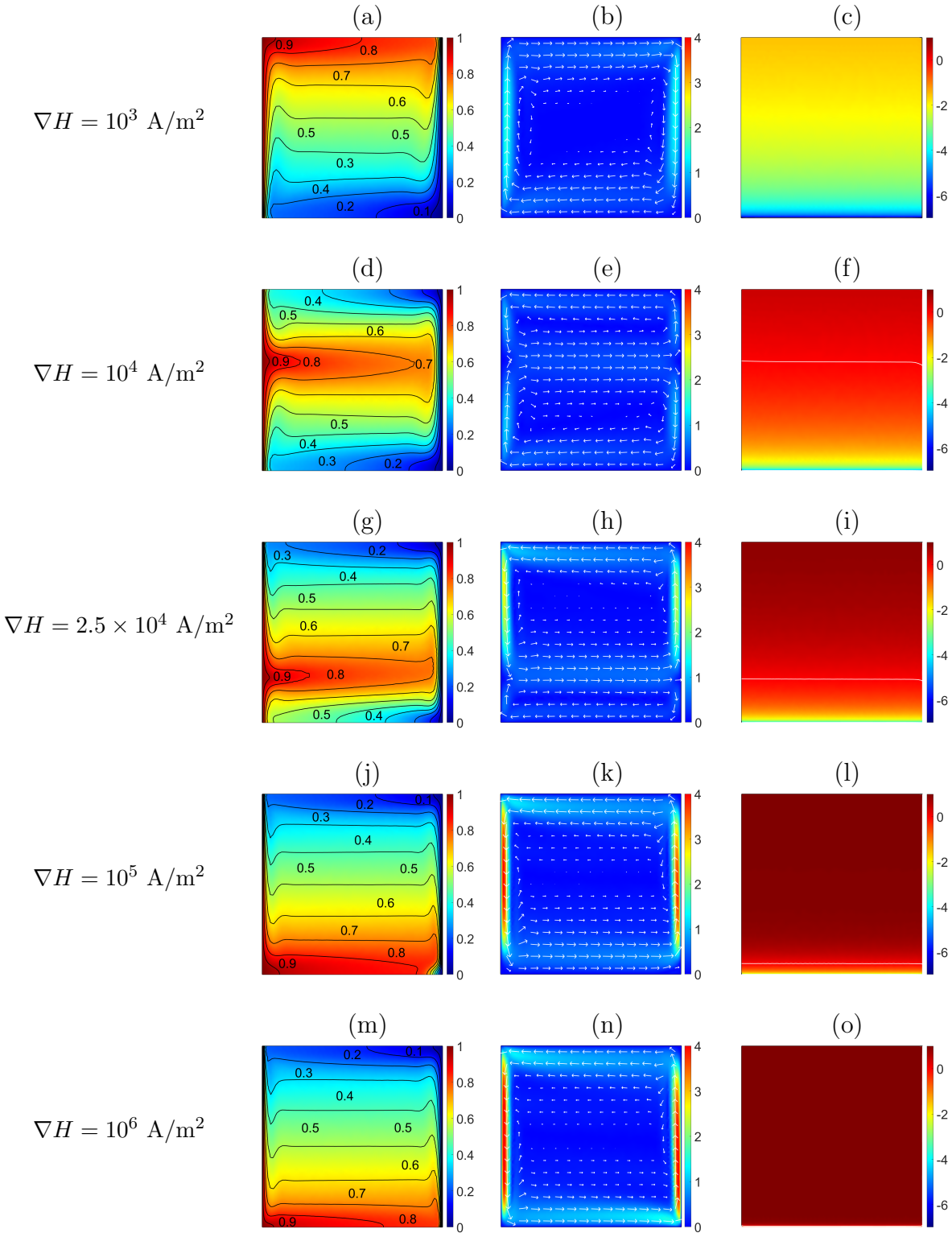

Figure 6.4: Non-dimensional temperature fields (left), velocity fields (middle) and force ratio, r (right) using configuration (BG).

6.3.3 Combined natural and thermomagnetic convection under constant magnetic field gradient

The third configuration (BC) simulated a combination of natural and thermomagnetic convection and both buoyancy and Kelvin body force are present. The results for different intensities of the magnetic field gradient are presented in Fig. 6.4. When the weakest field gradient is applied the magnetic fluid is magnetised resulting in the additional Kelvin body force eq.(4.43) but had no significant influence to induce a change in the already established natural convection cell presented in Fig. 6.4(a) for temperature and (b) for velocity. To get an indication of the acting body forces that drive the combined convection, a measure of their local ratio may be defined as

$$r = \log_{10}\left(\frac{\mathrm{Ra_m}}{\mathrm{Ra}}\right) \tag{6.6}$$

and is plotted for all applied magnetic field gradients in the right row of Fig. 6.4. A value grater then zero implies that the Kelvin body force is dominant in that part of the fluid domain whereas a value less than zero buoyancy dominates. If r equals zero both forces are equal and is presented with a black contour line.

For the weakest magnetic field gradient the force ratio, r, is presented in Fig. 6.4(c) and is negative in whole domain and convection is dominated by buoyancy. By applying a stronger magnetic field gradient of 10^4 A/m^2 the Kelvin body force increases and a change in convection is observed. The temperature profile presented in Fig. 6.4(d) changed significantly compared to the weakest field gradient and is a result of a change in convective flow where a second counter-circulating cell is established in the top part of the domain and has pushed the original convection cell in Fig. 6.4(b) downwards as can be seen in the velocity profile in Fig. 6.4(e). Evaluating the force ratio, r, presented in Fig. 6.4(f) indicates that the top part of the fluid domain is dominated by the Kelvin body force as $r > 0$ and creates a thermomagnetically induced convection cell whereas the bottom cell is still dominated by buoyancy $r < 0$ and regular natural convection is present. Increasing the magnetic field gradient to 2.5×10^4 A/m^2 increases the Kelvin body force. This is presented in 6.4(i) where r increases throughout the complete domain compared to 6.4(f) and the thermomagnetically induced convection cell expands further downwards such that the buoyancy dominated region decreases as can be seen in 6.4(g) and (h). A further increase in magnetic field gradient gradually increases the Kelvin body force and the thermomagnetic induced convection cell expands in the fluid domain. For a magnetic field gradient of 10^5 A/m^2 the Kelvin body force exceeds buoyancy everywhere except in a

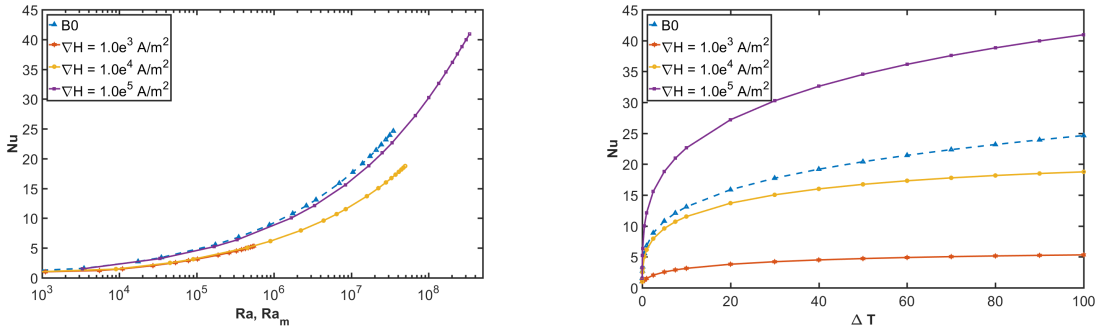

(a) (b)

Figure 6.5: The Nusselt number, Nu, plotted versus the Rayleigh numbers in (a) and versus the temperature difference in (b) for configuration (B0) and (BG).

small part in the bottom of the domain resulting in a fluid domain that is fully dominated by one thermomagnetically induced convection cell presented in Fig. 6.4(j-l). While the separator of r shifts further down with each increase in Kelvin body force, the force ratio at the top of the domain does not increase significantly further as is evident in Fig. 6.4(o). This relates to the saturation level of the magnetic fluid as the pyromagnetic coefficient, K, is weakening when the fluid gets closer to magnetic saturation and thermomagnetic convection increase moderate until the fluid is fully saturated as shown in Fig. 6.4(m) and (n).

6.4 Discussion

The heat transfer across the cavity is quantified by the Nusselt number, evaluated according eq.(4.64), and plotted versus the Rayleigh for case (B0) and magnetic Rayleigh number for case (BG) in Fig. 6.5(a) and their corresponding temperature differences in

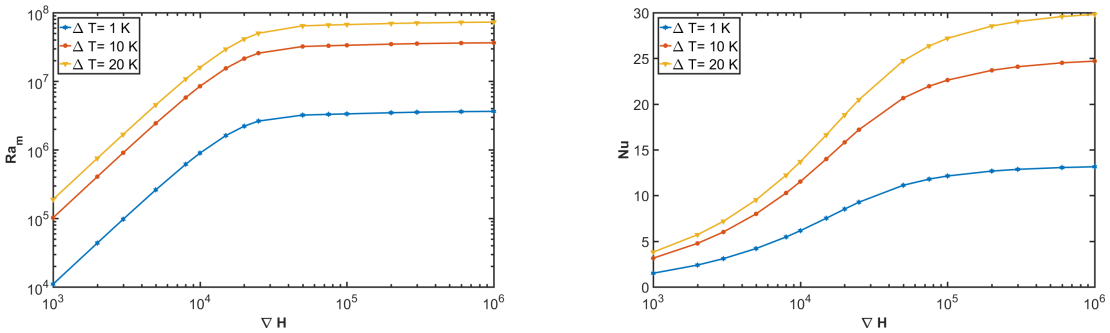

(a) (b)

Figure 6.6: The magnetic field gradient, ∇H, plotted versus the Nusselt number, Nu, in (a) and the magnetic Rayleigh number in (b) for configuration (BG).

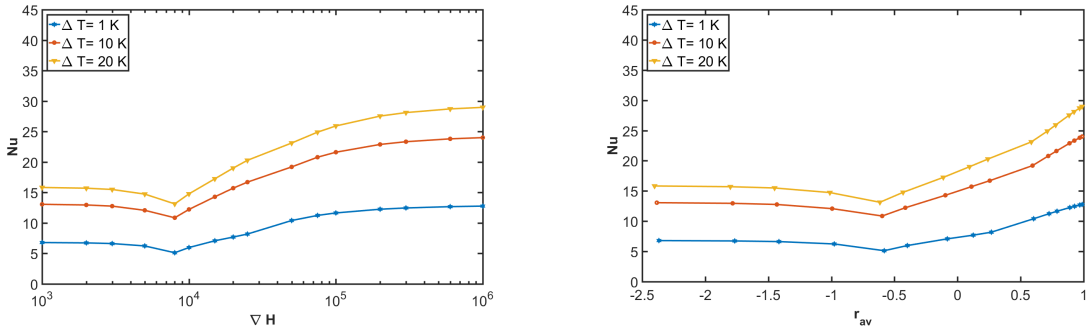

(a) (b)

Figure 6.7: The Nusselt number, Nu, plotted versus the magnetic field gradient, ∇H, in (a) and the body force ratio, r, in (b) for configuration (BC).

Fig. 6.5(b). The natural convection case (B0) of the magnetic fluid provided the benchmark solution for three applied magnetic field gradients with different intensities that induced thermomagnetic convection in study case (BG). The results suggest that heat transfer is increased by all applied magnetic field gradients compared to the conduction only case. However, the intensity differs between each magnetic configuration and refers to the strength of the applied magnetic field gradient, ∇H. By applying a magnetic field gradient of 10^5 A/m^2 thermomagnetic convection is even stronger than natural convection. Fig. 6.5(b) reflects the results of an increasing Nusselt number when temperature or ∇H increases. The thermomagnetic effect can be explained by interpreting Fig. 6.6(a). There, the effect on the Nusselt number is plotted versus ∇H for three different temperature differences. As can be seen a weak ∇H leads to a small Kelvin body force according to eq.(4.43) and heat transfer by thermomagnetic convection is relatively small. When ∇H increases the Kelvin body force becomes stronger and heat transfer by thermomagnetic convection is getting more intense represented in a rise of Nusselt number. When the magnetic fluid reaches its saturation magnetisation, M_s, the increase in Nusselt number is more moderate. This effect is also evident in Fig. 6.6(b) where the magnetic Rayleigh number increases with ∇H until a more moderate state as the pyromagnetic coefficient reduces when the magnetic fluid reaches magnetic saturation.

When both buoyancy and Kelvin body force are present, as it is in configuration (BC), the heat transfer across the cavity varies due to a transition region caused by the intensity of the applied magnetic field gradient. The effect of magnetic fields is understood by the model setup as gravity and Kelvin body force oppose each other. Thus, the magnetic field effect on the Kelvin body force would be in some cases the dominant factor that cause a significant change in the convective structure presented in Fig. 6.4 and in other cases only in part of the domain. As the buoyancy dominated fluid domain is significantly influenced

by the thermomagnetically induced Kelvin body force a drop in Nusselt number for the first magnetic configurations is observed compared to the non-magnetic configuration (B0) and is presented in Fig. 6.7(a). The drop can be explained by Fig. 6.4(e) and shows that the original natural convection cell in Fig. 6.4(b) was effectively reduced and pushed downwards by a thermomagnetically convection cell that appeared in the top of the fluid domain. This is also evident by comparing the velocity magnitude of both Fig. 6.4(b) with (e) where the convective flow reduced. The results in Fig. 6.4(a-o) present a transition region of a single buoyancy dominated convection cell via a two-cell structure to a single Kelvin body force dominated cell. Fig. 6.7(a) reflects the global effect in heat transfer across the cavity with a minimum in Nusselt number in the transition region.

To quantify the effect of competing body forces on heat transfer, an averaged force ratio, r_{av}, may be developed over the entire fluid domain written as

$$r_{av} = \frac{1}{A} \int r dA \tag{6.7}$$

and is plotted versus the Nusselt number in Fig. 6.7(b). With the weakest field gradient the Kelvin body force is small and does not exceed buoyancy in the fluid domain but has already an effect on heat transfer. As both body forces oppose each other their averaged force ratio, r_{av}, increases and the Nusselt number starts decreasing. When the field gradient is increased to $8{\times}10^3$ A/m^2 the Nusselt number reaches its minimum as the Kelvin body force is suppressing buoyancy without being able to contribute to heat transfer. By applying a magnetic field gradient of 10^4 A/m^2 the Nusselt number starts to increase. As r is still negative the overall heat transfer is still primarily driven by buoyancy. This changes when r gets positive indicating that heat transfer is primarily driven by the Kelvin body force.

6.5 Summary

The first study case (B0) simulated natural convection using a magnetic fluid and was used to benchmark the effect of thermomagnetic convection in the second study case (BG) and a combined study case (BC) were both buoyancy and Kelvin body force were present. The parametric study included the heat transfer that was influenced by the magnetic field intensity and the temperature difference across the system. A magnetic Rayleigh number was developed to characterise thermomagnetic convection and represents the empirical equivalent to natural convection to its respective Rayleigh number. By combining buoyancy and Kelvin body force in study case (C) a transition region from

natural to thermomagnetic convection was found. As the effective driving force of the combined convection varied substantially over the fluid domain a body force ratio, r, was developed and a surface averaged force ratio, r_{av}. The presented numerical analysis extend the studies by Snyder et al. [135] and was able to explain the transition of natural convection to thermomagnetic convection found in experiments by Sawada et al. [134]. The computed results present that flow structures were organised into distinct convection cells driven either by buoyancy or the Kelvin body force. The force ratio, r, in eq.(6.6) suggest a separator between both convection cells when both body forces are equal. The result in flow and heat transfer structure was a gradual transitional process where the spatial extent of one convection cell gradually increases at the expense of the other.

7 Infrared thermography of magnetic convection

Infrared thermography was used to investigate experimentally thermomagnetic convection in the presence of buoyancy and validated by a numerical finite-element model. The experimental perspex cavity filled with a commercially magnetic fluid was thermally forced at two opposite walls with different temperatures and subjected to a magnetic field generated by a permanent magnet. The size of the magnet was chosen to investigate the convective behaviour of a magnetic fluid in spatially non-uniform magnetic fields. The temperature conditions imposed were such that the magnetic fluid would either result in a stagnant, stably stratified fluid or in regular natural convection when buoyancy was present. The permanent magnet was placed in three different configuration, at the top, at the bottom and at the side of the cavity to study thermomagnetic convection where buoyancy and Kelvin body force were parallel or perpendicular to each other. The theory of the experimental methodology of infrared thermography were presented in detail in §5.3. As there was no information given by the manufacturer of the magnetic fluid the physicals properties had to be estimated and were the same as used in the previous studies presented in Tab. 6.1 for a mixture magnetic fluid model.

7.1 Model formulation

The model formulation in this section presents the theoretical formulation, the experimental setup and the computational methodology based on the experiment. The numerical model was set-up according to the experimental specifications such that the temperature and velocity boundary conditions corresponded to those who are presented in the left panel of Fig.7.1 in the experiment. The temperature boundary conditions for study case (A) was a heated cavity from the left with $T_h = T_c + \Delta T$ where $T_c = 290$ K and was the temperature of the cooled opposite side wall. All other side walls were kept adiabatic. For study case (B) the cavity was rotated by 90 deg. The boundary conditions for velocity were no-slip at all side walls for all configurations. Zero pressure point constraint was applied at the left top corner of the fluid domain. The initial conditions for all computations carried out were a uniform distributed temperature T_c, an initial gauge pressure and a stagnant fluid.

7.1.1 Theoretical formulation

As the magnetic fluid does not induce electromagnetic current and is considered non-conductive the magnetic field of the permanent magnet may be calculated with the

magneto-static Maxwell's equations for non-conductive materials which are presented in eq.(4.10) and eq.(4.11). The resulting static magnetic induction field, $\mathbf{B}$, may be written as

$$\mathbf{B} = \mu_0 \left(\mathbf{H} + \mathbf{M_M} \right) \tag{7.1}$$

where μ_0 is the permeability of free space, $\mathbf{H}$ the magnetic field and $\mathbf{M_M}$ the magnetisation of the magnetic material. Thus, the magnetisation of the permanent magnet is calculated using the remanent flux density, $\mathbf{B_r}$, written as $\mathbf{M_M} = \mathbf{B_r}/\mu_0$. The magnetic field, $\mathbf{H}$, within the cavity is calculated using the initial Langevin susceptibility modified by Pshenichnikov et al. [47,48] to take inter-particle interaction into account and is presented in eq.(2.25). Hence, the magnetic field within the fluid domain may then be calculated by

$$\mathbf{H} = \frac{\mathbf{B}}{\mu_0 \left(1 + \chi_P \right)} \tag{7.2}$$

and conforms to the magneto-static Maxwell's equations. The magnetisation of the magnetic fluid may then be calculated using eq.(2.24) with the fluid temperature, T, and the magnetic field, $\mathbf{H}$.

The fluid flow and heat transport equations may be rearranged from vector notation as follows for the continuity eq.(4.66)

$$\frac{\partial u}{\partial x} + \frac{\partial v}{\partial y} + \frac{\partial w}{\partial z} = 0 \tag{7.3}$$

the momentum eq.(4.67)

$$u\frac{\partial u}{\partial x} + v\frac{\partial u}{\partial y} + w\frac{\partial u}{\partial z} = -\frac{\partial p}{\partial x} + \nu \left(\frac{\partial^2 u}{\partial x^2} + \frac{\partial^2 u}{\partial y^2} + \frac{\partial^2 u}{\partial z^2} \right) + \mu_0 K \Delta T \frac{H}{\partial x} \tag{7.4}$$

$$u\frac{\partial v}{\partial x} + v\frac{\partial v}{\partial y} + w\frac{\partial v}{\partial z} = -\frac{\partial p}{\partial y} + \nu \left(\frac{\partial^2 v}{\partial x^2} + \frac{\partial^2 v}{\partial y^2} + \frac{\partial^2 v}{\partial z^2} \right) + \mu_0 K \Delta T \frac{H}{\partial y} \tag{7.5}$$

$$u\frac{\partial w}{\partial x} + v\frac{\partial w}{\partial y} + w\frac{\partial w}{\partial z} = -\frac{\partial p}{\partial z} + \nu \left(\frac{\partial^2 w}{\partial x^2} + \frac{\partial^2 w}{\partial y^2} + \frac{\partial^2 w}{\partial z^2} \right) + \Delta T \left(\beta g + \mu_0 K \frac{H}{\partial z} \right) \tag{7.6}$$

and heat eq.(4.69)

$$u\frac{\partial T}{\partial x} + v\frac{\partial T}{\partial y} + w\frac{\partial T}{\partial z} = \kappa \left(\frac{\partial^2 T}{\partial x^2} + \frac{\partial^2 T}{\partial y^2} + \frac{\partial^2 T}{\partial z^2} \right). \tag{7.7}$$

7.1.2 Non-dimensional parameters

This section introduces the main non-dimensional parameters for heat transfer by combined natural and thermomagnetic convection. A quantitative non-dimensional parameter to characterise natural convection is presented by the Rayleigh number, Ra, in eq.(4.65) and its equivalent for thermomagnetic convection the magnetic Rayleigh number in eq.(4.70). Both quantitative non-dimensional parameters are explained in detail in §4.4 and §4.5.1 respectively.

To attempt a characterisation of combined natural and thermomagnetic convection an overall force balance of the two additive body force terms can be defined by using appropriate non-dimensional parameters. An adequate framework for a quantitative comparison may be developed by using a modified Rayleigh number, Ra^*, that takes the relative orientation of each body force into account. For configuration (A1) and (B1) where the magnetic field gradient in the same direction to gravity Ra^* is calculated as a sum of the natural and thermomagnetical part. For configuration (A2) and (B2) where the magnetic field gradient is in opposite direction to gravity, the Ra^* is calculated as a net difference of the natural and thermomagnetical part. By using configuration (A3) where the magnetic field gradient is horizontal and is perpendicular to gravity the net effect may be calculated as a vector sum. Thus, the modified Rayleigh number for each configuration is calculated in the following manner

$$\mathrm{Ra}^* = \begin{cases} \mathrm{Ra} + |\mathrm{Ra_m}| & \text{for A1 and B1} \\ |\mathrm{Ra} + \mathrm{Ra_m}| & \text{for A2 and B2} \\ \sqrt{\mathrm{Ra}^2 + {\mathrm{Ra_m}}^2} & \text{for A3} \end{cases} \tag{7.8}$$

To compare experimental and computational results for combined natural and thermomagnetic convection further non-dimensional parameters may be introduced by using a suitable reference scale introduced in §4.5.1. Using this approach the following dimensionless variables

$$\mathbf{u} = \frac{\mathbf{u}L}{\nu}, \quad \nabla' = \nabla L, \quad T' = \frac{T - T_c}{T_h - T_c} \tag{7.9}$$

are introduced.

7.2 Experimental setup

The experiment was carried out in August 2015 at the Faculty of Electrical Engineering and Computer Sciences, University of Maribor, Slovenia. The focus on the experiment

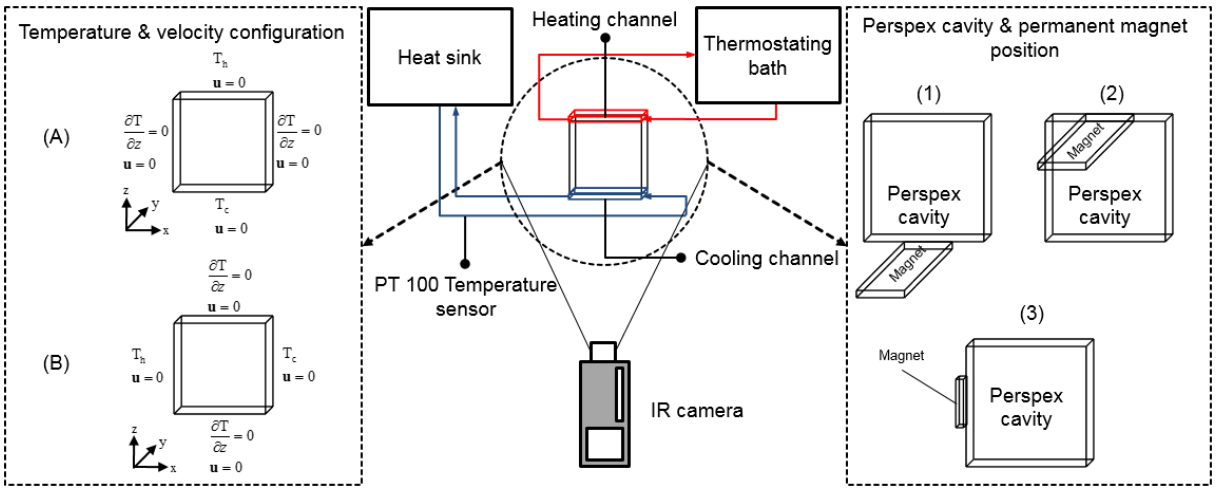

Figure 7.1: Schematic view of experimental apparatus (middle), with temperature and velocity configurations (left) and permanent magnet configuration (right).

was to study convective heat transfer in a cavity filled with a magnetic fluid by surface visualisation of the temperature field through one of the cavity walls made of thin perspex. As the perspex cavity absorbs most of the thermal infrared radiation, the monitored surface temperature was in fact that of the perspex surface whose temperature reflects the fluid through heat conduction. The apparatus and system dimensions of the cavity, the specifications of the infrared system and data acquisition are introduced in the flowing sections.

7.2.1 Apparatus and system dimensions

Figure 7.1 presents a schematic view of the experimental apparatus. The measurement system used was a infrared camera FLIR T620bx [194] with an infrared image resolution of 640×480 pixels. The spectral range is 7.5-14 μm and is applicable for a thermal range of -40 to +150°C by considering a sensitivity of 30 mK @+30°C. To measure the surface temperature of the experimental system the infrared camera was placed with a distance of 0.4 m away from the test section. The test section and perspex cavity of 50 mm by 50 mm by 10 mm whose wall thickness is 5 mm is shown in Fig. 7.2. This cavity was filled with a commercial mineral oil based magnetic fluid and subjected to thermal forcing by pumping hot water through a heating channel and cold water through a cooling channel respectively made of thin aluminium at two opposite side walls. The cooling channel was maintained by a constant temperature of $T_c = 20$°C by pumping water from a heat sink that was monitored by a PT100 temperature sensor. The heating channel was kept at temperature T_h via circulating water provided by a thermostating bath that

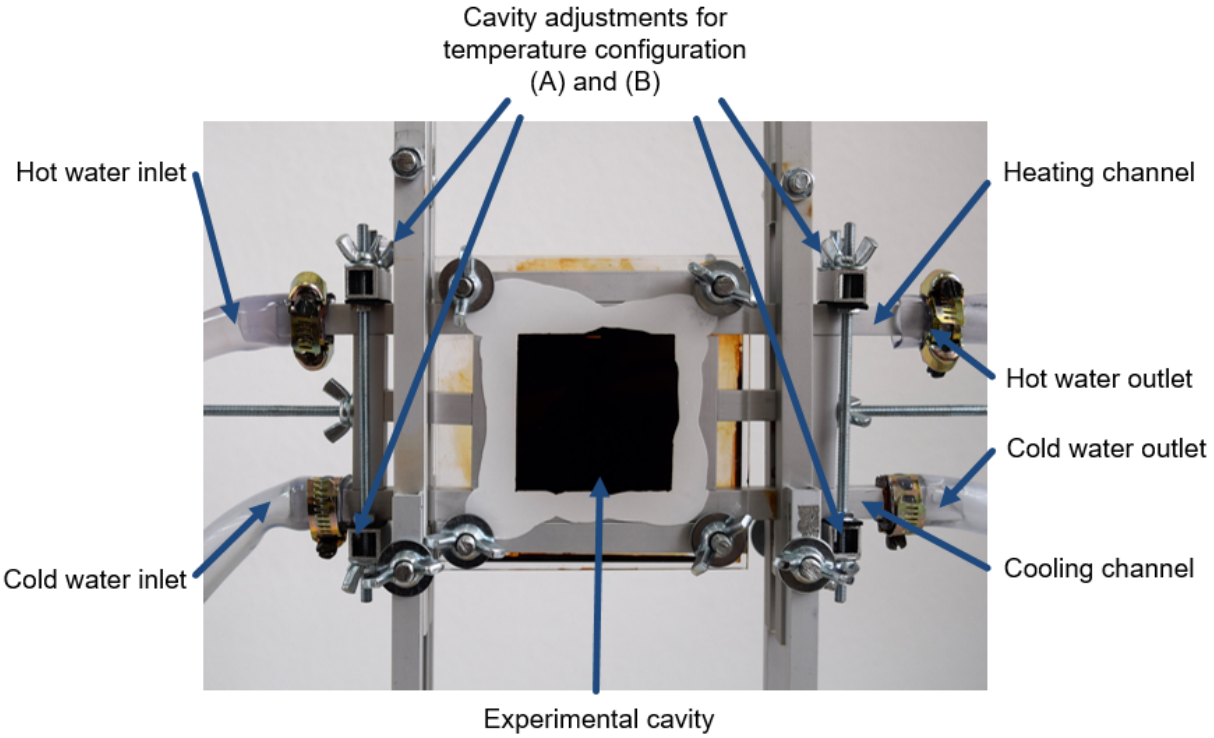

Figure 7.2: Experimental test section and perspex cavity filled with the magnetic fluid in configuration (A) without temperature sensors.

was controlled by a temperature control unit with an accuracy of 0.1 K. All remaining walls were insulated and considered to be adiabatic. The test section was designed such that two temperature and velocity boundary conditions could be investigated by rotating the system by 90°. Both cases (A) and (B) are presented in Fig. 7.1 (left). A permanent magnet with dimensions of 60 mm by 30 mm by 3 mm having its poles at the large 60 mm by 30 mm surfaces and a remanent flux density of $B_r = 1$ Tesla was used to provide an external magnetic field. To investigate the effect of external magnetic fields on a heated magnetic fluid the permanent magnet was placed respectively with a distance of 5 mm centred beneath (1), centred at the top (2) and centred at the left side (3) of the cavity. All positions of the permanent magnet are found in Fig. 7.1 (right).

7.2.2 Measuring technique and image processing

The experimental measurement technique of surface temperature fields was designed such that a set of temperature differences was completed each day by using a specific permanent magnet position shown in the right panel of Fig. 7.1. The measurement process consisted of a setup time of one hour each day. The first experiment used configuration (A) without a permanent magnet. The corresponding boundary conditions for temperature and

velocity are shown in the left panel of Fig 7.1. A temperature difference of $\Delta T = 10$ K was set between the top and bottom wall and maintained by heating the circulating water through the temperature control unit at the thermostating water bath. The evolving surface temperature field was observed via the live view of the infrared camera and used to determine if the fluid had clearly settled into a stable final state according to the applied temperature gradient. After the settling period, the surface temperature was recorded by an infrared image frame with the temperature scale superimposed by the camera. The conduction case configuration (A) was monitored for about one hour until the first frame was taken. Thereafter, the hot side was rapidly heated to the next temperature difference of $\Delta T = 20$ K which was recorded after a settling period of 30 min by an infrared image. Configuration (B) followed the day after by using the same procedure. The observed temperature field regarded to laminar natural convection and the established flow was induced by gravitational acceleration. The experiments with magnetic configurations (A1), (A2), (A3), (B1) and (B2) followed according the same procedure as the configurations without a magnet. At each day one magnetic configuration with the two temperature conditions was investigated, respectively.

While the infrared camera recorded the temperature of the outside of the perspex wall, the fluid's temperature was only reflected through conductive heat transfer across the perspex wall. The temperature of the fluids interior had to be estimated by using the in-siut temperature measurements from the thermocouple probes which were used to calibrate the surface infrared images. As the thermocouple probes were behind the perspex walls they provide two reliable calibration points as the signals need to go through the same wall. This provides a calibration to reconstruct the fluid temperature field. By using the infrared cameras software two measurement points were set manually to coincide with the in-situ temperature sensors. The recorded images generated by the infrared camera were extracted and post-processed to transfer the RGB values into a temperature matrix by using the infrared temperature scale added by the camera. This matrix was then adjusted to the temperature scale used by the temperature sensors. This method provided the correction of the radiation detected by the infrared cameras sensor and included the emissivity corrections as introduced in §5.3. To compare numerical and experimental results, the temperature matrix was expressed in non-dimensional form and plotted with a temperature color bar scaled to match the numerical results performed by the FEM-model.

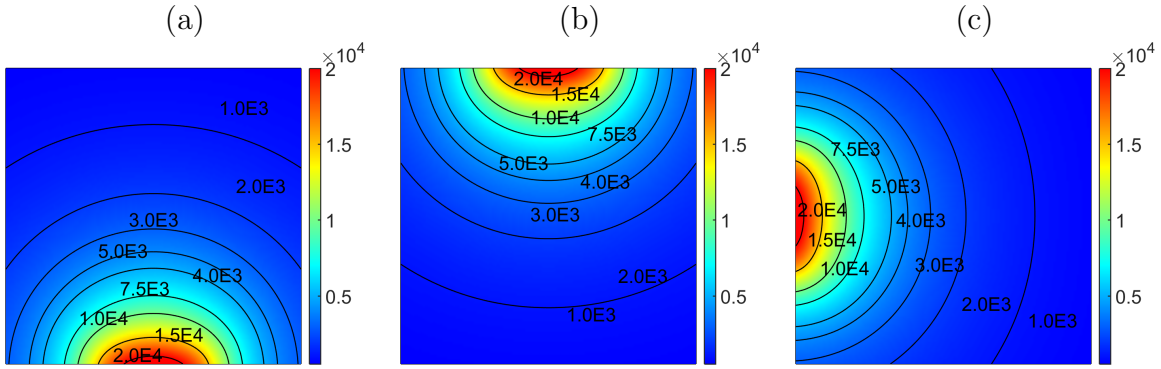

Figure 7.3: Contour plot of the magnetic field strength, H, in the x-z plane inside the convection cell for configuration (1) in (a), (2) in (b) and (3) in (c).

7.3 Computational methodology and numerical input

The numerical model was computed with the use of COMSOL Multiphysics [187] a commercially developed finite element solver. A tetrahedral mesh was used with 4,011,242 elements where most of them (3,437,223) were allocated to the fluid domain. Tests at a range of resolution suggested that the numerical model converged to a final reliable solution of at least 3 million tetrahedral elements. A parametric non-linear solver was used for stationary solutions and allowed to sweep initial parameters such as the temperature difference across the system.

7.3.1 Numerical methodology

To ensure that a realistic magnetic field corresponding to the conducted experiments was correctly computed, the field had to be solved in an extended domain. A cube with edge length of $3L$ was used where L is the physical cavity length and zero magnetic scalar potential was applied at its boundaries. The permanent magnet was placed in the centre of the cube and equipped with a remanent flux density of $\mathbf{B_r} = (0, 0, B_r)$ for study case (A1), (A2), (B1) and (B2) or $\mathbf{B_r} = (B_r, 0, 0)$ when configuration (A3) was used. The perspex cavity filled with the magnetic fluid was placed according to each specification outlined in Fig. 7.1 within the extended domain. The magneto-static Maxwell's equations presented in eq.(4.11), eq.(4.10) and eq.(7.1) were solved using a liner solver in all domains in a first study step. From this, a second study step used only the solution of the induction field, $\mathbf{B}$, to compute the resulting magnetic field, $\mathbf{H}$, within the fluid domain using eq.(7.2). Results of $\mathbf{H}$ are presented in Fig. 7.3 for all magnetic configurations. The magnetisation was then provided by the temperature of the magnetic fluid and the computed magnetic field, $\mathbf{H}$, and calculated via eq.(2.25) that provided the pyromagnetic coefficient, K_p,

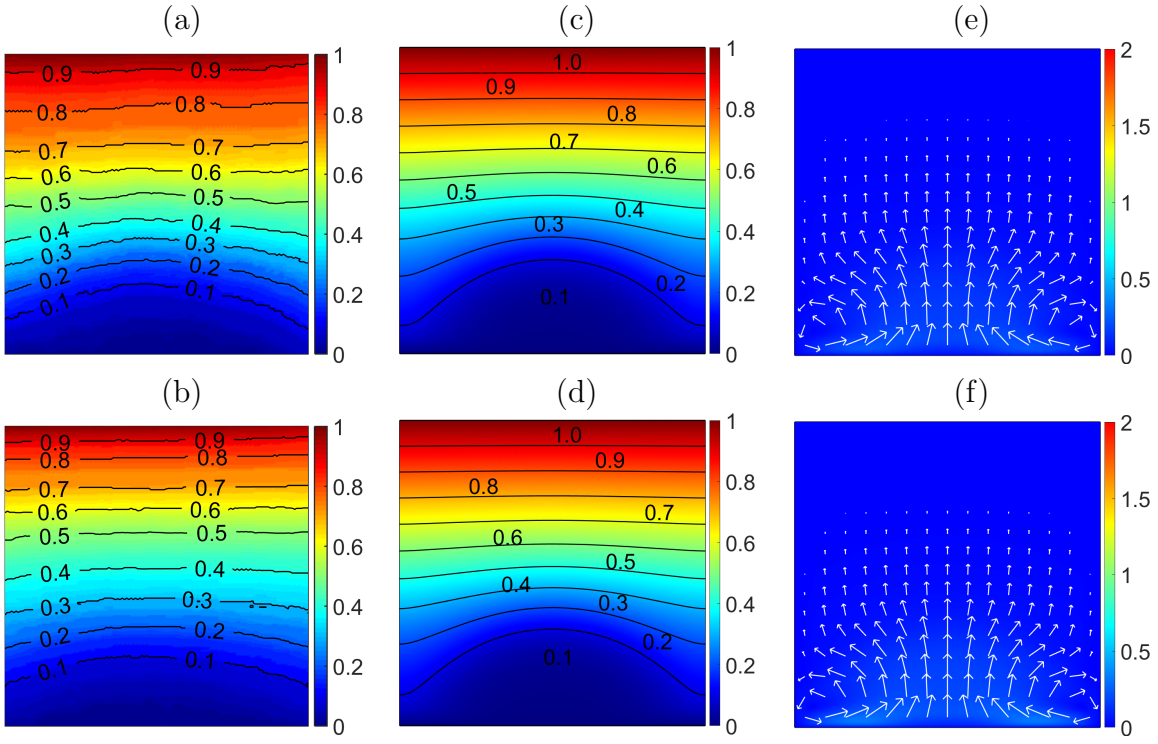

Figure 7.4: Non-dimensional experimental temperature fields in (a), (b) , non-dimensional computed temperature (c), (d) and velocity fields (e), (f) for $\Delta T = 10$ K, $\mathrm{Ra}^* = 3.85 \times 10^6$ in the top row and $\Delta T = 20$ K, $\mathrm{Ra}^* = 7.66 \times 10^6$ in the bottom row using configuration (A1).

eq.(4.68) to calculate the Kelvin body force. Hence, the continuity, momentum and heat eq.(7.3-7.7) were computed simultaneously using the buoyancy and the Kelvin body force as the active volume forces.

7.4 Results

This section presents the experimentally observed temperature recordings alongside the numerical temperature and velocity fields of the computational model in §7.4.1-§7.4.5 for configuration (A1), (A2), (A3), (B1) and (B2) respectively. This is followed by an analysis of the heat transfer with the use of the computational model in §7.5 and a comparison of experimental and computational results in §7.6.

7.4.1 Thermomagnetic convection with configuration A1

By placing the magnet below the cavity in configuration (A1) the magnetic force expressed through the Kelvin body force distorts the horizontal isotherms in the bottom of the cavity. As the Kelvin body force is strong near the magnet cooler magnetic fluid is attracted due to

its higher magnetisation closer to higher magnetic field intensity. This forms a dome shape of cold magnetic fluid in the bottom of the fluid domain represented in the experimental temperature profile in Fig. 7.4(a). By an increase in temperature difference across the system the dome expands throughout the cavity as seen in Fig. 7.4(b). The phenomena may be understood by comparing the experimental results with the numerical computed temperature profiles shown in Fig. 7.4(c) and (d) which reflect the experimental findings. However, the dome of cold magnetic fluid in the numerical solutions expands slower than the experimental observed temperature profile. Regardless of the difference the effect of the formation of cold magnetic fluid in the bottom of the cavity can be interpreted with the corresponding velocity profiles in Fig. 7.4 (e) and (f). Here, the higher magnetised cold magnetic fluid moves from each side at the bottom of the cavity horizontally towards the middle of the bottom wall where it converges and rise in the centre of the fluid domain. When the magnetic force decreases further away from the magnet, the stratification due to gravity in the top of the fluid domain becomes stable. There, no convective heat transfer is observed in the numerical and experimental model and only conduction is present and is reflected in straight isotherms at the top part of the cavity.

The temperature plots in Fig. 7.5 are used to identify the vertical temperature distribution within the fluid domain through the centre of the cavity. Here, each curve correspondents to the panels (a) to (d) of Fig. 7.4, respectively and present a good agreement between experimental and computational results. The curves show a relative small increase of the temperature within the cavity to about 20% compared to the conduc-

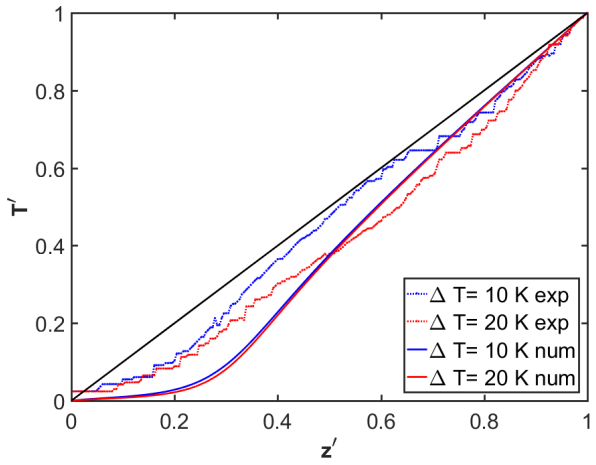

Figure 7.5: Non-dimensional experimental and simulated temperature profiles for the vertical cross-section through the centre of the cavity using magnetic configuration (A1). The solid black diagonal line is the conduction-only solution.

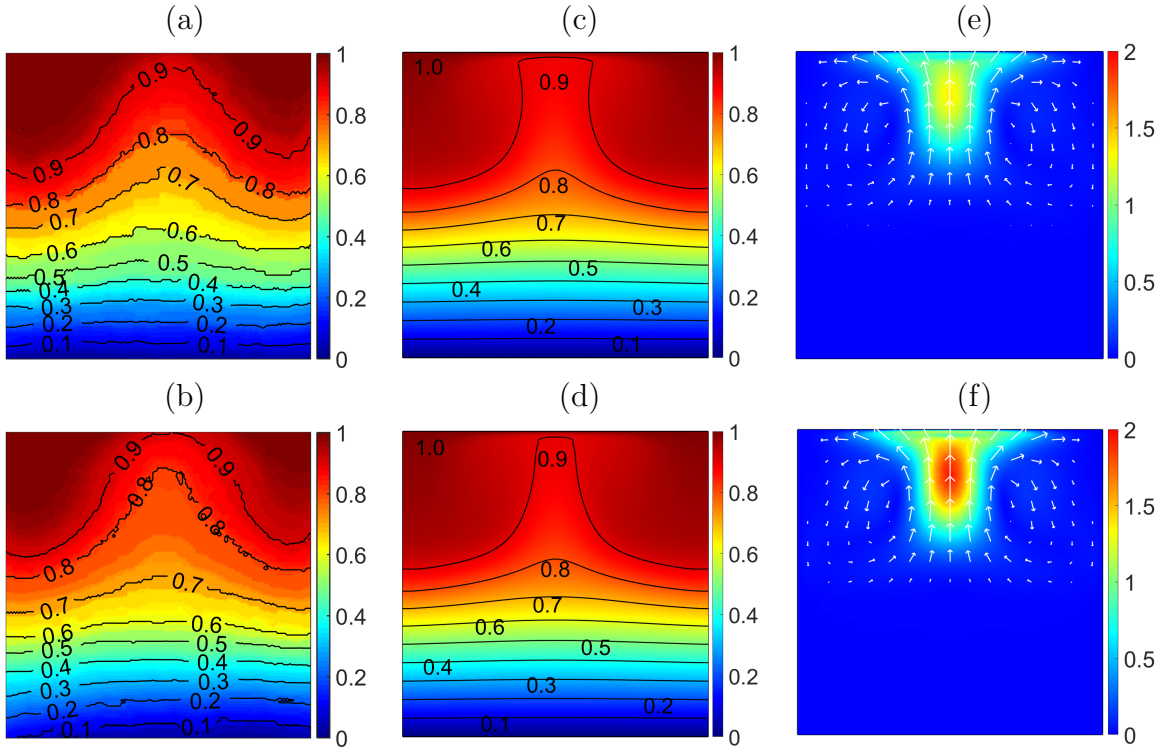

Figure 7.6: Non-dimensional experimental temperature fields in (a), (b) , non-dimensional computed temperature (c), (d) and velocity fields (e), (f) for $\Delta T = 10$ K, $\mathrm{Ra}^* = 1.93 \times 10^7$ in the top row and $\Delta T = 20$ K, $\mathrm{Ra}^* = 3.71 \times 10^7$ in the bottom row using configuration (A2).

tion case represented by a solid black diagonal line. The temperature gradient for both computational solutions in this region is about $\mathrm{d}T'/\mathrm{d}z' = 0.01$ and for the experimental results a little higher at $\mathrm{d}T'/\mathrm{d}z' = 0.05$ indicating heat transfer by convection. Above that region the temperature gradient increases gradually until it reaches a fairly constant value of $\mathrm{d}T'/\mathrm{d}z' = 1.5$ at $z' \approx 0.35$ for computational results. The experimental temperature curves for both temperature differences follow that increase to about $z' \approx 0.3$ but are smaller than the computed values. The upper 60% of the cavity with a fairly constant temperature gradient indicates heat transfer by conduction where simulations and experiments are closely aligned and present excellent agreement.

7.4.2 Thermomagnetic convection with configuration A2

Placing the magnet at the top of the heated system the Kelvin body force induces thermomagnetic convection within the cavity by distorting the isotherms resulting in a change in heat transfer.

The observed experimental temperature fields are presented in Fig. 7.6 for two different

temperature differences alongside the corresponding computed temperature fields and indicate convective heat transfer. The weak convective flow and its pattern is shown in Fig. 7.6(e) and (f) by numerical simulation where the fluid moves upwards against gravity in the centre of the cavity towards hight magnetic field intensity. The cold magnetic fluid with a higher magnetisation is therefore forced upwards towards the magnet to displace hotter fluid at the top of the cavity. The observed thermomagnetic convection gets stronger in the top of the cavity when the temperature difference across the system increases whereas the bottom of the cavity is less affected by the magnetic force.

The difference in convective flow for the two temperature differences investigated is identified by the vertical temperature profiles through the centre of the cavity shown in Fig 7.7. Here, each curve corresponds to the panels (a) to (d) of Fig. 7.6, respectively. All four plots show a relatively constant temperature increase from the bottom of the cavity to about 30 to 40% of the depth. There, the temperature gradient of both computational simulation is $\mathrm{d}T'/\mathrm{d}z' = 1.761 \pm 0.003$. The experimental temperature gradient in this region is a little smaller at $\Delta T = 10$ K: $\mathrm{d}T'/\mathrm{d}z' = 1.44 \pm 0.01$ and at $\Delta T = 20$ K: $\mathrm{d}T'/\mathrm{d}z' = 1.55 \pm 0.01$. Above the linear increase in temperate the computational temperature gradient decrease gradually and reaches an isothermal region between $z' \approx 0.75$ and 0.98. This correspondents to the convective heat transfer observed in Fig. 7.6. Further above the mixed region, a thermal boundary layer is visible having a temperature gradient at the top wall of $\mathrm{d}T'/\mathrm{d}z' = 7.69$ at $\Delta T = 10$ K and $\mathrm{d}T'/\mathrm{d}z' = 7.95$ at $\Delta T = 20$ K, respectively. The experimental thermography fields for both temperature differences fol-

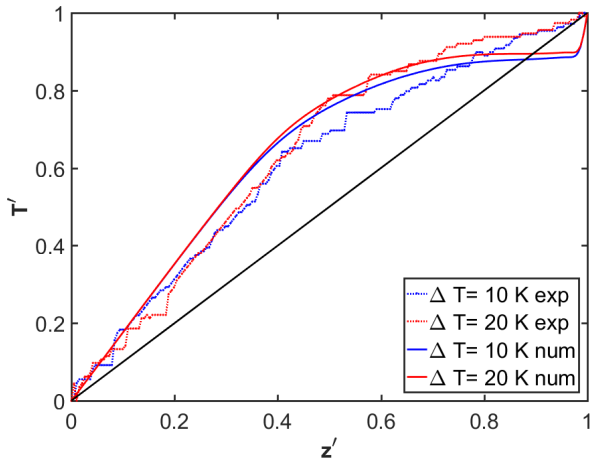

Figure 7.7: Non-dimensional experimental and simulated temperature profiles for the vertical cross-section through the centre of the cavity using magnetic configuration (A2). The solid black diagonal line is the conduction-only solution.

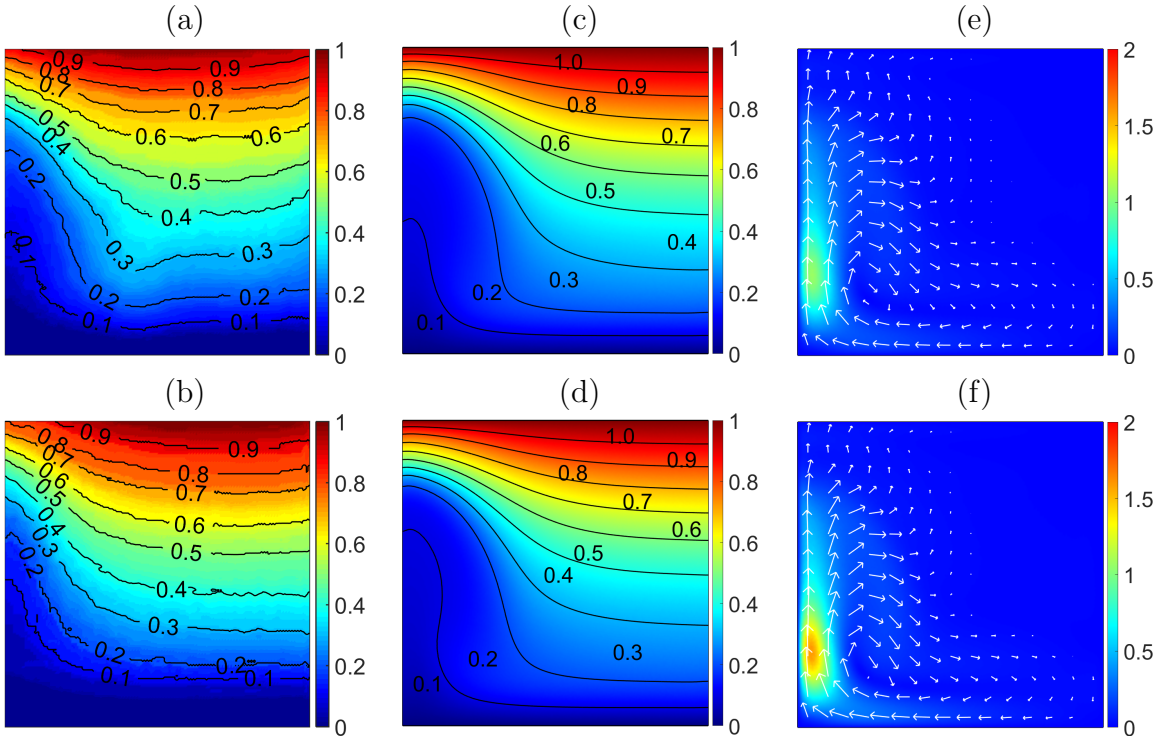

Figure 7.8: Non-dimensional experimental temperature fields in (a), (b) , non-dimensional computed temperature (c), (d) and velocity fields (e), (f) for $\Delta T = 10$ K, $\mathrm{Ra}^* = 4.33 \times 10^6$ in the top row and $\Delta T = 20$ K, $\mathrm{Ra}^* = 8.22 \times 10^6$ in the bottom row using configuration (A3).

low the numerical computed results closely. However, the boundary layer is not resolved. In general the results of the experiments in the convection region remain below the computed results but even then, a reduction in the temperature gradient is observed that indicates the presence of convective heat transfer within the cavity. The transition region of the observed conduction layer to the convection region is in the experiment at around $z' = 0.43$ and 0.5, for $\Delta T = 10$ K and 20 K respectively, whereas the computational transition region is observed at $z' = 0.29$ and 0.32.

7.4.3 Thermomagnetic convection with configuration A3

In the third configuration (A3) where the magnet is at the left side of the cavity a horizontal magnetic field is generated. Results suggest a similar convective behaviour as the previous described thermoconvective cases above and are presented in Fig. 7.8. The thermomagnetically induced flow in this configuration pulls the isotherms up at the left cavity wall which is closer to the magnet as seen in the experimental temperature profile in Fig. 7.8(a) and (b) alongside the corresponding computational results in Fig. 7.8(c)

and (d). As the magnetic field is now perpendicular to buoyancy the resulting Kelvin body force induces a weak flow of colder more strongly magnetised magnetic fluid from the bottom of the cavity towards the left side wall. The fluid moves then upwards at the side wall towards the magnet and creates a thermomagnetic convective cell. In the right part of the fluid domain the thermal stratification under gravity becomes visible as the Kelvin body force becomes weaker when the magnetic field intensity decreases according to the distance of the permanent magnet. The fluid in the right part of the domain is therefore little affected and moves very slowly as seen in Fig. 7.8(e). When the temperature difference of the system is increased the overall convective flow increases as presented in Fig. 7.8(f). This indicates an increase of convective heat transfer within the cavity.

The difference of the experimental and computed temperature profiles are identified by the vertical temperature plot in Fig. 7.9(a) and horizontal temperature plot in Fig. 7.9(b) through the centre of the fluid domain. A good agreement between the experiments and computational simulation is observed for the vertical temperature plot for all temperature configurations. Comparing the solution with configuration (A1) and (A2) the temperature profile is much closer to the diagonal conduction line that represents the conductive only case. The smallest vertical temperature gradient is found in a region between $z' = 0.2$ and the mid-hight of the cavity and indicates heat transfer by convection. Above this region the temperature plot becomes gradually more linear and reaches a constant temperature gradient of $\mathrm{d}T'/\mathrm{d}z' = 1.30$, at $\Delta T = 10$ K, and $\mathrm{d}T'/\mathrm{d}z' = 1.37$ at $\Delta T = 20$ K. Above this at the upper 20% of the cavity a very small convective region is observed and confirmed

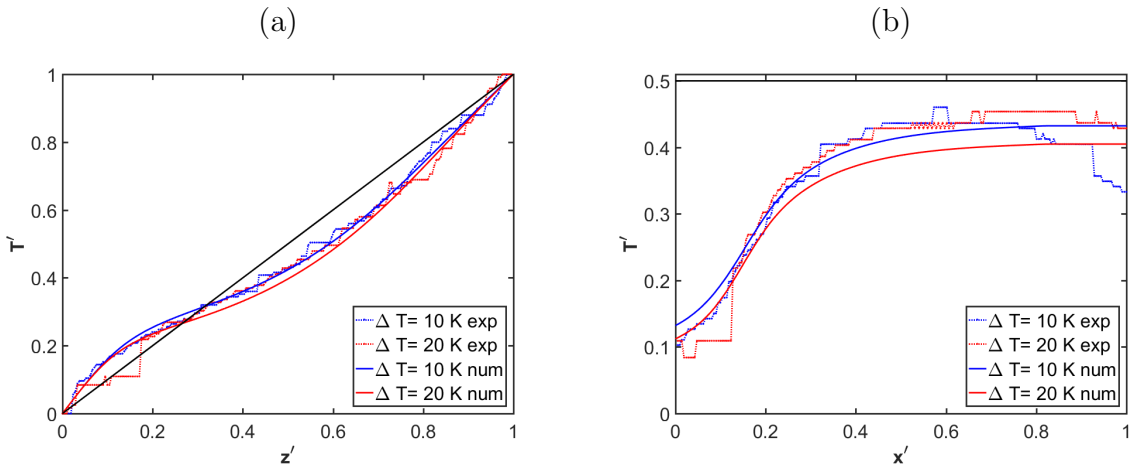

Figure 7.9: Non-dimensional experimental and simulated temperature profiles for the vertical cross-section in (a) and horizontal in (b) through the centre of the tank using magnetic configuration (A3). The solid black diagonal line is the conduction-only solution.

by the velocity field in Fig. 7.8(e) and (f). For higher temperature differences such as $\Delta T = 20$ K the convective region extends further down indicating an increase in heat transfer.

The horizontal temperature plot at mid-height of the cavity presents low temperatures close to the left side wall within about $x' = 0.1$ and is increased rapidly to a moderate constant level at about $x' = 0.4$. While the temperature plots agree well with each other, the experimental observations do not reflect the decrease seen in the computational simulation when the temperature is increased from $\Delta T = 10$ K to 20 K. However, the computed temperature plots at $\Delta T = 20$ K compared with $\Delta T = 10$ K indicate convective cooling near the permanent magnet. This results in a overall reduction of temperature across the cavity. While the computational simulations reach the highest temperature at the right insulated side wall of the cavity, the experiments present a maxima not at the upper right corner but along the top boundaries away from the right boundary. This is followed by a drop closer to the right side wall which is more moderate at higher temperature differences.

7.4.4 Thermomagnetic convection with configuration B1

When the cavity is heated from the side walls as is done in configuration (B1) regular natural convection is present and is influenced by the Kelvin body force when the permanent magnet is placed below the cavity. As can be seen in Fig. 7.10(a) the magnetic fluid is heated at the left and cooled at the right side wall whereas all remaining walls are kept adiabatic. The experimental temperature field presents the temperature boundary layer at the cooled and heated side walls which start decreasing when the temperature is increased as seen in Fig. 7.10(b). Within the fluid interior the isotherms are more stably stratified. However, at the bottom a dome pattern of cold magnetic fluid is observed. There the cold magnetic fluid is attracted towards the highest magnetic field intensity that is closest to the magnet. Consistent with the experimental findings are the numerically computed temperature profiles shown in Fig. 7.10(c) and (d). The corresponding computed velocity profiles seen in Fig. 7.10(e) and (f) present a domain-filling convection cell where the magnetic fluid moves from the heated side wall towards the top of the cavity and descends near the cold side wall. There, the fluid is moved to higher magnetic field intensity to form a dome flow pattern that is as high as the half cavity. This distorts the isotherms at the bottom in a circular shape surrounding the highest magnetic field region. As the Kelvin body force is weaker at the top of the cavity the isotherms are more stratified there and the flow is more dominated by natural convection.

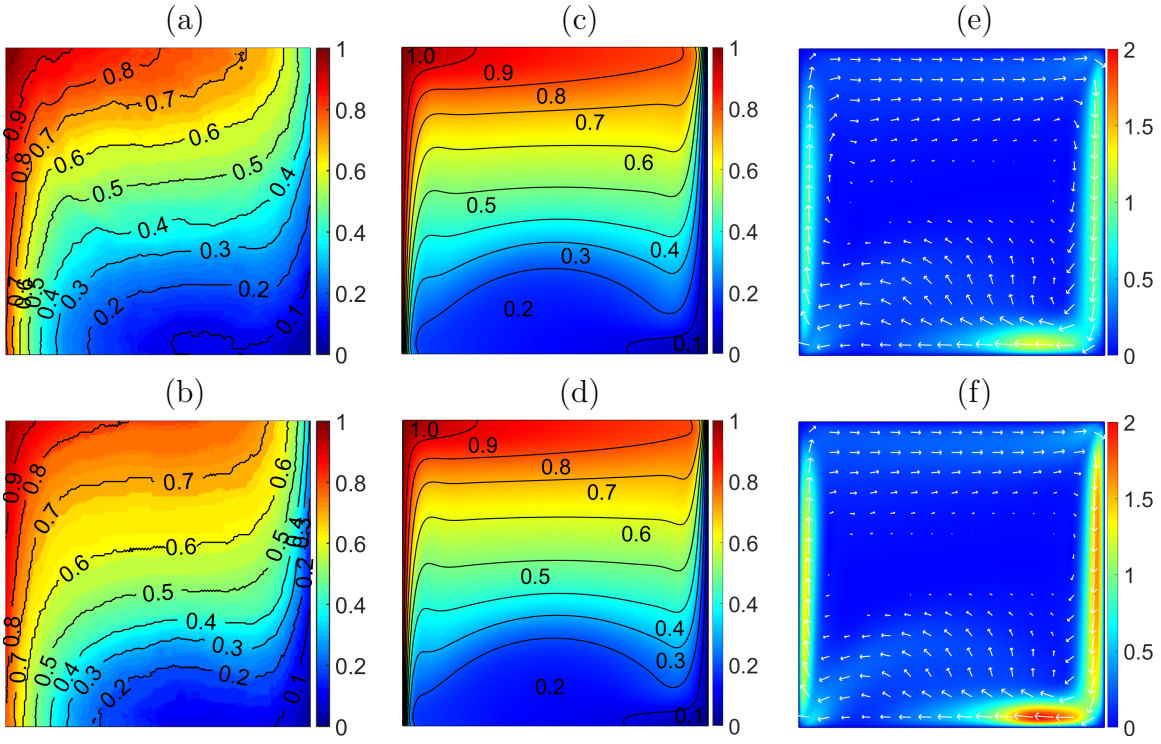

Figure 7.10: Non-dimensional experimental temperature fields in (a), (b) , non-dimensional computed temperature (c), (d) and velocity fields (e), (f) for $\Delta T = 10$ K, $\mathrm{Ra}^* = 6.54 \times 10^6$ in the top row and $\Delta T = 20$ K, $\mathrm{Ra}^* = 1.27 \times 10^7$ in the bottom row using configuration (B1).

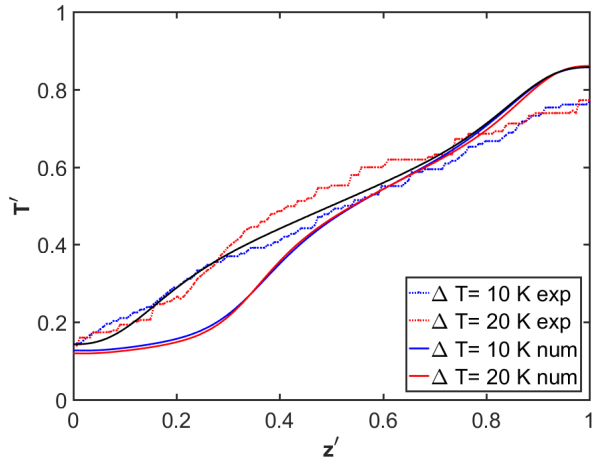

Figure 7.11: Non-dimensional experimental and simulated temperature profiles for the vertical cross-section through the centre of the cavity using magnetic configuration (B1). The solid black line is the natural convection solution for $\Delta T = 10$ K.

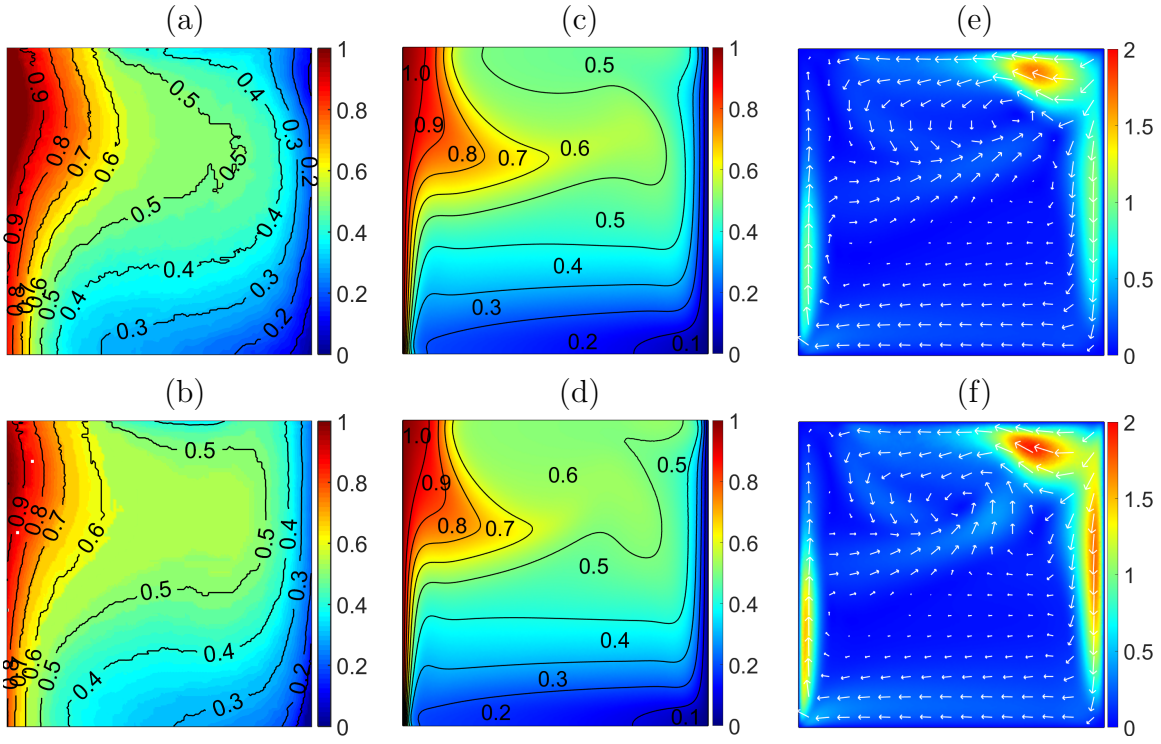

Figure 7.12: Non-dimensional experimental temperature fields in (a), (b), non-dimensional computed temperature (c), (d) and velocity fields (e), (f) for $\Delta T = 10$ K, in the top row and in the bottom row using configuration (B2).

The differences in experimental and computed temperature profiles are identified with the same principle as before through the centre of the cavity and results shown in Fig. 7.10. Here, the experiments and computed results do not agree well with each other quantitatively. However, the qualitative view reflects the same trend and shape of the curves observed in the numerical results. The computational results present an isothermal region in the lower 20% of the cavity where the temperature of the fluid is low and indicates convective heat transfer. Above that region the temperature gradient increase and reaches a maximum of $\mathrm{d}T'/\mathrm{d}z' = 1.4$ at $z' = 0.40$. Here, the temperature gradients starts decreasing to a fairly constant value to about $\mathrm{d}T'/\mathrm{d}z' = 0.6$ to align closely with the natural convection solution (B0) presented as a solid black line. At $z' = 0.75$ the temperature gradient increases moderate to $\mathrm{d}T'/\mathrm{d}z' = 0.8$ in the upper 80% of the cavity and starts decreasing into a convective boundary layer at about $z' = 0.95$. In general, the experimental temperature curves are more aligned with the natural convection case. However, the moderate trend of the temperature gradients follows the computational solutions.

7.4.5 Thermomagnetic convection with configuration B2

The last configuration (B2) used the permanent magnet at the top position of the perspex cavity and was used to explore the transition region discussed in §6.3.3 by using a horizontal magnetic field gradient with spatial variation in intensity generated by the permanent magnet and is presented in Fig. 7.3(b). Here, the magnetic fluid is magnetised resulting in the additional Kelvin body force that significantly affects the temperature distribution within the cavity. The experimental temperature fields in Fig. 7.12(a) and (b) show this in the top of the cavity. A tongue of cold fluid is moved upwards against buoyancy from the left cooled side wall towards the magnet displacing the hot fluid below it. The numerical temperature profiles in Fig. 7.12(c) and (d) show a good agreement with the experimental observed temperature fields. The velocity fields in Fig. 7.12(e) and (f) present the change in convective structure that are indicative for the change in the temperature profile. There, a second, counter-circulating cell has established in the top part of the cavity that is closest to the magnet and pushed the natural convection cell dominated by buoyancy downwards.

To compare the experimental and computational temperature profiles for the last configuration (B2) the temperature distribution trough the centre of the cavity is investigated. Here, the computational results show a convective boundary layer to a depth of 5% followed by an increase in the temperature gradient that is fairly constant in the region of $z' = 0.3$ to $z' = 0.5$ of about $\mathrm{d}T'/\mathrm{d}z' = 0.4$ following the natural convection line plotted in black. The temperature gradient then peaks at $z' = 0.6$ and is followed

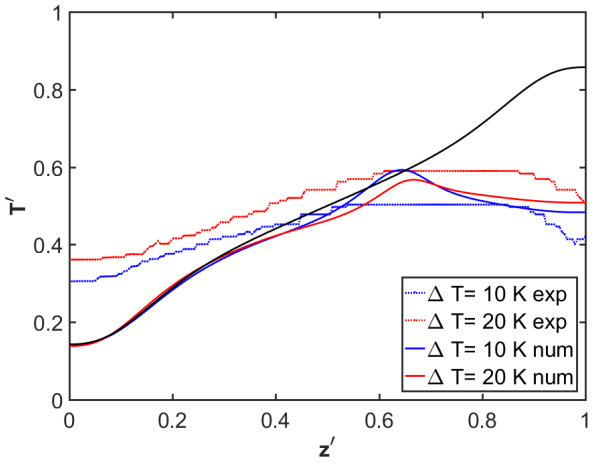

Figure 7.13: Non-dimensional experimental and simulated temperature profiles for the vertical cross-section through the centre of the cavity using magnetic configuration (B2). The solid black line is the natural convection solution for $\Delta T = 10$ K.

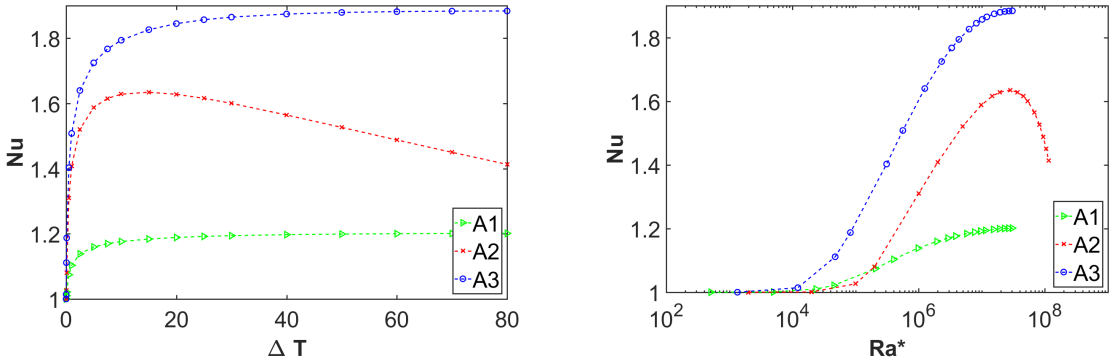

(a) (b)

Figure 7.14: The Nusselt number, Nu, plotted versus the temperature difference in (a) and the modified Rayleigh, Ra*, in (b) for configuration (A).

by a decrease to $\Delta T = 10$ K: $\mathrm{d}T'/\mathrm{d}z' = -0.75$, and at $\Delta T = 20$ K: $\mathrm{d}T'/\mathrm{d}z' = 0.44$. At $z' = 0.8$ the temperature gradient recovers to a relative constant increase. The experimental temperature profile correspond to the computed ones but are slightly higher. The experimental temperature gradient is as well as the computational results fairly constant at $\mathrm{d}T'/\mathrm{d}z' = 0.5$ to about 55% of the cavity hight. Then, the gradient decreases to zero at $z' = 0.54 : \Delta T = 10$ K and $z' = 0.6 : \Delta T = 20$ K and remains presenting an isothermal region until it starts decreasing moderately at $z' = 0.8$.

7.5 Heat transfer by thermomagnetic convection

The heat transfer across the experimental cavity is characterised by the dimensionless Nusselt number, Nu, presented in eq.(4.64) and investigated by using the computational model. The Nusselt number for the first configuration (A1-A3) is plotted versus the tem-

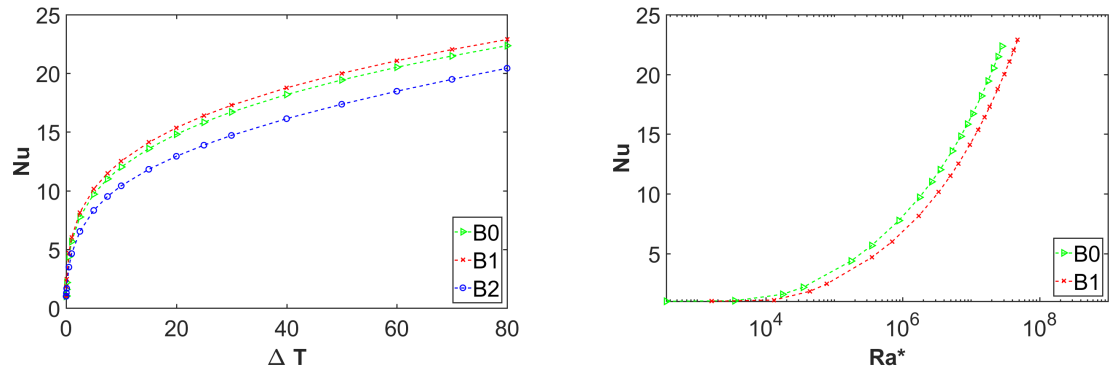

(a) (b)

Figure 7.15: The Nusselt number, Nu, plotted versus the temperature difference in (a) and the modified Rayleigh, Ra*, in (b) for configuration (B).

perature in Fig. 7.14(a). Here, the heat transfer increases by thermomagnetic convection and approaches a maximum for each configuration that uses the temperature boundary condition (A). When the maximum in Nusselt number in configuration (A1) and (A3) is reached Nu remains constant if the temperature difference is increased further. This indicates that thermomagnetic convection can increase heat transfer to a certain threshold depending on the applied difference in the system temperature. However, this is different for configuration (A2) where the Nusselt number peaks at 1.63 and starts decreasing constantly when temperature is increased. Fig. 7.14(b) reflects the results where Nu is plotted versus the modified Rayleigh number, Ra^*. Here, the peak in Nu is at $\mathrm{Ra}^* = 3.71 \times 10^7$ for configuration (A2) and starts dropping with increasing Ra^*. The configuration (A1) and (A3) correspond to those observed in Fig. 7.14(a) and reflect a threshold in Nu whereas the modified Rayleigh number increases with increasing temperature difference.

The heat transfer characteristics for temperature configuration (B) are presented in Fig. 7.15 where configuration (B0) is the natural convection case and (B1) and (B2) the combined natural and thermomagnetic convection configurations. As seen in Fig. 7.15(a) all three computed configuration increase heat transfer significantly when temperature is increased. However, they differ between the magnetic configurations. While configuration (B1) enhances heat transfer, (B2) reduces natural convection as the body forces oppose each other. An indication of strength of combined convection is given by the modified Rayleigh number, Ra^*, in Fig. 7.15(b) for configuration (B1). The natural convection case (B0) is plotted as an indication of the increase in combined convective heat transfer. A modified Rayleigh number for configuration (B2) is not calculated and will be discussed in §7.6.

To establish a constant temperature difference within the experiments that corresponds to the computational model a lumped capacity analysis is conducted for the experimental test section. For this purpose the Nusselt number, Nu, is extracted from the numerical simulations to calculated the expected convective heat transfer coefficient, h, at the solid-fluid interface of the heating and cooling channel by using eq.(4.62). As the computational simulation provided stationary solutions for all configurations the heat flux through the non-adiabatic boundaries must be constant for each configuration over time. This is confirmed by the experimental infrared thermography as temperature field did not vary over time after he settling period. Thus, it follows that the heat flux into the system must equal the heat flux out of the system. Following this relationship gives the same Biot number, Bi, for the solid-fluid interface at the heating and cooling channel. To provide a constant temperature at the non-adiabatic boundaries the lumped capacity analysis is conducted that assumes a uniform spatial temperature distribution within the

Table 7.1: The Nusselt number, Nu, convective heat transfer coefficient, h and Biot number, Bi, at the solid-fluid interface of the experimental non-adiabatic boundaries.

	dT=10K			dT=20K		
	Nu	h	Bi $\times 10^{-4}$	Nu	h	Bi $\times 10^{-4}$
A1	1.18	3.03	7.38	1.19	3.06	7.46
A2	1.63	4.19	10.22	1.63	4.19	10.22
A3	1.79	4.62	11.26	1.84	4.75	11.58
B	12.02	30.93	75.43	14.81	38.10	92.94
B1	12.52	32.20	78.59	15.36	39.53	96.40
B2	10.42	26.80	65.37	12.93	33.27	81.16

aluminium. This implicit the assumption of an absent temperature gradient within the solid that can be assumed when the Biot number is below 1. Thus, Bi is calculated using eq.(4.53) where h is the convective transfer coefficient and k_s the thermal conductivity of the heating and cooling channel both made of aluminium. The Nusselt number, Nu, the convective transfer coefficient, h and the Biot number, Bi, are presented for each configuration in Tab 7.5. Results of the computational model indicate that the Bi$>>$ 1 following that the temperature at the non-adiabatic solid-fluid interface can be assumed the same as in the heating and cooling channel respectively. This was also confirmed by each infrared image frames where no temperature gradient was observed within the 5 mm thick aluminium channel.

7.6 Discussion

This section gives a critical analysis of the experimental thermography observations and the corresponding computational results that lead to identify the features of thermomagnetic convection in the presence of gravity and the underlying physical process.

Reviewing the main differences between the experimental and computational results as highlighted the most dominate observed feature are the rising isotherms at the side walls for configurations (A1-A3), the differences in the spreading of the isotherms at the bottom and top wall for configurations (B1) and (B2) and the less sharp temperature gradients closer to the magnet. These differences refer to the perfectly insulated side walls used in the computational model resulting in straight isotherms whilst the experimental apparatus are imperfectly insulated leading to heat loss through the side walls, especially from the heated magnetic fluid. The reduction of the temperature gradient near the permanent magnet could be a consequence of the imaging technique or the magnet itself. While the computational model considered a uniform magnetisation across the pole surfaces and

sharp edges the physical magnet has slight imperfection such as a non-uniform surface magnetisation or rounded edges. This may lead to a reduction in the magnetic field gradient near the edges of the magnet. The imaging technique of infrared thermography used to record the temperature fields at the perspex side wall of the cavity leads to a spatial resolution which coincide with the thickness of the perspex wall. Therefore, the temperature boundary layer reported in Fig. 7.7 having a thickness of 2% of the cavity depth is not be expected to be resolved by the experimental set-up.

In the light of this, the computational simulations for (A1) in panels (c) and (d) of Fig. 7.4 show good quantitative and qualitative agreement by comparing with their corresponding experimental observations in panels (a) and (b). Here, the isotherm spacing of the experiments at the bottom of the cavity closely reflect the computational simulation. The quantitative comparison of the computational temperature distribution in Fig. 7.5 through the centre of the cavity follows the trend of the experiments and report good agreement. Furthermore, the results of configuration (A2) and (A3) report a remarkable quantitative and qualitative agreement of experimental and computational simulations. In (A2) the location of the change of horizontal isotherms to the isotherms shifted upwards in the centre of the cavity below the permanent magnet closely mimic the observations. The spacing between the isotherms are in addition a good indication of a remarkable agreement and show the shift of the transition from the conductive layer to the upper convective heat transfer. The results are well captured by the computational model as well as experiments and shown in Fig. 7.7. A comparison of configuration (A2) with the computational results obtained by Chang et al. [148] shows good agreement and is used as a validation of the computational model. The velocity fields presented in Fig. 7.7(e) and (f) may be used to interpret the computational and experimental observed temperature fields as the result of thermomagnetic convection. As the magnetic field gradient in configuration (A2) creates through the Kelvin body force a higher attraction of cold magnetic fluid below the warmer fluid towards the permanent magnet, two convection cells are established in the centre upper layer of the cavity. Here, warm magnetic fluid flows outwards and downwards at the side of the central region to be displayed by cooler fluid. The heat transfer is then organised by a thermomagnetically forced upper layer where the Kelvin body force is dominat and a stable lower layer where gravity overcomes the magnetic forces resulting in a stably stratified conduction layer.

All these findings can be used to analyse configuration (A3). Here, the Kelvin body force is perpendicular to gravity and is strong enough to induce thermomagnetic convection in a single convection cell. The cold magnetic fluid from the bottom of the cavity is attracted closer to the permanent magnet resulting in a strong convection near the

magnet. At the upper and lower boundaries of the cavity that are closer to the magnet the flow is weak whereas further away a stagnant region of cold and hot magnetic fluid is observed. The established convection cell may be understood by the perpendicular orientation of both acting body forces. As gravity points downwards it does not impede horizontal fluid flow such as the horizontal acting Kelvin body force does. Here, the fluid responds towards the magnet from the lower region of the cavity and injects it towards the upper region forming a convection cell that satisfies continuity.

The experiments and computational simulation for (B1) show good qualitative agreement whereas the quantitative comparison is acceptable by considering the limitations of the experimental apparatus. The imperfection of insulation of the experimental cavity is clearly seen when comparing the temperature profiles in panel (a) to (d) in Fig. 7.10. While the isotherms in the experiment at the upper and lower side walls are shifted towards the centre of the cavity, the isotherms in the computational model are closely spaced. This indicates heat loss through the top and bottom wall of the experimental set-up such that the quantitative comparison in Fig. 7.13 does not agree well with the computational results in the lower and upper 25% of the cavity. However, the computational temperature profiles mimic the experimental observations such that the computed velocity profiles in panel (e) and (d) of Fig. 7.10 are used to understand the resulting temperature distribution within the cavity. Here, the permanent magnet that is placed below at mid-height of the cavity attracts colder fluid closer towards the magnet forming a circular flow pattern at the bottom of the cavity, then starts rising at the left heated side wall where the fluid heats up and descends near the cold wall forming a convective cell. As both body forces contribute towards the direction of the flow heat transfer increases as it is seen in Fig. 7.15 compared to the natural convection case where the Kelvin body force is absent.

Configuration (B2) presents according to the experimental limitation good qualitative and adequate quantitative agreement. This relates to the arguments of the imperfect insulated top and bottom wall mentioned above in detail for configuration (B1) and can be directly transferred. However, the effect at the upper layer of the cavity is less strong and is a result of the cold fluid that is attracted towards the magnet at the top of the cavity reducing heat losses through the system. This is reflected in Fig. 7.13 by a closer alignment of experimental and computational results in the upper 25% of the cavity. The difference in lower the 25% of the cavity remains and corresponds to the observed heat losses for configuration (B1). In spite of the limitation, the experimental thermography images mirror the computational temperature profiles and give evidence of a transition region between natural and thermomagnetic convection that is found for uniform magnetic

field gradients in §6.3.3. When the magnet is placed at the top of the cavity the convective pattern of natural convection is influenced by the Kelvin body force and a second counter-circulating convection cell is formed in the upper part of the cavity as seen in panel (e) and (d) of Fig. 7.12. Here, the Kelvin body force overcomes buoyancy and attracts cold fluid from the cooled right side wall towards the magnet pushing the original natural convection cell downwards. The corresponding temperature profiles in Fig. 7.12 (a) to (d) show that there is now warm fluid extending from the heated left wall between the two convection cells. This demonstrates the presence of a transition area within the cavity such that the top part of the cavity is dominated by thermomagnetic convection while the bottom of the cavity is still dominated by natural convection.

Using a single non-dimensional number to characterise the driving force of combined convection is possible for configuration (A1-B1) by using the proposed non-dimensional modified Rayleigh number but within certain limitations. First, if convection is induced only by one body force as is the case in (A1-A3) or second, both body forces contribute to each other forming a single convection cell as is the case in (B1). Here, a net balance of both body forces is developed by taking their spatial orientation into account and is indicative for the observed heat transfer. In the event when the Kelvin body force is opposite to gravity a transition region is found and the system is partly dominated by one of each acting body forces and a modified Rayleigh number cannot be developed. This refers to the individual contribution of each convection cell towards heat transfer and a net balance of the driving force for the complete system is not possible to distinguish. A special case occurs when both body forces are present but only one dominates the complete system and a single convection cell is observed as is the case in Fig. 6.4(a-c) by a gravity dominated cell and (m-o) by a Kelvin body force dominated cell.

As the flow and temperature fields are discussed on the basis of the acting body forces it is useful to quantify a force ratio which is introduced in eq.(6.6) for all configurations and plotted in Fig. 7.16. The Rayleigh and magnetic Rayleigh number are calculated with eq.(4.65) and eq.(4.70) respectively using the local computed results of equations (7.3-7.7). The top row in Fig. 7.16 presents the force ratio, r for configuration (A1). Here, the distribution of r in panel (a) for $\Delta T = 10$ K shows that the Kelvin body force is dominat in the bottom of the cavity whereas buoyancy dominates the top. When the temperature difference across the system increases further, the $r = 0$ contour line shifts marginal downwards as is seen in panel (b) and (c). To give a quantitative indication of this shift the non-dimensional distance of $r = 0$ in the centreline of the cavity is used and shown in Tab. 7.2. Here, the shift is 0.79% when ΔT is increased from 10 K to 80 K. The effect relates to the temperature dependent pyromagnetic coefficient, K. In particular,

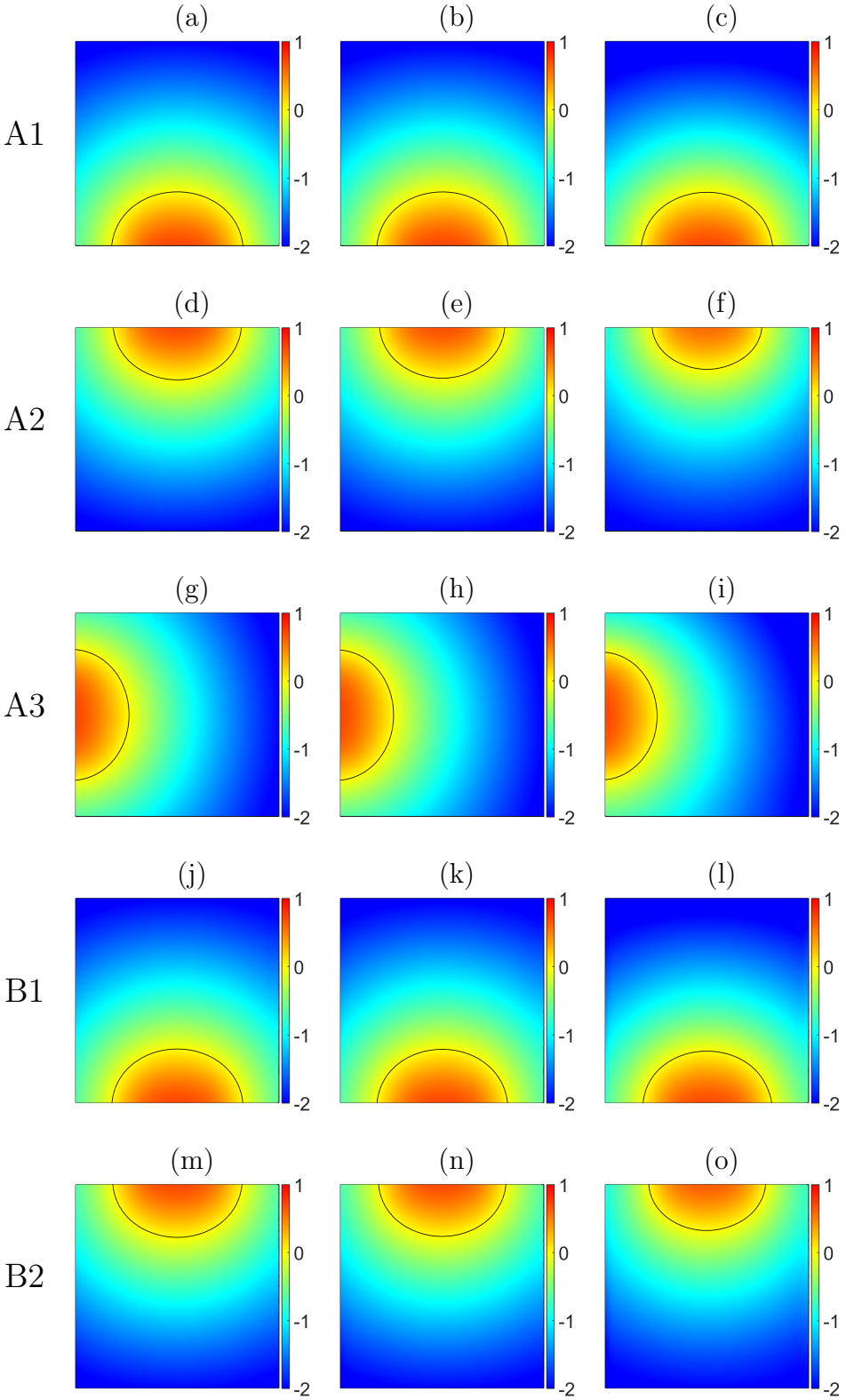

Figure 7.16: The force ratio,r, used as an indication of the relative influence of Kelvin body force on buoyancy within the cavity at temperature differences of $\Delta T = 10$ K (left), $\Delta T = 20$ K (middle) and $\Delta T = 80$ K (right).

the variation of K caused by temperature is weak when the fluid has reached saturation in a strong magnetic field but the value of K decreases strongly in a weak magnetic field. When the magnetic field reduces according to the distance to its origin, r is therefore not much affected very close to the magnet where the fluid is saturated but reduces rapidly a little further away when the fluid is below saturation shifting the $r = 0$ contour line towards the magnet indicating an equal balance of Kelvin body force and buoyancy closer to the magnet. This phenomenon is observed for all configurations. However, due to the arrangement of the body forces and the fluid's temperature the effect may be more significant for other configurations as is for (A2) shown in panel (d) to (f). Here, the shift in location is 3.2% between 10 K and 20 K and 20% between 10 K and 80 K. The difference refers to the spatial temperature distribution of the magnetic fluid within the cavity and the opposed body forces. In contrast to configuration (A1) where the cold magnetic fluid is attracted and gathered at the bottom of the cavity a small local temperature difference to the system's reference temperature is observed and results in a weak local magnetic Rayleigh number that is reflected in a small modified Rayleigh number in Fig. 7.14(b). As the modified Rayleigh number gives an indication of the effective driving force of convective heat transfer, the resulting fluid motion is small and is evident in the results presented in panel (e) and (d) of Fig. 7.4. This is different in configuration (A2) as here the cold magnetic fluid is attracted towards the top heated boundary such that the local temperature difference of the fluid to the systems reference temperature is much higher resulting in a greater local magnetic Rayleigh number as configuration (A1). This intensifies thermomagnetic convection and is evident in Fig. 7.6 as the magnetic Rayleigh number increases with the temperature difference across the system which is reflected in the modified Rayleigh number in Fig. 7.14(b) resulting in an intensification in convective heat transfer as seen in panel (e) and (f) of Fig. 7.6 where the fluid motion increases in the top of the fluid domain. The drop in the Nusselt number is understood by the different rate of increase of both body forces. While the Kelvin body force increases more slowly due to the variation of K as mentioned above, the body force ratio, r, shifts closer towards the magnet and the cavity becomes more buoyancy dominated. This is visible in the experimental and computational temperature profiles in panel (a) and (c) of Fig. 7.6 where the 0.6 and 0.7 isothermal contour lines become more horizontal at a higher system temperature difference of $\Delta T = 20$ K as shown in panel (b) and (d) indicating an increase of heat conduction throughout the system. In other words while an increases in the magnetic Rayleigh number increase convection in the top of the domain the influence of dominance of the Kelvin body force to the respective driving force decreases such that gravity becomes more dominant and heat transfer in form of conduction expands

throughout the cavity following in a decrease in the Nusselt number as seen in 7.14(b). This trend continues when the temperature increases beyond the experimentally explored results. In general the effect of the shift in r differs significantly between the direction of both body forces when both are parallel. However, the differences arise out of the temperature dependent variation of K and the respective local temperature of the fluid to the reference temperature of the system caused by the direction of the body forces. The phenomena of the shift in location is therefore moderate when the local temperature to the reference temperature of the system is small (A1) and significant when large (A2).

All these arguments can be directly transferred to configuration (A3), (B1) and (B2). When the Kelvin body force is perpendicular to gravity as is the case in configuration (A3) the shift in the $r = 0$ contour line is 0.5% between 10 K and 20 K and 3% between 10 K and 80 K. As here the body forces do not oppose each other and the local fluid temperature difference near the magnet to the system's reference temperature is smaller than in (A2) but larger than in (A1) such that the shift in location is between both configurations.

By changing the temperature boundary conditions and placing the magnet below the cavity in configuration (B1) the same effect is observed as in configuration (A1). Following, that gravity has now introduced a natural convection cell in the cavity where the Kelvin body force contributes to the convective flow such that the local temperature closer to the magnet increases as is visible by comparing the numerical solution of Fig. 7.4.1 with Fig. 7.4.4. The shift of location due to the increase in the local temperature is therefore stronger than in configuration (A1). As both body forces contribute to the convection cell the heat transfer reported in Fig. 7.15 is stronger than natural convection. This is not the case for configuration (B2) where both body forces oppose each other. Here, the developed second counter-circulating convection cell suppress natural convection in the top and reduces heat transfer across the cavity as is evident in Fig. 7.15(a). This reduces the local temperature in the top of the cavity resulting in a reduction of the local temperature to the system's reference temperature such that the magnetic Rayleigh number is smaller than in configuration (A2). Thus, the shift in location is smaller than in configuration (A2).

7.7 Summary

This section analysed thermomagnetic convection in presence of terrestrial gravity by experiments and validated by computational simulations. Both experiments and numerical simulations showed good correspondence by considering the limitation of each model.

Table 7.2: Non-dimensional distance of the $r = 0$ point along the centreline or mid-height from the wall adjacent to the magnet for all configurations.

ΔT	(A1)	(A2)	(A3)	(B1)	(B2)
10 K	0.2640	0.2564	0.2627	0.2627	0.2596
20 K	0.2636	0.2483	0.2614	0.2611	0.2549
80 K	0.2619	0.2049	0.2548	0.2522	0.2260

Furthermore, configuration (A2) showed good agreement with the numerical simulations of Chang et al. [148]. In the light of this the experimental observation and numerical simulations explained the temperature dependence of the Kelvin body force. This was evaluated by the an effective force ratio develop and introduced in eq.(6.6) and calculated with the local Rayleigh and magnetic Rayleigh number. The resulting heat transfer was quantified by the Nusselt number and evaluated against a modified Rayleigh number that considered both body forces. In summary a temperature increase across the system increases both body forces. However, the intensity in the increase differs between the body forces and can be evaluated via a force ratio, r. Secondly, the Kelvin force can induce convection where gravity is not able to e. g. (A1-A3). Thirdly, the Kelvin force is much stronger than buoyancy such as observed in configuration (A2) and (B2).

8 Alternating magnetic field

In this section a parametric numerical study was carried out to study the effect of alternating magnetic field on a magnetic fluid to induce thermomagnetic convection in the presence and the absence of gravity. The magnetic field within the cavity had a constant field gradient and was parallel and opposite to gravity. A set of frequencies for the sinusoidal variation of the magnetic field strength was used to study the magnetic fluid flow of the mineral oil based magnetic fluid with the physical properties mentioned in Tab. 6.1 by computational simulations. All frequencies investigated alternated around a zero mean value starting from 0.2 to 2 Hz. The amplitudes of the magnetic field investigated was 10^5 A/m and 10^6 A/m. As buoyancy was absent in the first case study (BG) the only active driving force for convective heat transfer related to the the applied magnetic field and the volume force acting was the Kelvin body force. As the *Curie law* states that magnetisation is inversely proportional to temperature a net acceleration of colder, and therefore more magnetised, fluid in the direction of the applied magnetic field gradient was observed. The resulting thermomagnetic convection induced by alternating magnetic fields developed flow fields of cold magnetic fluid towards higher magnetic field regions with the frequency of the magnitude of the applied magnetic field but with varying amplitude. This was similar when buoyancy was present in the second study case (BC). Here, a competition of both body forces in inverse direction developed flow patters of buoyancy dominated and Kelvin body force dominated regions that alternated with the frequency. The response of the magnetic fluid and the alternating heat transfer was characterised by the Nusselt number, Nu. The alternated convection of both study cases was reflected in the velocity and temperature profile of the magnetic fluid.

8.1 Model formulation

To get an indication of theromagnetic convection under alternating magnetic field with constant gradient a set of frequencies (0.2 Hz, 0.5 Hz, 1 Hz, 2 Hz) is studied with two different amplitudes of 10^5 A/m and 10^6 A/m respectively. The configurations investigated are shown in Tab. 8.1. The problem geometry used was the non-dimensional square cavity introduced in §6.1 and filled with the mineral oil based magnetic fluid. Figure 6.1 presents the problem geometry that was forced thermally at two opposite vertical side walls with constant temperatures of T_h and T_c respectively with $T_h > T_c$ whereas all remaining walls kept adiabatic. As the transient changes in the magnetisation due to Brownian motion and Néel relaxation were in the range of 10^{-7} s and were several orders slower than the frequency of the impost magnetic fields, both relaxation mechanism were neglected in

this study. As the problem geometry was considered in non-dimensional form a set of non-dimensional parameters were introduced to characterise heat transfer by natural and thermomagnetic convection in the following section.

8.1.1 Governing equations

The non-dimensional parameter introduced in eq.(4.59) represents the ratio of buoyancy to viscous dissipation and is a scaling strength of the acting driving forces in natural convection known as the Grashof number, Gr. A similar non-dimensional number is found in thermomagnetic convection. The temperature dependent Kelvin body force introduced in eq.(4.43) maybe used to give a scaling strength to viscous dissipation for thermomagnetic convection by using their ratio expressed as a magnetic Grashof number

$$\mathrm{Gr_m} = \frac{\mu_0 K\ \Delta T H L^2}{\rho \nu^2} \tag{8.1}$$

where $\mu_0 = 4\pi \times 10^{-7}$ is the vacuum permeability, $\Delta T = T_h - T_c$ is the temperature difference across the system, H the magnetic field, L characterisitc length scale of the problem geometry, ρ the density, ν the kinematic viscosity and K the pyromagnetic coefficient as presented in eq.(4.68) to include inter-particle interaction.

By introducing the same non-dimensional parameters as in eq.(4.71) one can write the continuity eq.(4.66)and momentum eq.(4.67) in non-dimensional form as

$$\frac{\partial u'}{\partial x'} + \frac{\partial v'}{\partial y'} = 0 \tag{8.2}$$

Table 8.1: The configurations and parameters used for simulations was based on configuration (B) with heating and cooling at the side walls. This base configuration was slitted into two subconfigurations (BG) and (BC). Configuration (BG) used a constant vertical magnetic field gradient in the positive z-direction indicated by the symbols $\nabla H|$. The second configuration (BC) used analogues to (BG) the same constant vertical magnetic field gradient in presence of buoyancy and was indexed by $\nabla H \parallel -\mathbf{g}$.

Label	Configuration	ΔT (K)	Frequency	Amplitude (H_0)
B	Heating and cooling at the sides ∇T			
BG1	constant $\nabla H\|$	10	0.2 ... 2 Hz	10^5 A/m
BG2	constant $\nabla H\|$	10	0.2 ... 2 Hz	10^6 A/m
BC1	constant $\nabla H \parallel -\mathbf{g}$	10	0.2 ... 2 Hz	10^5 A/m
BC2	constant $\nabla H \parallel -\mathbf{g}$	10	0.2 ... 2 Hz	10^6 A/m

$$\frac{\partial u'}{\partial t'} + u'\frac{\partial u'}{\partial x} + v'\frac{\partial u'}{\partial y} = -\frac{\partial p'}{\partial x} + \left(\frac{\partial^2 u'}{\partial^2 x} + \frac{\partial^2 u'}{\partial^2 y}\right) + T'\,\mathrm{Gr_m}\left(M'_x\frac{\partial H'_x}{\partial x} + M'_y\frac{\partial H'_x}{\partial x}\right) \tag{8.3}$$

$$\frac{\partial v'}{\partial t'} + u'\frac{\partial v'}{\partial x} + v'\frac{\partial v'}{\partial y} = -\frac{\partial p'}{\partial y} + \left(\frac{\partial^2 v'}{\partial^2 x} + \frac{\partial^2 v'}{\partial^2 y}\right) + T'\left[\mathrm{Gr} + \mathrm{Gr_m}\left(M'_x\frac{\partial H'_y}{\partial y} + M'_y\frac{\partial H'_y}{\partial y}\right)\right] \tag{8.4}$$

and for the heat eq.(4.69)

$$\frac{\partial T'}{\partial t'} + u'\frac{\partial T'}{\partial x} + v'\frac{\partial T'}{\partial y} = \mathrm{Pr}\left(\frac{\partial^2 T'}{\partial x^2} + \frac{\partial^2 T'}{\partial y^2}\right) \tag{8.5}$$

where $t' = tf$ is the non-dimensional time[16] and Pr the Prandtl number introduced in eq.(4.60). The heat transfer is quantified by the non-dimensional Nusselt number and may be formulated as

$$\mathrm{Nu} = \frac{L}{k\,\Delta T}\,\frac{1}{A}\int_0^L \frac{1}{2}\,(q_h + q_c)\;\mathrm{d}y. \tag{8.6}$$

where q_h and q_c is the heat flux through the hot wall and cold wall, respectively.

8.2 Computational and numerical methodology

The computational model was solved with COMSOL Multiphysics [187] a commercial solver that uses the Finite-Element technique. As the model was tested before in §6.1 the mesh test to Vahl Davis [193] benchmark solution of natural convection was equivalent. The computational simulation were performed by solving the non-dimensional eq.(8.2), eq.(8.3) and eq.(8.5) using the magnetic Grashof number, $\mathrm{Gr_m}$, in eq.(8.1) as an input value for configurations (BG). In the event when gravity was present such as in configurations (BC) the Grashof, Gr, in eq.(4.59) was used a second input value. The non-dimensional boundary conditions for temperature were $T' = 1$ for the left side wall and $T' = 0$ for the right side wall and for velocity no-slip conditions at all walls. The initial conditions for all computational simulations was a uniform distributed temperature of $T' = 0$, a dimensionless gauge pressure of $p_0 = 1$ applied on the bottom left corner of the cavity and a stagnant fluid. The magnetisation of the magnetic fluid was calculated

[16] The time, t', is written in non-dimensional form by using an appropriate parameter such as is the frequency, f, to compare the configurations studied.

via eq.(2.24) using the fluid's temperature, T, defined as

$$T = \Delta T \, T' + T_0 \tag{8.7}$$

where T_0 is the reference temperature at which the experiment was carried out and T' the local non-dimensional temperature. This provided the pyromagnetic coefficient, K. The alternating magnetic field, H, used for both configuration (BG) and (BC) was calculated by

$$H = |H_0 \sin\left(t \, 2\pi f + \frac{\pi}{2}\right)| \tag{8.8}$$

where H_0 is the respective amplitude of the magnetic field and f the frequency. The alternating magnetic field, H, and the temperature, T, of the magnetic fluid then provide the variables to calculate the Grashof numbers for each configuration which was used to solve the non-dimensional eq.(8.2-8.5) by using a transient solver.

8.3 Results

In this section the computed results are presented for alternating thermomagnetic convection in configuration (BG1) and (BG2) followed by a combined alternating thermomagnetic convection and natural convection alone in (BC1) and (BC2). As all configurations are presented in non-dimensional form, a comparison of the change in velocity magnitude and Nusselt number is in non-dimensional time from 0 to 1 and presents half a period of the alternating magnetic field. A comparison of all configurations studied is addressed in §8.4.

8.3.1 Thermomagnetic convection with configuration BG1

The first set of results evaluated is configuration (BG1) with $f = 0.2$ Hz shown in Fig. 8.1 for velocity and 8.2 for temperature. At the beginning of the period when the magnetic field has its full intensity at $t' = 0$ the velocity profile shows a domain filling convection cell in which the magnetic fluid descends at the heated side wall and rises adjusted to the cooled side wall whereas the centre of the cavity is relatively quiescent. The corresponding temperature profile below shows isotherms which are relatively flat at the heated and cooled side walls and adjacent stratified within the center of the fluid domain. When the magnetic field has significantly decreased as is the case for $t' = 0.4004$ the field gradient decreases and the Kelvin body force is small. This effect is visible and shown in the velocity profile where the magnetic field in the bottom of the cavity is not sufficient to magnetise the magnetic fluid but still strong enough in the top part closer to the

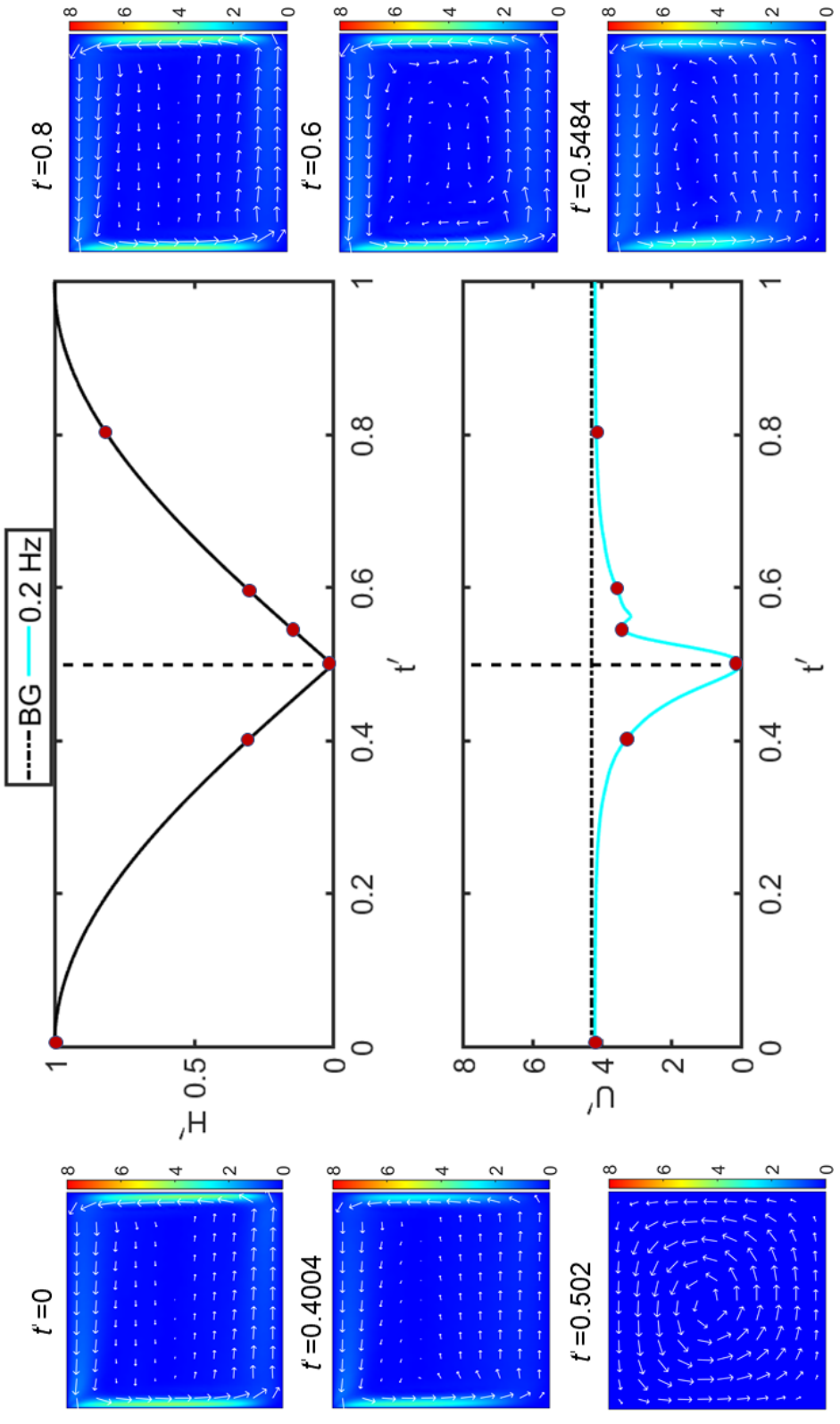

Figure 8.1: Non-dimensional velociy, u', fields (BG1) at 0.2 Hz.

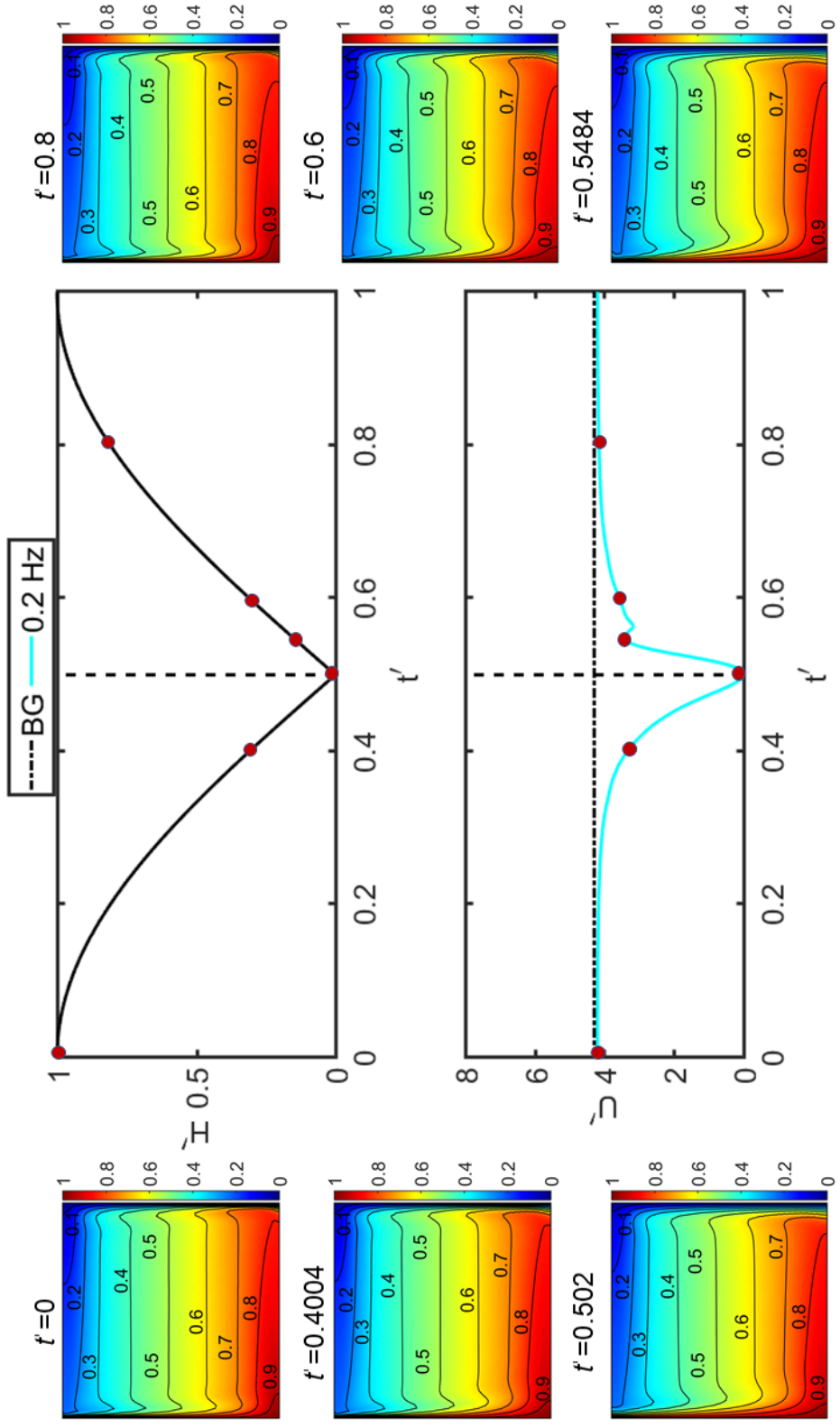

Figure 8.2: Non-dimensional Temperature, T', fields (BG1) at 0.2 Hz.

origin of the field. Thus, the established thermomagnetic convection in the bottom of the cavity reduces. The temperature field shows that and the isotherms at the bottom reflect an increase in the thermal boundary layers at the heated and cooled side wall. When the magnetic field is zero, as is the case at $t' = 0.502$ the magnetic fluid has lost its magnetisation and the Kelvin body force is zero. While the velocity arrows still reflect motion within the interior, the flow is very small and has its origin in the inertia of the magnetic fluid. As no body force is active that continues convection, heat transfer is only in form of conduction. Thus, the previously established thermal boundary layers increase further as is represented by the isotherms that flatten at the vertical side walls. However, stable equally aligned isotherms are not observed in the temperature profile as the process of the local variation in temperature is time dependent. Hence, the fluid's local temperature still contributes to an enhanced heat transfer until the fluid achieves stable equally spaced isotherms. When the magnetic field gradient increases, the top part of the fluid domain is higher magnetised and the Kelvin body force increases. As seen in $t' = 0.5484$ thermomagnetic convection recovers and the magnetic fluid ascends again at the left cooled side wall and descends at the heated side wall in the top part of the cavity. The corresponding temperature profile reflects the increase in heat transfer by convection and the thermal boundary layers decrease as seen by the isotherms moving closer to the heated and cooled boundary. A further increase in the magnetic field seen in $t' = 0.6$ increases the influence of the Kelvin body force throughout the cavity and more fluid is magnetised. Thus, the thermomagnetic convection cell expands through the full domain as presented in $t' = 0.8$ and the intensity of convective flow increases to a maximum. This cycle is repeated when the magnetic field intensity drops again with the same velocity and temperature fields as presented.

To evaluate the response of the magnetic fluid and the effect on heat transfer a comparison of the alternating non-dimensional magnetic field, H', velocity magnitude, U', and Nusselt number, Nu, is plotted versus the non-dimensional time, t', in Fig. 8.3. It is clear that the alternating magnetic field affects the fluid's velocity and convective heat transfer of the interior significantly. Here, the magnetic fluid response to the alternating magnetic body force in a certain time scale, the inertial time scale. While the magnetic fluid's inertia plays a significant role, the response of the fluid to the applied alternating body force varies with frequency. Thus, the magnetic fluid has a shorter time to respond to the change in the alternating intensity of the applied body force if the frequency is high. As the response time of the magnetic fluid determined by its inertia, becomes longer than the time in which the applied forces change, the shift of the curves to right becomes stronger, leading to an increasing phase lag in velocity and Nusselt number.

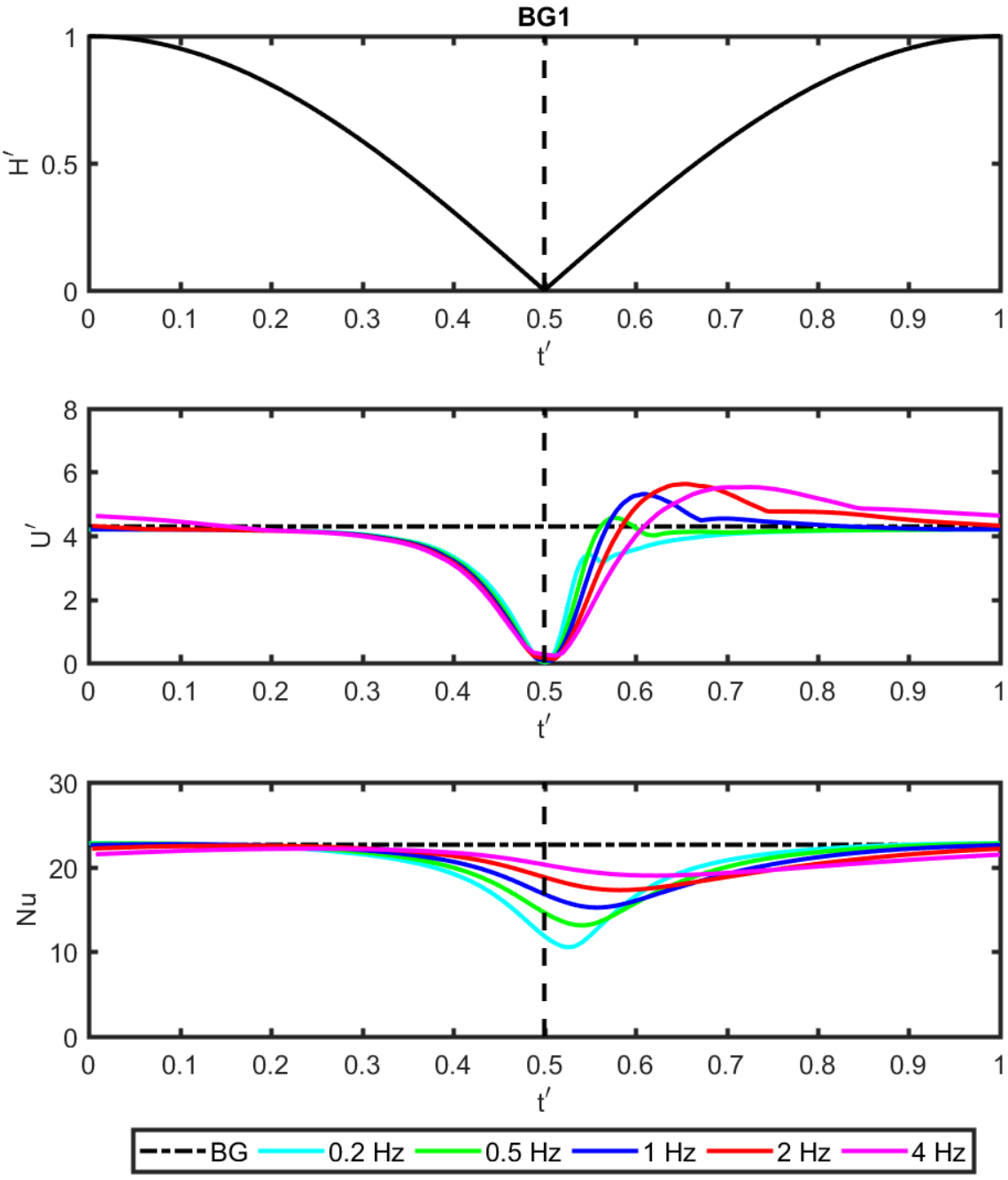

Figure 8.3: Non-dimensional magnetic field, H', velocity magnitude, U', and Nusselt number, Nu, plotted versus the time, t', for configuration (BG1).

2020 However, the shift of the maxima in velocity magnitude to the right is primarily driven by temperature differences. This is well observed in the temperature profiles in Fig. 8.2 at the heated and cooled boundaries, where the isotherms flatten when the Kelvin body force is small. There, the magnetic fluid gets colder via heat conduction at the cooled boundary and is therefore higher magnetised when the Kelvin body force returns

resulting in a stronger acceleration of the cold fluid. This effect may be explained by a thermal diffusivity time scale. The scale is understood by the temporal change in the spatial distribution of the temperature via heat conduction when the Kelvin force is small. Thus, the clear maxima of each velocity curve can now be explained by the thermal and viscous diffusivity time scale of the magnetic fluid. Here, at low frequencies the fluid's thermal diffusivity time scale is high as the Kelvin body force is small or even absent over a longer period. This changes the fluid's temperature at the cooled and heated boundaries and effects the spatial temperature distribution within the interior. If the thermal diffusivity time scale is large the temperature distribution of the interior was more stronger affected by heat conduction resulting in a higher magnetisation and a stronger acceleration of the cold magnetic fluid. Thus, the gradient of the velocity magnitude is higher at lower frequencies. The range between the minima, maxima and velocity magnitude smoothing to a fairly constant value is explained via the viscous diffusivity time scale. Here, the spatial temperature distribution is reorganised within the interior by thermomagnetic convection. The time scale to reorganise the temperature distribution to a "steady state solution" is the viscous diffusivity time scale. Thus, at low frequencies the time is large enough to reorganise the temperature distribution within the interior. At higher frequencies the time is to short to reorganise the temperature distribution and the fast increase in magnetic field intensity shifts the peak upwards and towards the right. However, the rate of the upwards shift of the maxima in velocity magnitude as seen for 0.2 to 2 Hz decreases when frequency rises and a clear maximum may be observed between 2 and 4 Hz such that a further increase in frequency would shift the maxima in velocity magnitude downwards. This refers to the decreasing gradient in velocity magnitude that gets smaller at higher frequencies. Here, the thermal diffusivity time scale is small for a significant temporal change in the spatial distribution of the temperature via heat conduction and has its origin in the Kelvin body force that is small over a short time.

The three effects of the fluid's inertia, thermal diffusivity time scale and viscous diffusivity time scale impact the Nusselt number significantly. The bottom graph were Nu is plotted versus H' reflects a clear minimum of the Nusselt number for each configuration. The phase shift towards the right and the upwards shift of the minima when the frequency increases depends on three time scales that impact on the temperature distribution of the interior.

To get an indication of the variation in velocity magnitude, U', and Nusselt number, Nu, during the process of a changing alternating field both parameters are plotted versus the non-dimensional magnetic field intensity, H', in Fig. 8.4. Here, the velocity magnitude plotted in the top graph shows the response of the magnetic fluid to the alternating field

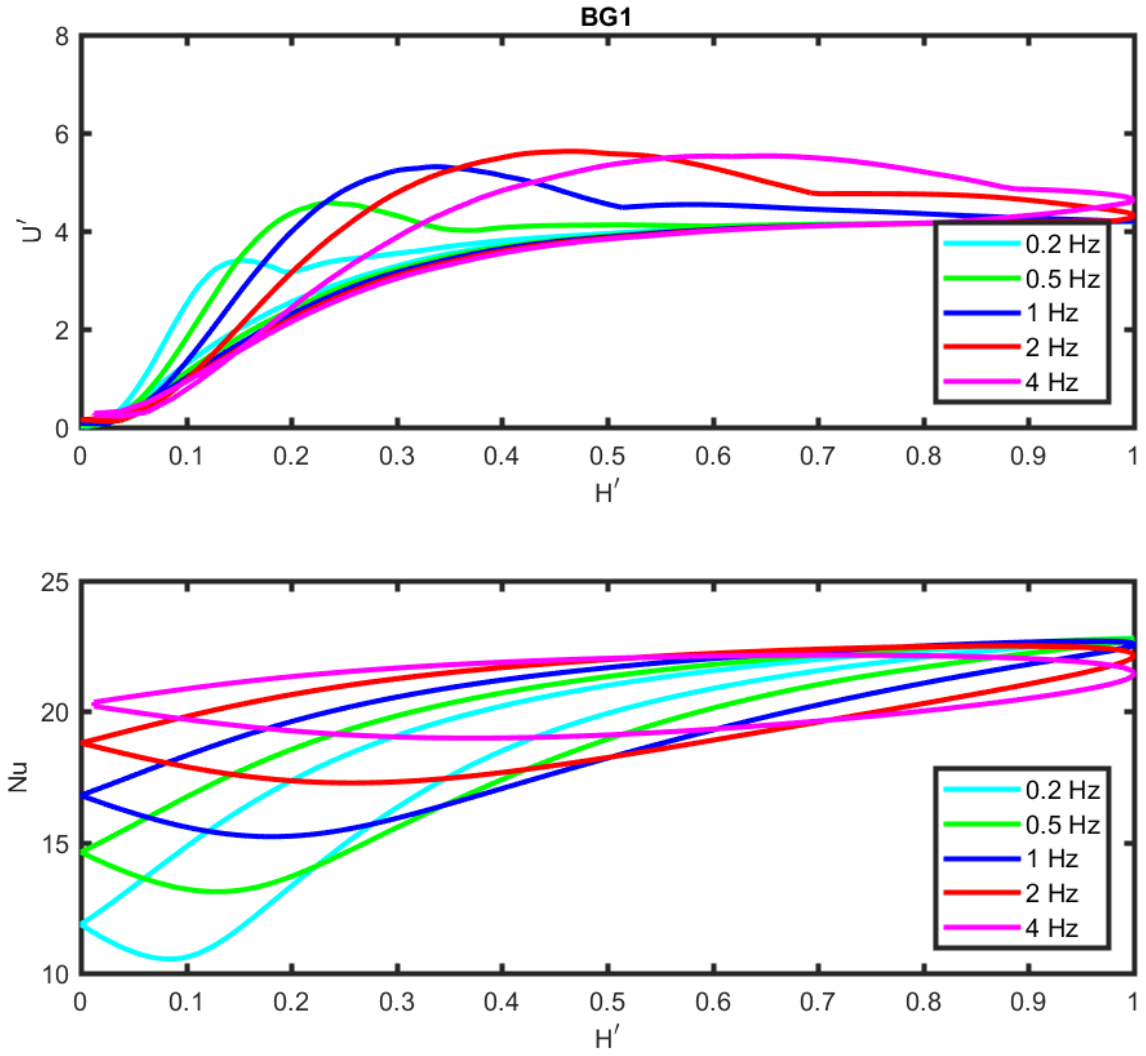

Figure 8.4: Non-dimensional velocity magnitude, U', and Nusselt number, Nu, plotted versus the magnetic field, H', for configuration (BG1).

and reflects the shift towards the right when the frequency is increased. The quantitative characterisation of the heat transfer is expressed via the Nusselt number and is plotted in the graph below versus H'. Here, a minima in Nu is seen for each configuration and relates to the three time scales of the magnetic fluid. The inertia, viscous diffusivity and
2065 thermal diffusivity scale. The upwards shift in the minima is understood by the short time scale to rearrange the temperature field according to the viscous diffusivity and thermal diffusivity scale. The same effect causes the phase lag in Nu which is 8.5% of the period at 0.2 Hz and increase with frequency to 26% and 37% for 2 Hz and 4 Hz respectively.

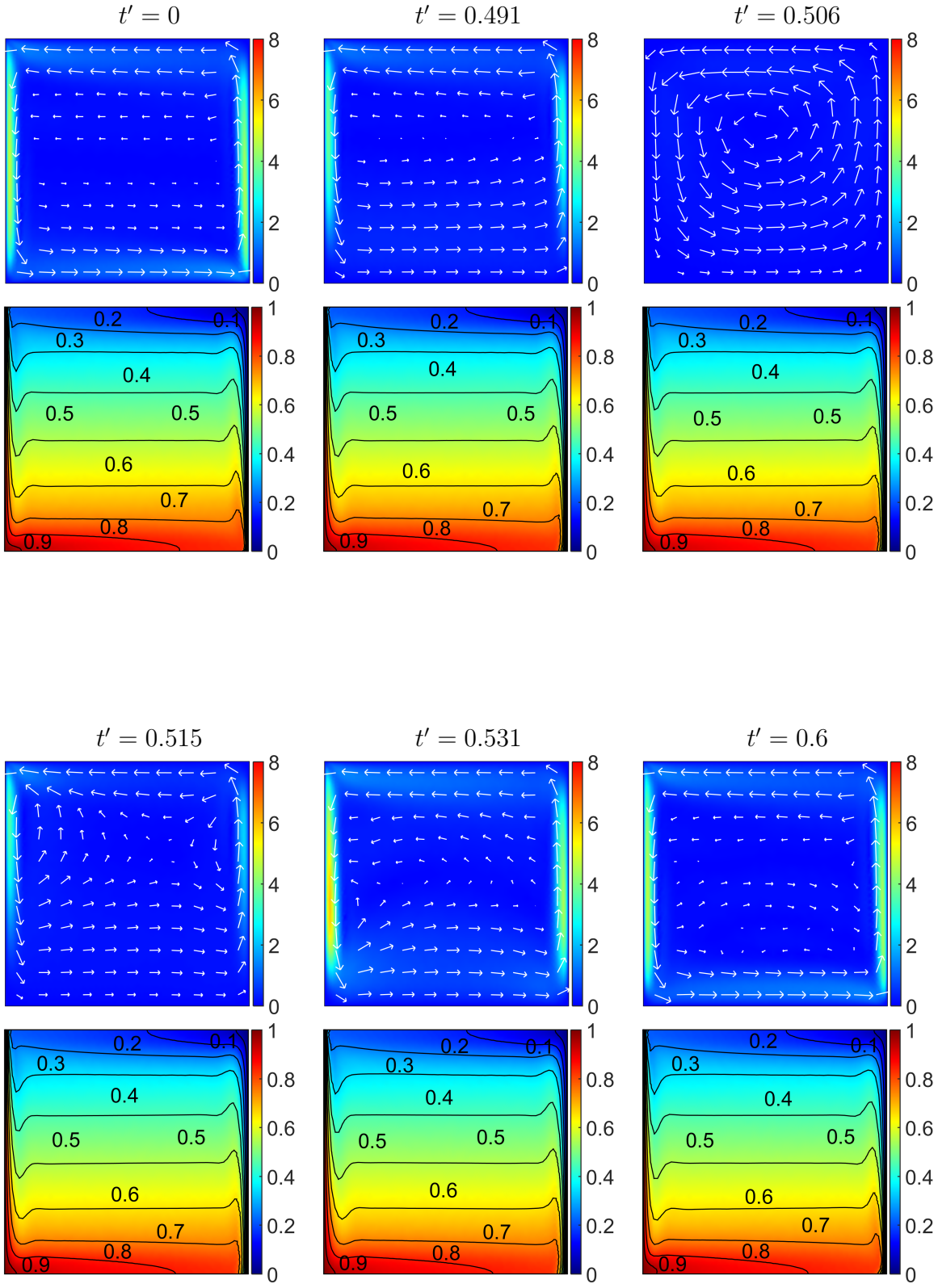

Figure 8.5: Non-dimensional velocity, u', (top row) and temperature, T', fields (bottom row) of configuration (BG2) at 0.5 Hz.

8.3.2 Thermomagnetic convection with configuration BG2

By increasing the amplitude from 10^5 A/m to 10^6 A/m the magnetic fluid is magnetised over a longer time of the cycle. Results in Fig. 8.5 indicate a start of the period that is equivalent in its structure to configuration (BG1) even with a higher frequency of 0.5 Hz. At the beginning when $t' = 0$, the magnetic field is at its highest intensity following in a saturated magnetic fluid with a domain filling thermomagnetic convection cell. When the field intensity drops according to the frequency, the fluid is still saturated for a longer period as in configuration (BG1) after it loses its magnetisation. The first change is observed at about $t' = 0.48$ and is significantly later as in (BG1). The first difference in the velocity field is noted in the bottom of the fluid domain where the magnetic field gradient is not strong enough to magnetise the fluid and the velocity field changes to $t' = 0.491$. Here, the Kelvin body force is as in configuration (BG1) sufficient enough to overcome viscous dissipation in the top of the fluid cavity but insufficient in the bottom. When the magnetic field is zero, the fluid has no magnetisation resulting in an absence of the Kelvin body force. Here, the inertia of the fluid becomes visible in the remaining advection of momentum presented in $t' = 0.506$ where the fluid moves very slowly. This is equivalent to (BG1) $t' = 0.502$. When the magnetic field increases again the Kelvin body force recovers and thermomagnetic convection starts in the top of the cavity as seen in $t' = 0.515$ and expands to a domain filling convection within the cavity at $t' = 0.6$. All temperature fields are marginally affected by the time-varying convective flow structure. This refers to the thermal diffusivity time scale that is too small to make significant changes to the temperature field via conductive heat transfer when the magnetic fluid is fairly stagnant. Thus, the effect is more distinctive for configuration (BG1) due to the lager time scale where the Kelvin body force is small.

The higher amplitude of 10^6 A/m keeps the magnetic fluid magnetised over a longer period even when the magnetic field decreases. This is well reflected in Fig. 8.6 where all minima and maxima move closer together. Thus, the time scale of a change in the intensity of the Kelvin body force is much shorter than in configuration (BG1). This is well seen in Fig. 8.5 where the temperature distribution is very little affected by the thermal diffusivity time scale. A good indication of the marginal change in temperature distribution by heat conduction is a comparison of the 0.7 contour line near the cooled boundary at different non-dimensional times. The thermal diffusivity time scale is therefore still able to make marginal changes to the interiors temperature distribution. As introduced in §8.3.1 the thermal diffusivity time scale corresponds with the viscous diffusivity time scale such that it was stated that a clear maximum may be observed between 2 and 4 Hz. This effect is

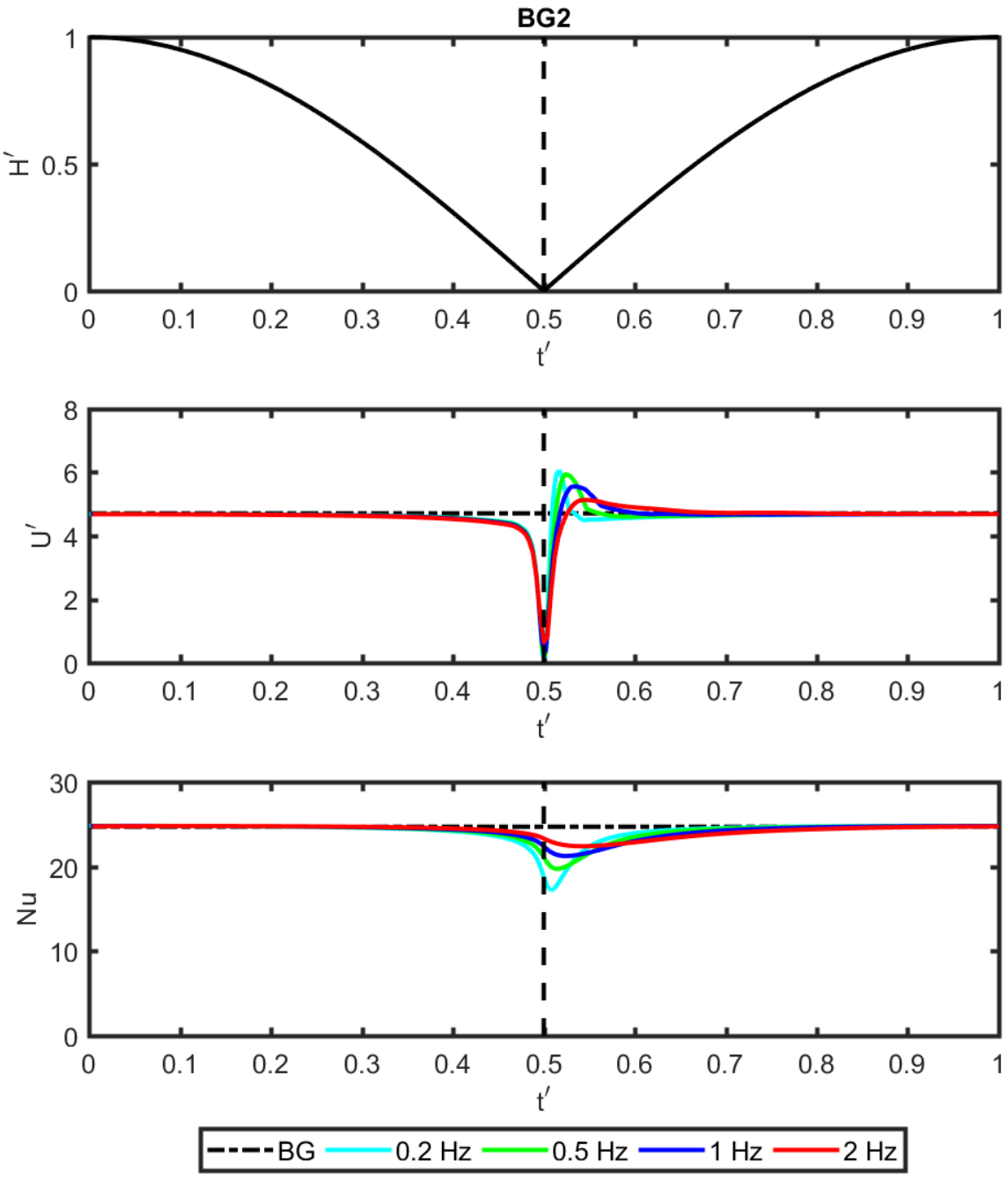

Figure 8.6: Non-dimensional magnetic field, H', velocity magnitude, U', and Nusselt number, Nu, plotted versus the time, t', for configuration (BG2).

also applicable when the amplitude of the magnetic field is higher. Here, the competition between both time scales shifts the maxima downwards when frequency increases. As the viscous time scale is rearranging the temperature field the velocity curves shift towards the right. As the magnetic fluid is magnetised over a longer period the change in Nu moves closer together and reflects the change in the velocity magnitude. The phase shift

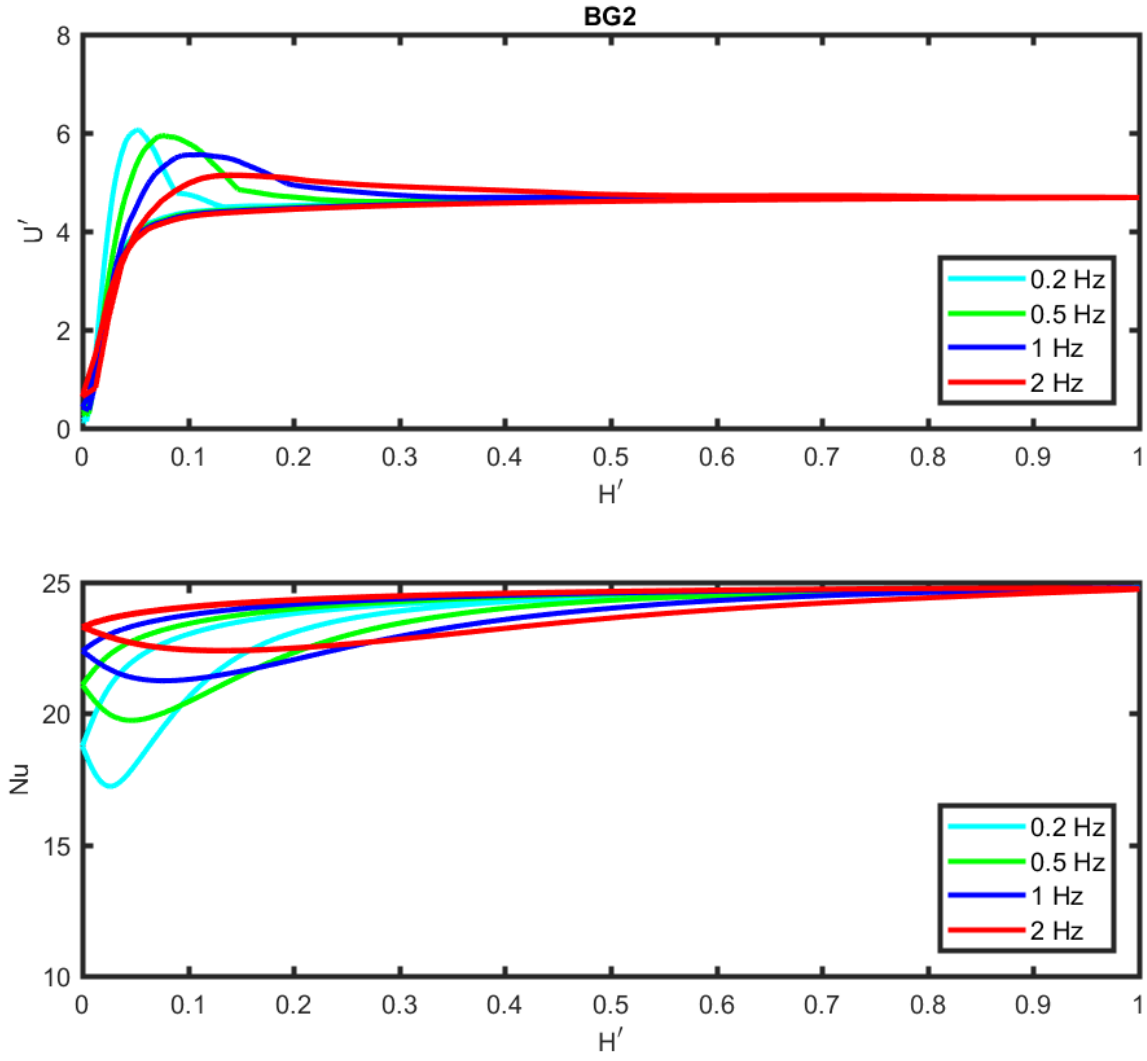

Figure 8.7: Non-dimensional velocity magnitude, U', and Nusselt number, Nu, plotted versus the magnetic field, H', for configuration (BG2).

is therefore significantly smaller than in configuration (BG1).

Plotting the velocity magnitude versus H' as is presented in Fig. 8.7 the inertia of the fluid becomes visible at $H' = 0$. There, the velocity is above zero and is a result of the inertial time scale as the fluids response time becomes longer than the time in which the applied forces change. This and the time in which the applied magnetic field changes impacts the thermal diffusivity time scale and the phase lag of the Nu towards the right is smaller as compared in (BG1). The phase in Nu at 0.2 Hz is 2.6% of the period and for 2 Hz 13% of the period.

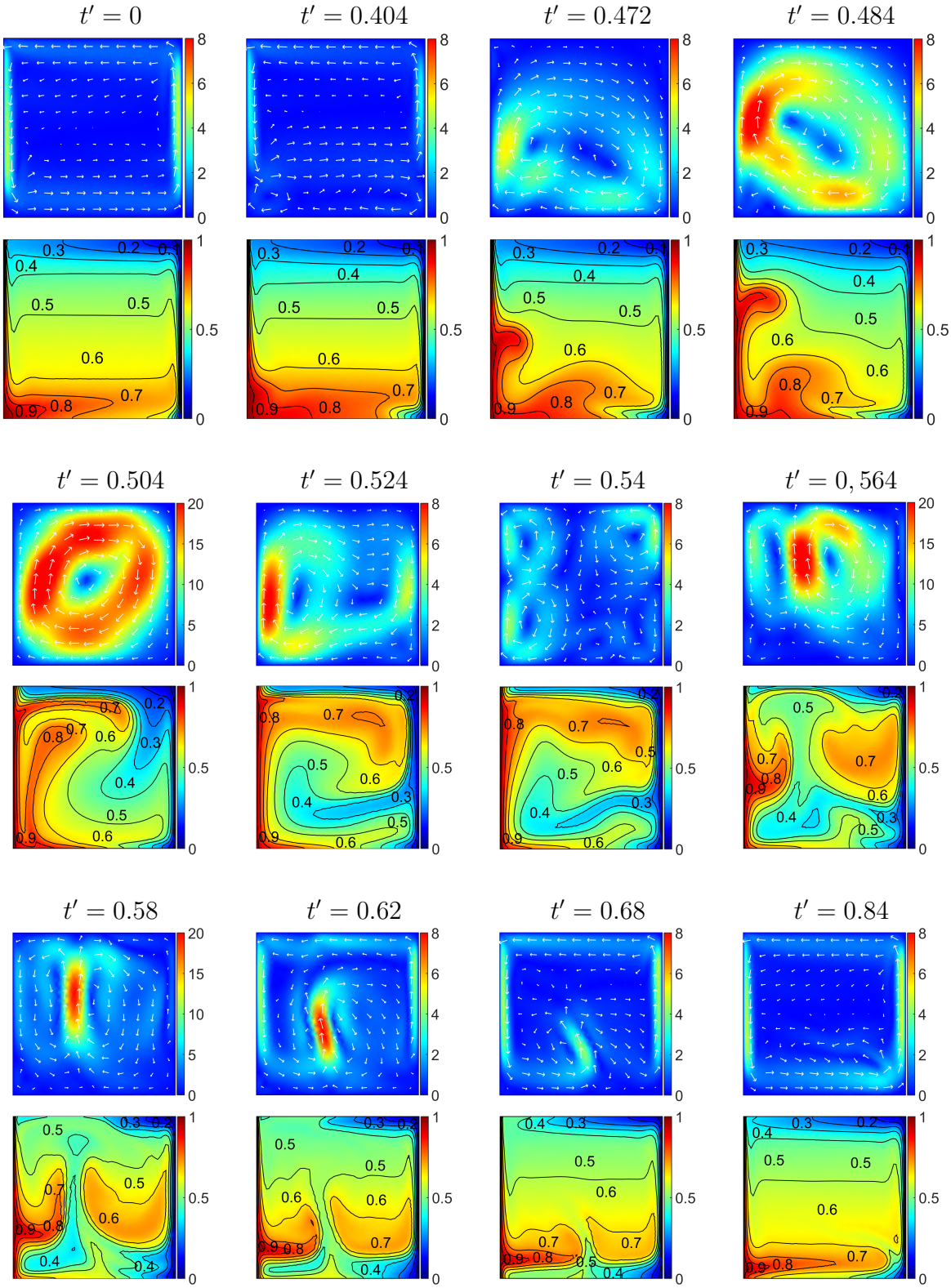

Figure 8.8: Non-dimensional velocity, u', (top row) and temperature, T', fields (bottom row) of configuration (BC1) at 0.2 Hz.

8.3.3 Thermomagnetic convection with configuration BC1

In the presence of gravity the fluid is additionally influenced by buoyancy. The results for the velocity and temperature distribution within the cavity for an alternating frequency of 0.2 Hz are presented in Fig. 8.8. At the start of the cycle ($t' = 0$) the magnetic field intensity is at its maximum and the fluid domain is fully dominated by a single thermomagnetic convection cell. Here, the cold fluid ascends at the left heated wall and descends at the cooled wall whereas the centre of the cavity remains relatively quiescent. The temperature field below reflect this. However, a significantly higher temperature distribution in the centre of the fluid domain is observed compared to (BG1) where buoyancy is absent.

When the magnetic field intensity decreases, the magnetic fluid loses its magnetisation first in the bottom of the domain as seen in $t' = 0.404$ and two counter-rotating convection cells develop. The convection cells in the bottom of the cavity have their origin in a gravitational dominated flow regime whereas the thermomagnetic convection cell is pushed upwards towards the centre of the cavity. The corresponding temperature profile reflects the change in convection such that the bottom left and right side isotherms move towards the upper centre of the cavity. This intensifies at $t' = 0.472$. Here, the velocity increases and hot fluid from the heated left side wall moves towards the top whereas cold fluid descends at the right side wall towards the bottom. At $t' = 0.484$ the velocity profile intensifies further and the structure indicates a domain that is fully dominated by buoyancy and a natural convection cell has developed. Here, the cold fluid with higher density descends at the right wall whereas hotter less dense fluid moves upwards at the heated side wall. This is reflected in the temperature field where the isotherms extend away from the top boundary. When the magnetic field intensity is at its minimum ($t' = 0.504$) the buoyancy dominated convection cell rearranges the temperature field and injects the cold fluid from the top wall towards the right centre of the cavity forcing hot fluid from the bottom and centre of the cavity upwards. As seen in the temperature field a small layer of cold fluid remains at the top of cavity whereas below a tongue of warm fluid extends from the heated side wall towards the cooled side wall. In $t' = 0.524$ the velocity within the cavity decreases significantly as buoyancy has turned the thermomagnetic dominated convection cell into a gravitational counter-circulating cell. Thus, the heated fluid is on the process to rearrange the temperature field according to a gravitationally dominated convection cell. This is followed in $t' = 0.54$ where the velocity decreases in the bottom of the fluid domain and shifts the hot layer slowly upwards. The injected cold fluid from the top of the fluid domain to the centre of the cavity starts also settling further downwards

whereas the hot fluid remains at the top below the small cold layer that has decreased in size at the left side but increased at the right. This relates to the magnetic field intensity that is increasing such that the top part of the fluid is magnetised again resulting in two small thermomagnetic convection cells that start attracting cold fluid from the right side wall towards the left. A further increase in magnetic field intensity increases the Kelvin body force which overcomes buoyancy and the fluid domain rearranges again as seen in $t' = 0.564$. Here, the velocity increases and the Kelvin body force that dominates the cavity attracts colder higher magnetised fluid from the bottom through the centre of the domain upwards to form a mushroom shape of cold fluid in the top. The hotter less magnetised fluid arranged by natural convection is therefore displaced by cooler fluid and forced to move downwards at the left and right side wall. A jet of cold fluid that separates the hot fluid regions at the left and right side is supplied by a layer of cold fluid from the bottom of the cavity. This process is further developed in $t' = 0.58$ and $t' = 0.62$ where the magnetic field increases and the Kelvin body force becomes the dominant force in the interior. Thus, the hot fluid moves further down at the left and right side walls and the cold layer below decreases by injecting cold fluid upwards towards higher magnetic field regions in the centre of the domain that separates the two hot regions. This effect leads to a mixing in hot and cold fluid such that the temperature in the centre of the domain becomes warmer and is stably stratified as seen in $t' = 0.68$ when the magnetic field intensity increases further. Here, the cold layer at the bottom decreased further and the tongue that injects the cold fluid into the top centre of the cavity is pushed by the hot fluid that descends at the left wall towards the right side of the cavity. Hence, the increases in temperature observed in the centre of the cavity compared to (BG1) refer to the mixing of magnetic fluid by changing the temperature distribution during the cycle. In $t' = 0.84$ the hot fluid has moved the remaining cold layer at the bottom of the cavity towards the right side wall where it still injects marginally cold fluid into the centre and towards the top right side wall to form the initial flow structure seen in $t = 0$ to repeat the cycle when the magnetic field has reached its maximum.

As seen in (BG1) and (BG2) the alternating frequency affects the response of the magnetic fluid and has a significant influence on the convective structure within the cavity. By increasing the frequency from 0.2 Hz to 1 Hz the effect of a gravity dominated fluid domain is still present but flow structures may be developed differently and relate to the viscous diffusivity time scale. Fig. 8.9 presents the results of (BC1) with a frequency of 1 Hz. Results suggest a significant difference in the temperature and flow fields compared to the 0.2 Hz case. As seen in $t' = 0$ the temperature distribution in the fluid interior does not reflect a relative constant temperature in the centre and the temperature gra-

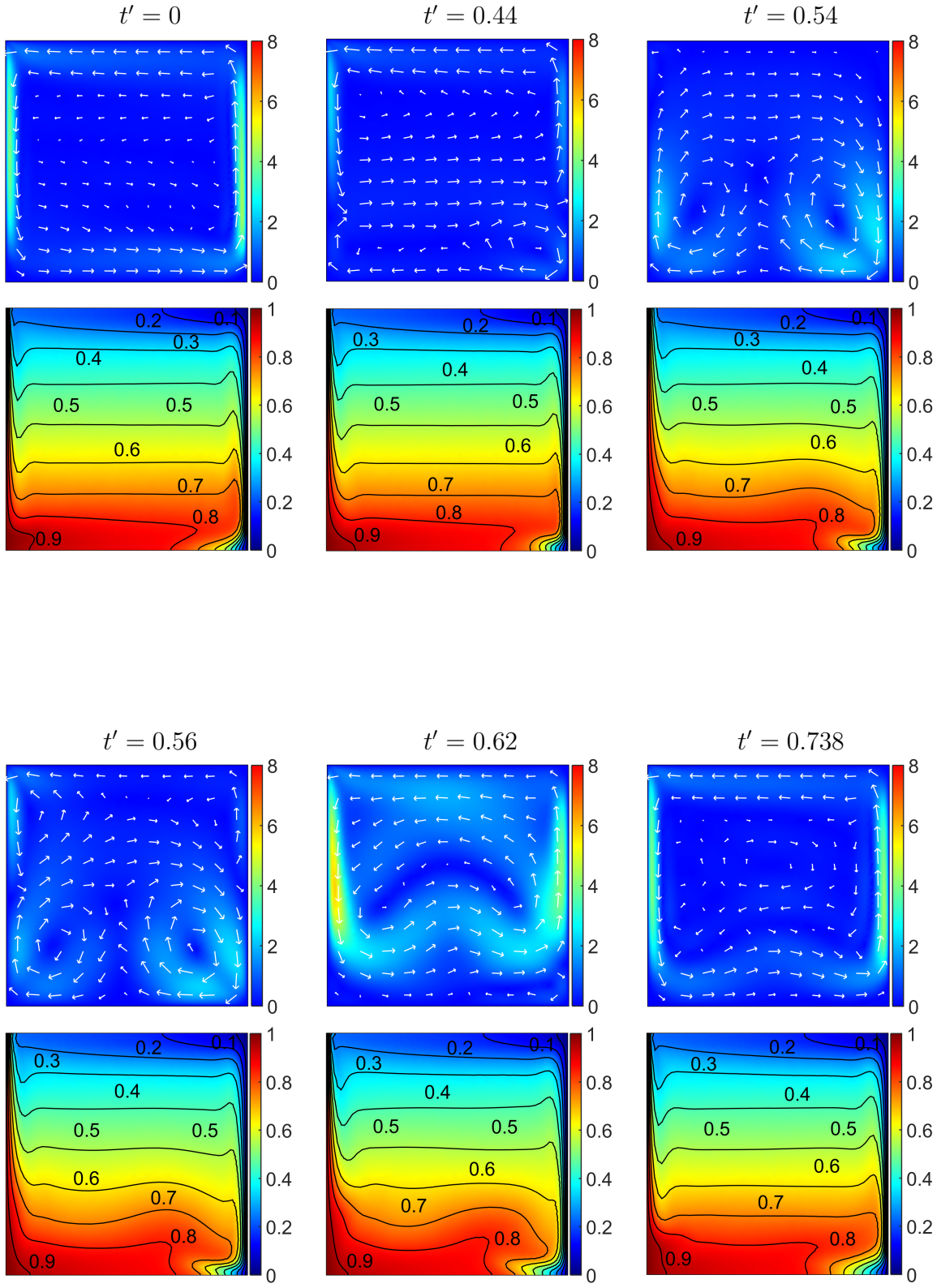

Figure 8.9: Non-dimensional velocity, u', (top row) and temperature, T', fields (bottom row) of configuration (BC1) at 1 Hz.

dient is fairly linear compared to the 0.2 Hz simulation. This indicates that a mixing of hot and cold fluid does not occur and flow fields are unable to establish like in the 0.2 Hz configuration. As seen in $t' = 0.44$ the flow structure established in the bottom of the cavity has gravitational origins that is comparable with the $t' = 0.404$ of the 0.2 Hz case. However, to rearrange the temperature field a certain time scale is needed. As one has observed in configuration (BG1) and (BG2) the viscous diffusivity time scale requires a long time to make significant chances in the temperature interior. Thus, the developed flow in $t' = 0.54$ in the bottom part of the fluid domain with gravitational origins has developed far before the minimum of the magnetic field such that the velocity due to buoyancy in the bottom part of the cavity is increasing and starts affecting the temperature field. When the magnetic field increases further the top part becomes dominated by the Kelvin body force again as seen in $t' = 0.56$ developing a single counter-rotating cell that pushes the two natural convections cells downwards. While the magnetic fluid is still influences by the dominating buoyancy at the bottom the temperature field is still subjected to gravitational changes and the isotherms move upwards indicating a motion of hot fluid towards the top. With the increase in magnetic field intensity the Kelvin body forces increases and as seen in $t' = 0.62$ the thermomagnetically induced convection cell expands further downwards such that the isotherms align horizontal in the centre of the interior as presented in $t' = 0.738$. As a result of the small period the viscous diffusivity time scale is insufficient to establish the significant change in the temperature field caused by gravitational origins as seen for the lower 0.2 Hz frequency.

As gravity is now operating as a second body force the impact on convective flow is significant when the Kelvin body force and frequency is small. Fig. 8.10 shows a significant increase in U' when the magnetic field drops and buoyancy becomes the dominating body force as seen for the 0.2 Hz configuration. Here, the viscous diffusivity time scale is large and gravity has a significant impact changing the temperature distribution within the cavity and establishes a natural convection cell as described in details above. When the Kelvin body force recovers the velocity magnitude drops again significantly to a minimum. However, when the Kelvin body force overcomes buoyancy and becomes the dominant force again, the temperature field is formed back to the original temperature distribution of the thermoconvective cell, filling the complete cavity. For higher frequencies the viscous diffusivity time scale is too small and the fluid is not able to respond as fast to the changing body forces such that the temperature distribution is less affected. The Nusselt number shows this in the graph below. Here, the 0.2 Hz curve with a large viscous diffusivity time scale the Nusselt number peaks at $t' = 0.5168$ and reflects a heat transfer enhancement by natural convection. Thus, two phase lags in Nusselt number are observed when the

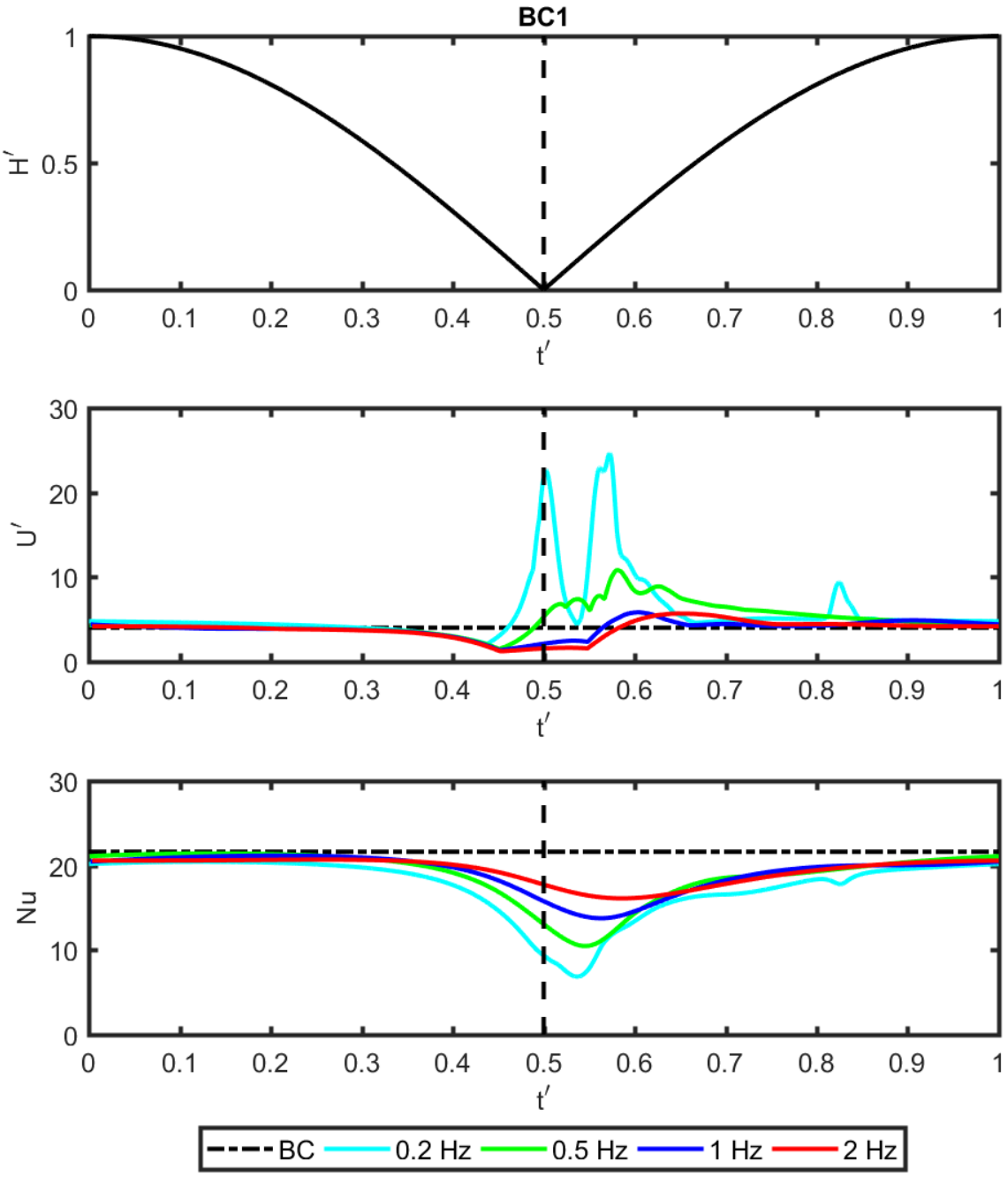

Figure 8.10: Non-dimensional magnetic field, H', velocity magnitude, U', and Nusselt number, Nu, plotted versus the time, t', for configuration (BC1).

frequency is small.

2225 The velocity magnitude curve in Fig. 8.11 shows the effect of the change in velocity over the alternating magnetic field and reflects the results observed in Fig. 8.10. Here, a first phase lag in Nu is seen for the 0.2 Hz case at 4.5% of the period where buoyancy is able to induce a fully developed natural convection cell that contributes to an enhanced

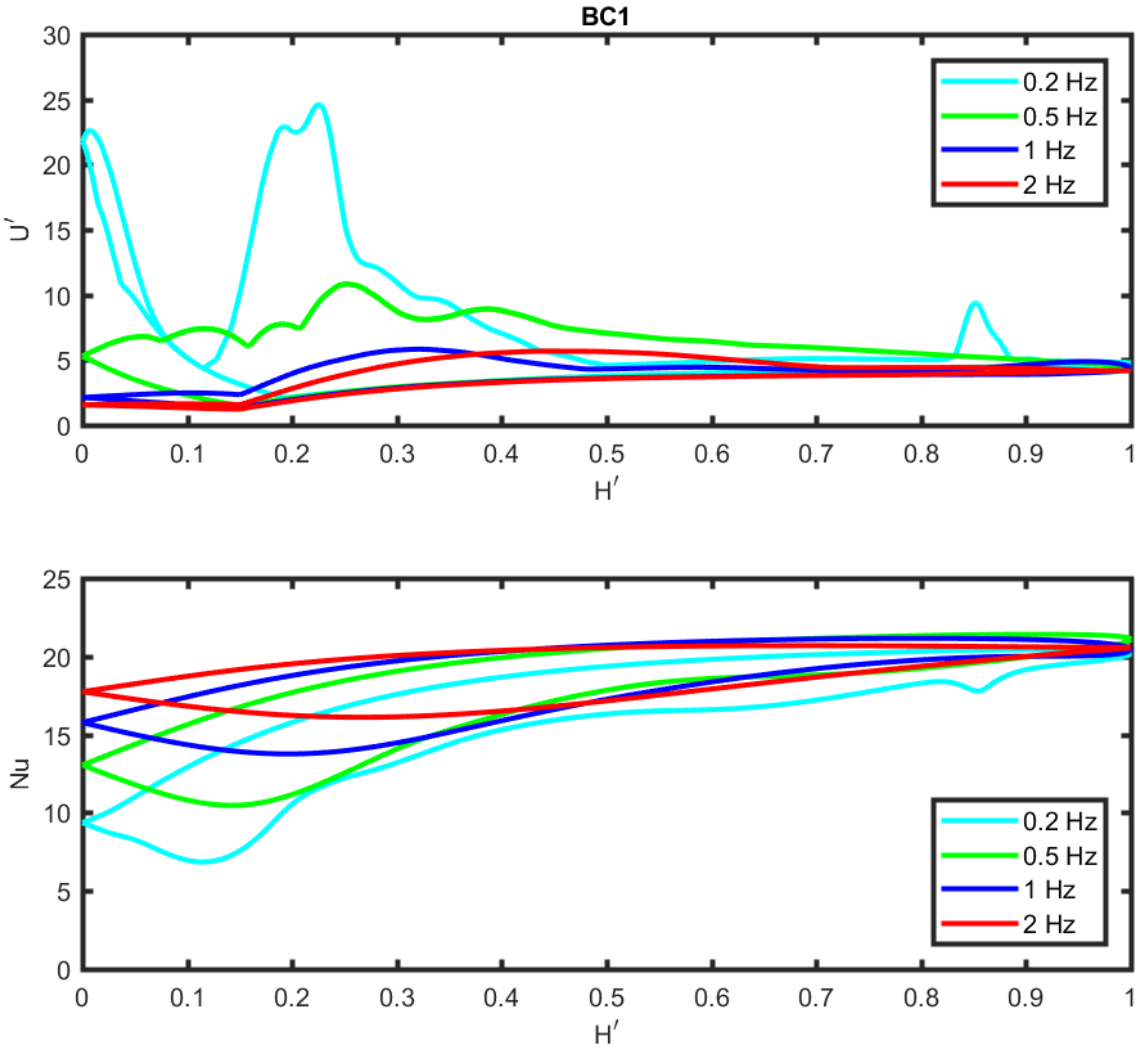

Figure 8.11: Non-dimensional velocity magnitude, U', and Nusselt number, Nu, plotted versus the magnetic field, H', for configuration (BC1).

heat transfer for a certain period which is also visible in the velocity magnitude profile above. The second phase lag is at 11.4% when thermomagnetic convection overpowers gravity and rearranges convection within the fluid interior. Both phase lags arise out of the viscous diffusivity time scale. At larger frequencies the effect is due to the small viscous diffusivity time scale not achievable and the phase lag of Nu is observed of 27.3% for a 2 Hz frequency.

8.3.4 Thermomagnetic convection with configuration BC2

While a higher amplitude of 10^6 A/m magnetises the magnetic fluid over a longer period of the cycle as observed in configuration (BG2), the same configuration is applied in presence

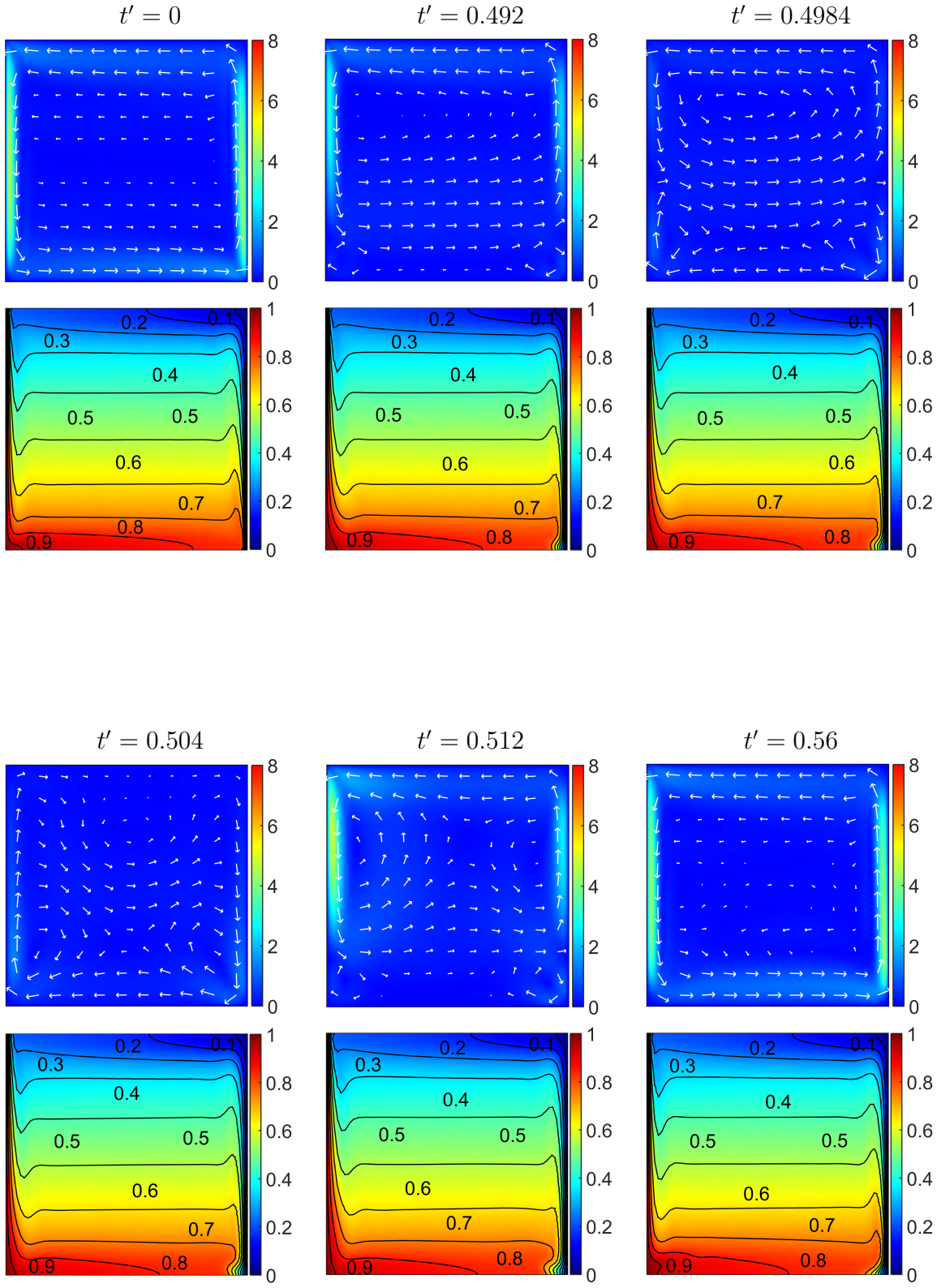

Figure 8.12: Non-dimensional velocity, u', (top row) and temperature, T', fields (bottom row) of configuration (BC2) at 0.2 Hz.

of gravity. Results in Fig. 8.12 suggest the same phenomena as reported in (BG2) where temperature fields are less effected with a higher amplitude and the fluid is not able to respond as rapidly to the change of the alternating Kelvin body force to induce significant changes as is the case in (BC1) for 0.2 Hz. In other words, the viscous diffusivity time scale is too small to achieve a significant change in the velocity that may affect the temperature distribution within the cavity. As observed at the initial position when $t' = 0$ the velocity and temperature fields are similar to configuration (BG1) and (BG2). Here, the fluid domain is controlled by the Kelvin body force and a thermomagnetic convection cell rotates counter-clockwise. When the magnetic field drops the Kelvin body force losses its dominance at the bottom of the domain and two gravitationally dominated small convection cells appear. This was also observed for configuration (BC1) seen in Fig. 8.8 and Fig. 8.9. However, the appearance of the natural convection cells is at $t' = 0.492$ firstly noted and therefore significantly later observed as in the previous configuration. The origin refers to the same reason as in (BG2) of a saturated magnetic fluid over a longer time frame of the cycle that is subjected to the magnetic field intensity. The developed natural convection cells at the bottom are now only able to develop marginal effects to the temperature fields in the bottom of the cavity. Here, the developed boundary layers increase and the isotherms at the right wall align horizontally whereas the cold fluid moves from the right wall marginally towards the centre of the bottom wall. As seen in $t' = 0.4984$ and $t' = 0.504$ the top convection cell has now disappeared when the magnetic field was unable to magnetise the magnetic fluid. Thus, the flow refers to the inertial time scale and is the remaining inertial velocity when the Kelvin body force was present. As the fluid was unable to respond as quickly the cavity's temperature distribution is little affected at the top as the viscous diffusivity time scale is too small. At the bottom of the cavity buoyancy was dominant for a longer time such that the temperature was affected by the viscous diffusivity time scale and changes in the temperature distribution was made and is seen in $t' = 0.504$. There, the temperature field changed and the cold fluid at the bottom extended marginal further towards the left heated side wall. When the magnetic field increased again the top of the fluid domain was dominated by the Kelvin body force and the small natural convection cells disappeared at $t' = 0.56$ and the cold fluid at the bottom pushed back into the counter-clockwise thermomagnetic convection cell to restart the cycle at position $t' = 0$.

Fig. 8.13 presents the correlation of U' and Nu to the alternating magnetic field intensity. Here, all graphs are equivalent and are explained via the viscous diffusion time scale introduce in §8.3.1 in relation to buoyancy. Thus, the thermal diffusion time scale is absent in (BC2) as seen in the minima of velocity magnitude that are significantly above

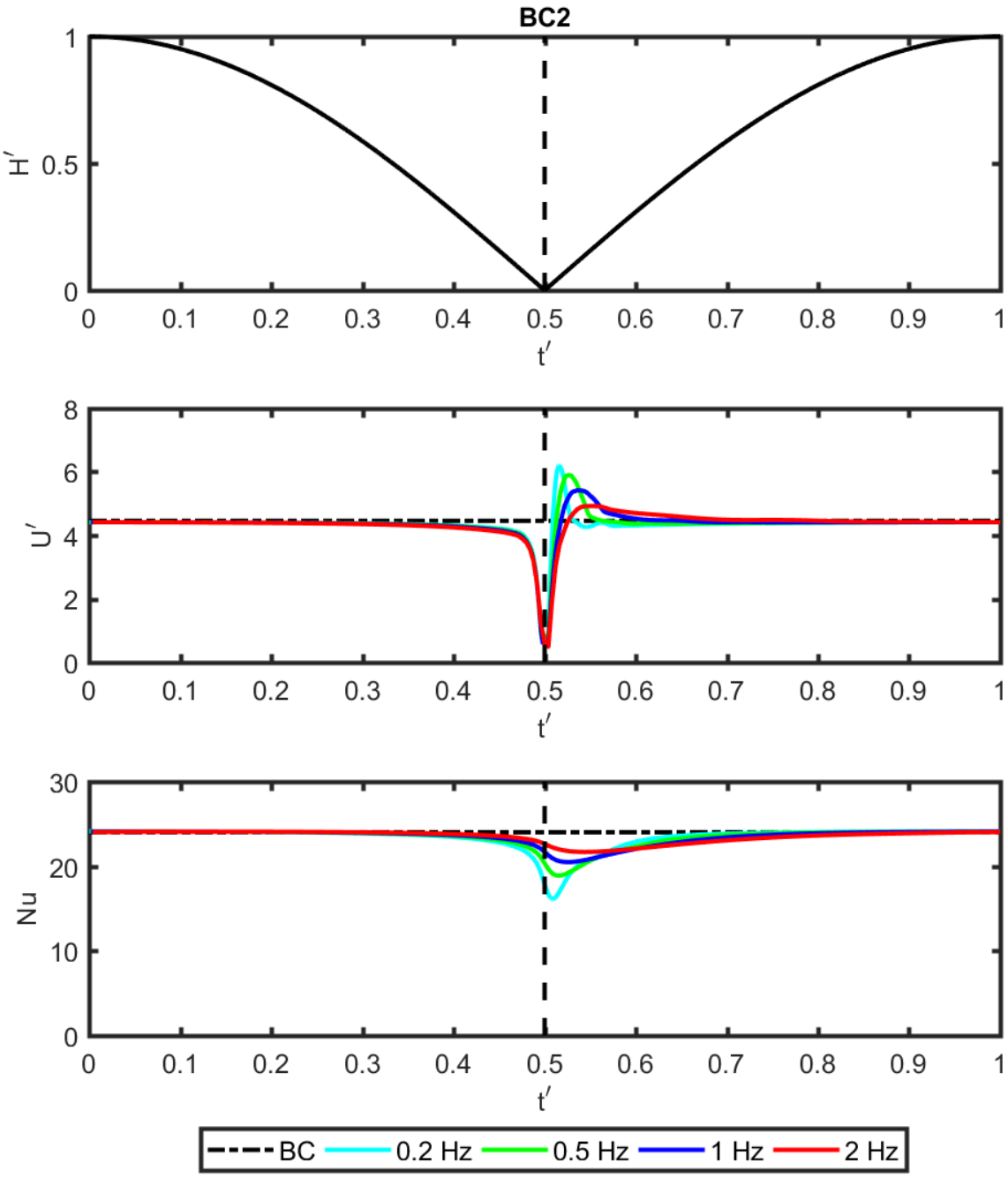

Figure 8.13: Non-dimensional magnetic field, H', velocity magnitude, U', and Nusselt number, Nu, plotted versus the time, t', for configuration (BC2).

zero and have gravitational origins. Here, the temperature field is affected by buoyancy instead of conductive heat transfer as is the case in (BG2). As the velocity magnitude is above zero the time is still sufficient enough to make small changes to the temperature profile and the peaks in Nu shift upwards and towards the left as is in (BG2). The velocity profile in Fig. 8.14 correspondents to this as does the phase lag in Nu. The phase lag for

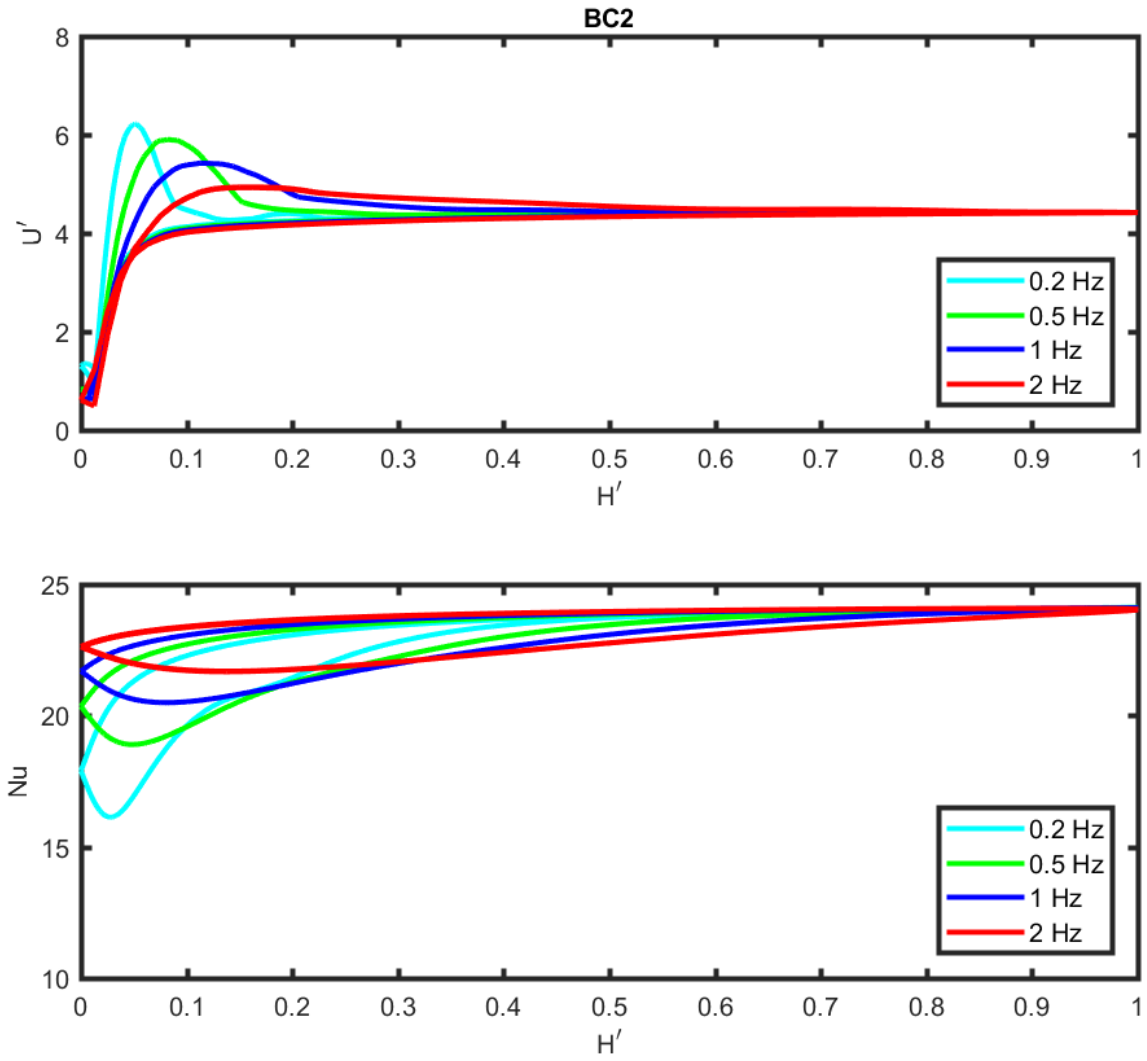

Figure 8.14: Non-dimensional velocity magnitude, U', and Nusselt number, Nu, plotted versus the magnetic field, H', for configuration (BC2).

0.2 Hz is 2.6% of the period and increase with frequency to 13.8% for 2 Hz .

8.4 Discussion

To get an indication of the varying heat transfer for each configuration the range and mean value of the Nusselt number is plotted versus the applied frequencies in Fig. 8.15 for all configurations investigated. The first configuration (BG1) shows a fairly constant mean value of Nu in the range of 20.24 to 20.74. The maximum of Nu is 22.52 and minimum 10.54 which reflect the alternating magnetic influence on the Kelvin body force. While the maximum in Nu is constant for all applied frequencies the minimum in Nu shifts from 10.54 to 17.27 when the frequency is increased. This phenomena refers to the

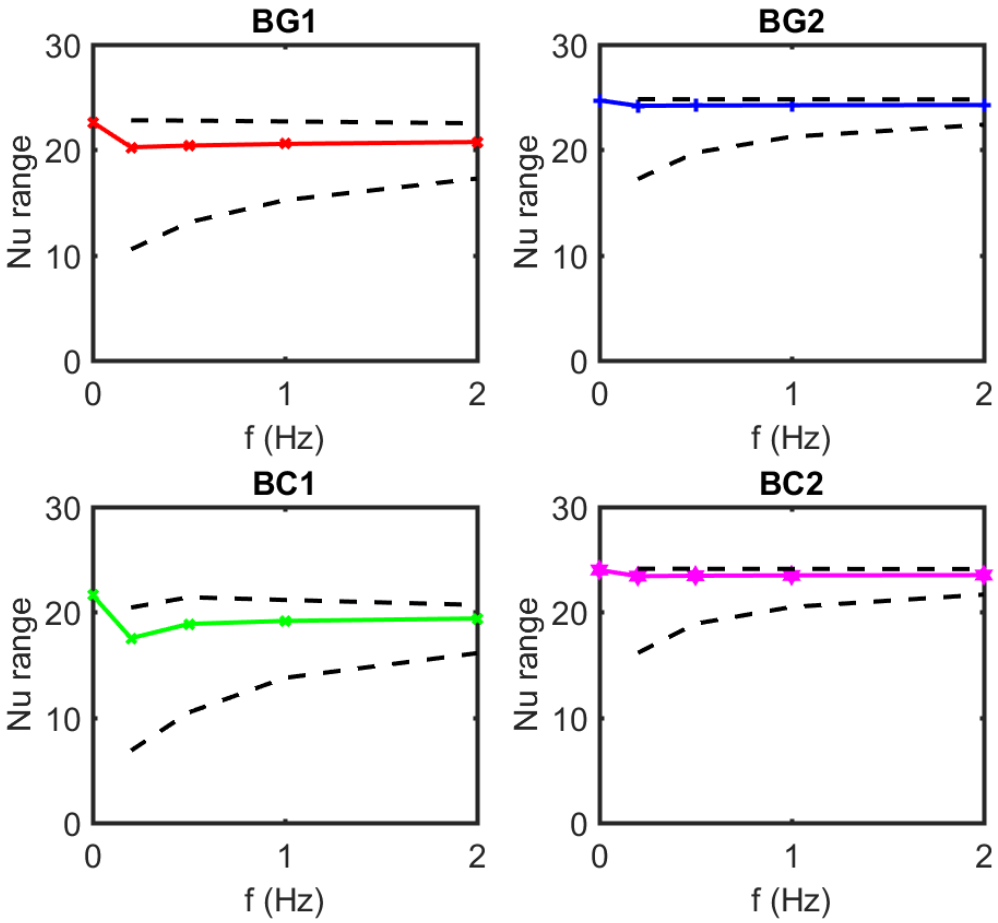

Figure 8.15: The range mean value of the Nusselt number, Nu, plotted versus the frequency, f, for each configuration.

thermal diffusivity time scale and the viscous diffusivity time scale. Here, the fluid is less magnetised for a longer time frame and the Kelvin body force is small or even absent when the magnetic field is zero. Thus, conductive heat transfer can influence the temperature field when the Kelvin body force is absent and affects thermomagnetic convection when the Kelvin body forces recovers. At higher frequencies the time frame is too short to cause significant changes in fluid's temperature as the Kelvin body force is small for a shorter time. The temperature field is therefore less affected by conduction and the minimum in Nu rises with the frequency. A higher amplitude of the magnetic field intensity such as in (BG2) magnetise the fluid to its saturation magnetisation and the mean Nu shifts upwards. While the fluid stays for a longer period magnetised as in (BG1) the time frame to cause significant changes to the temperature field is marginal resulting in a higher minimum of Nu than compared to (BG1). With an increase in frequency the same effect

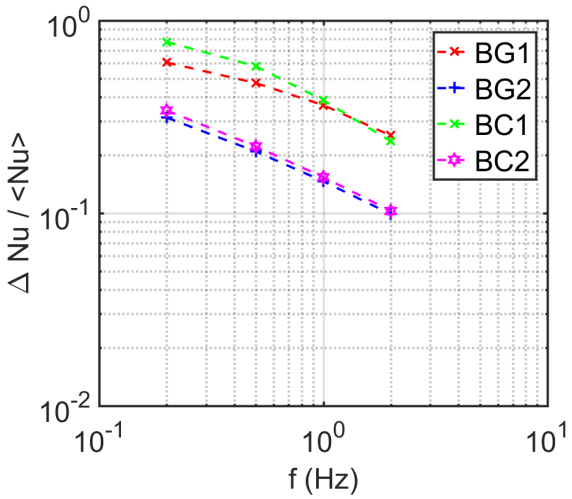

Figure 8.16: The range of Nusselt number, Nu, per mean value plotted versus the frequency, f, for each configuration.

is observed as in (BG1) and the minimum of Nu shifts upwards.

In the presence of gravity such as in case (BC1) with 0.2 Hz heat transfer is additionally influenced by buoyancy. Here, gravity opposes the Kelvin body force and is able to overtake convective heat transfer in the cavity for a short time frame rearranging the temperature distribution as seen in Fig. 8.12. This has influence on Nu as both the Kelvin body force and buoyancy compete to take the dominance within the cavity with respect to the time frame and viscous diffusivity time scale. Thus, the first decrease in Nu seen in Fig. 8.8 is followed by a peak caused by buoyancy and is followed by a second decrease when the intensity of the Kelvin body force starts suppressing buoyancy. A further increase in Nu is then observed when the Kelvin body force becomes the dominant force resulting in a lower mean value of Nu overall. By using a higher frequency the Kelvin body force is small for a shorter time and the acting buoyancy is insufficient to affect the temperate distribution significantly. Thus, a flipping convection from to thermomagnetically induced convection to a natural convection cell and back is not observed as it is for case (BC1) at 0.2 Hz. Hence, the change in temperature within the fluid's interior is only caused by the buoyancy force that acts in a short time to rearrange the temperature distribution marginally. In this case only the viscous diffusivity time scale is active. Here, the thermal diffusivity time scale is replaced by buoyancy and heat transfer is in form of natural convection that changes the temperature field marginally instead of the (BG1) and (BG2) configuration where thermal conduction is in place to change the temperature field when the Kelvin body force is small by heat conduction.

The increase in the minima of Nu refers to the time where the fluid response to the

Kelvin body force. If the time is small as it is when the frequency is high the minima increases and the temperature change is less affected by thermal conduction or buoyancy driven convection. An indication of the variation of the minima and maxima of Nu to the mean value is given by Fig. 8.16 that reproduce the shift in the range when the frequency is increased.

8.5 Summary

This section analysed thermomagnetic convection (BG1), (BG2) and combined natural and thermomangetic convection (BC1), (BC2) induced via alternating magnetic fields by numerical simulations. The alternating velocity and temperature fields were analysed in non-dimensional form using the most appropriate time scale the frequency. The heat transfer was quantified by the Nusselt number, Nu, and plotted versus the time varying magnetic field and the non-dimensional time. In summary the temperature, velocity magnitude and Nusselt number responded to the alternating intensity of the magnetic field. Here, in the absence of gravity when the Kelvin body force is small, heat transfer is in form of conduction that makes changes to the temperature distribution. The time scale was characterised by the temporal change in the spatial distribution of the temperature via heat conduction when the Kelvin body force was small and referred to the thermal diffusivity time scale. If the time was large the effect of heat conduction on the temperature distribution was significant. A second time scale was found where the temperature distribution was reconfigured to the initial structure and had its origin in the viscous diffusivity time scale. The third time scale characterises the inertial response to the magnetic fluid and was found not significantly large.

9 Conclusion

The previous chapters have analysed thermomagnetic convection in the absence and the presence of terrestrial gravity in magnetic fluids. The results, discussions and summaries provided for each study case are now concluded in this chapter and bring the theory, experimental and computational simulations together in a global context.

This study has analysed the effect of magnetic fields that varied from a constant magnetic field gradient to spatial varying alternating magnetic fields to induce magnetic convection in a mineral-oil based magnetic fluid. The physical properties of the magnetic fluid and its behaviour of a complex multiphase system was considered in theory, numerical and in experimental simulation. The computational simulations are based on a finite-element technique developed by COMSOL Multiphysics [187] a commercial software package. This package was easy able to couple the magneto-static field equations with the energy, continuity and momentum equations with or without buoyancy. The magneto-static field equations then provided the magnetic body force and were added to the governing equations. All computational analyses were carried out in a single phase mixture model. Here, the magnetic fluid was considered as a macroscopic fluid and behaves as a homogeneous magnetisable fluid where differences in particle concentration do not occur. All simulations were benchmarked using de Vahl Davis [193] benchmark solution for natural convection or validated against the experimental observations in §7.

In order to study the potential of thermomagnetic convection a natural convection model was studied first. A parametric computational model used a set of different Rayleigh numbers to provided a benchmark solution. Based on the benchmark a numerical model was developed that took the magnetic body force into account to study thermomagnetic convection. Here, the magnetic fluid was subjected to a constant magnetic field gradient that induced the convection. For this purpose a magnetic Rayleigh number was developed that represented the empirical equivalence to the conventional Rayleigh number. A comparison of each model validated the dependants of magnetic and thermal forces to induce thermomagnetic convection. It was also found that the magnetic force is stronger than buoyancy.

With use of magnetic fluids as a coolant in heat transfer applications and the sensitivity to magnetic fields convective structures of terrestrial gravity origins may influence thermomagnetic convection significantly. A joined model was developed to study thermomagnetic convection in the presence of buoyancy. A constant magnetic field gradient was used to induce magnetic convection. The intensity was set such that the magnetic effects would in some cases be the dominant factor throughout the domain and other

cases only in part of the domain. As both body forces oppose each other a transition region was found from natural convection to thermomagnetic convection. It was evident that the effective driving force could be characterised with a body force ratio, r. The ratio introduced a robust feature to evaluate the transition region where both body forces were equal. A relatively sharp transition from one to the other convection cell was found rather than an extended mixture of the magnetic fluid and was determined by the spatial structure of the applied magnetic field. The spatial extent of one of the convection cells increased at the expense of the other and refers to the applied magnetic field intensity and the fluid's temperature[17]. The start of the transition in convective structure was also observed in the Nusslet number and found as a clear minimum. Here, heat transfer reduced as the magnetic force started to become the dominate force and suppressed buoyancy, shifting the natural convection cell away from the origin of the magnetic field. When the magnetic force was intense enough to establish a second thermomagnetic convection cell that contributed to convective heat transfer the Nusselt number recovered.

Based on experimental and numerical simulations the features of thermomagnetic convection under spatial non-uniform magnetic fields was investigated in the presence of buoyancy. The aim was to give an indication of the heat transfer process of applications that use a realistic magnetic field generated e.g. by a permanent magnet. The choice of the permanent magnet was based on the field distribution and the constant remanent flux density to magnetise only a part of the fluid domain to magnetic saturation. As both buoyancy and magnetic body force are temperature dependant one objective was to explore the degree of convective heat transfer by only varying the temperature difference. The experimental and numerical model included two separate sets of temperature boundary conditions and three sets of different magnetic field distributions to conform to a more realistic experimental examination of different application geometries.

The experimentally recorded images via infrared thermogrpahy and the computational model provided corresponding temperature and flow fields. Both experiment and numerical model presented good agreement and provided the evidence of the temperature dependent magnetic body force and its correlation to buoyancy. To give an indication of the combined driving force and the effect on heat transfer a modified Rayleigh number was developed that accounted for both body forces. The heat transfer within the cavity was quantified by the Nusselt number and plotted versus the modified Rayleigh number. Results presented that an increasing temperature difference across the system leads to an increase in both forces. However, the body forces increase with different intensity. A

[17] As the magnetic fluid is considered as a macroscopic homogeneous fluid differences in particle concentration are not taken into account.

useful tool to describe and calculate the variation was introduced in the body force ratio, r. This parameter indicated an adequate quantification of the process and competition of both body forces when the temperature difference changed. In addition it was observed that the Kelvin body force can induce convection where gravity was not able to.

To give a better understanding of the heat transfer processes that involves alternating magnetic fields the response of the magnetic fluid needed to be investigated. A parametric study was carried out to investigate the effect of alternating magnetic field on thermomagnetic convection with and without buoyancy. A set of alternating frequencies was used to investigate the response of the magnetic fluid by computational simulations. All frequencies investigated alternated around a zero mean value starting from 0.5 to 2 Hz with an amplitude of 1×10^6 A/m. As Néel relaxation and Brownian motion were several orders faster than the frequencies the transient change of the magnetisation were neglected.

The observed thermomagnetic convection induced by the alternating magnetic field developed flow fields that altered with the frequency of the applied field but with varying amplitude. The time-varying thermomagnetic convection was characterised by the Nusselt number, and it was found that the heat transfer alternated with the frequency. This was reflected in the velocity magnitude that effected the temperature profile. The alternating mangetic body force and the competition between buoyancy when present cause a phase lag in the convective heat transfer that could be characterised in three time scales. The first time scale is the response of the fluid to the alternating magnetic field. The observed phase lag in the velocity field was small and had its origin in the inertial time scale due to viscous dissipation. The second time scale that affected the velocity field was the thermal diffusivity time scale. The origin of this time scale is the change of the spatial temperature distribution via heat conduction as no body force was active or to small to induce convection[18]. When the magnetic body force recovers the fluid responds to the change in the fluid temperature and rearranges the temperature distribution by a sharp increase in velocity. This change refers to the third viscous diffusivity time scale and characterises the time that is needed to establish the representative temperature field of the convective flow. Those time scale competed with each other when frequencies or amplitude of the magnetic field change in the absence or the presence of buoyancy. The effect of the competition of these time scales resulted in a lag in heat transfer that was marginal when the magnetic field intensity was higher than the fluid saturation and the frequency small.

Putting the study cases in context, the Kelvin body force is much stronger than

[18]This is the case when the Rayleigh number is below its critical value and convection does not occur.

buoyancy if the magnetic fluid is magnetised close to saturation magnetisation[19]. Second, the effect of the magnetic field intensity on natural convection of a magnetic fluid can be characterised by a force ratio if a transition region is observed. Third, the effect on heat transfer cause by the representative body force of combined convection can be quantified by a modified Rayleigh number plotted versus the Nusselt number. Unfortunately, this has its limitation for the transition region where a effective Rayleigh number cannot be developed due to two different dominant body forces. Lastly, the response of the magnetic fluid to alternating magnetic fields can be characterised by three representative time scales, the inertial time scale, thermal diffusivity time scale and viscous time scale.

The conducted studies in this thesis enables the fundamental understating and present the potential of thermomagnetic convection for the use in heat transfer applications for efficient cooling. The additional response of the magnetic fluids towards higher magnetic field intensity even if alternated enables a intelligent cooling system. Thus, the potential of cooling with magnetic fluid using magnetic forces enables a new approach of design and manufacturing. Hence, the stronger body force reduces the amount of cooling fins and cooling fluid needed for efficient cooling. In addition the arrangement and direction of magnetic fields induce convection where buoyancy was not able to. The potential of thermomagnetic convection in low-gravity environments where natural convection is not present is in addition an applicable area of efficient cooling by using magnetic fluids.

[19]This is true for the used magnetic fluid. However, the limitation of different fluid composition and volume concentration of suspended magnetic nano particles may lead to the effect that the Kelvin body force is smaller than buoyancy.

10 Future work

The experimental and numerical studies since the early and mid-60s are not numerous in the application of magnetic fluid for efficient cooling. Up until now there is still a great potential of new introduced heat transfer applications for magnetic fluids. However, detailed comparison of experiments and numerical studies are still difficult to achieve and is mostly regarded to the lack of information in the physical properties of the magnetic fluid and the complex behaviour of the two phase system. Commercially available magnetic fluids are also subjected to this limitations and in general only averaged values of the fluids composition are given. In line with this, the experiments and numerical simulations still show a good agreement.

In addition to these limitations in the fluid composition and the determination of the physical properties additional mechanism need to be considered. These are subjected to a multiphase analysis of the magnetic fluid. As the fluid is exposed to various forces that cause inter-particle and fluid-particle interactions, the effects on convection need to be investigated in more detail. This includes magneto-dissipation, thermophoresis and magnetophoresis from the Soret effect, gravitational sedimentation, magnetic agglomeration and magnetic phase separation.

In order to deal with this complex multiphase fluids further models and experiments need to be carried out to take these effects into account to study thermomagnetic convection in heat transfer applications. This includes the effect of alternating magnetic fields and the response of magnetic colloids by considering magneto-dissipation that may causes significant impacts when frequency is high.

In the context of this further investigations of magnetic fluids at higher frequency may be studied in a multiphase analysis using the fundamentals introduce in this thesis. For the application of magnetic fluids e.g. in power transformers the complex geometry, cooling channels such as fins and the high heat intensity regions between the electromagnetic coils and the core may be studied in more detail.

As the application of such fluids in heat transfer applications is limited of the life cycle of the fluid itself, magnetic phase separation and sedimentation due to particle agglomeration and gravity may be investigated further that influences convective fluid flow and heat transfer.

References

[1] S. U. S. Choi and J. A. Eastman. Enhancing thermal conductivity of fluids with nanoparticles. Technical report, Energy Technology Division and Material Science Division Argonne National Laboratory Argonne, Illinois, 1995.

[2] R. E. Rosensweig. *Ferrohydrodynamics*. Dover Books on Physics. Dover Publications, 2013.

[3] S. Odenbach. *Ferrofluids: Magnetically Controllable Fluids and Their Applications*. Springer, 2010.

[4] M. I. Shliomis. Magnetic fluids. *Sov. Phys. Usp.*, 112(3):153–169, 1974.

[5] A. Bozhko and T. Tynjälä. Influence of gravitational sedimentation of magnetic particles on ferrofluid convection in experiments and numerical simulations. *Journal of Magnetism and Magnetic Materials*, 289(0):281–284, 2005.

[6] T. Tynjälä, A. Bozhko, P. Bulychev, G. Putin, and P. Sarkomaa. On features of ferrofluid convection caused by barometrical sedimentation. *Journal of Magnetism and Magnetic Materials*, 300(1):195–8, 2006.

[7] A. Jafari, S. M. Mousavi, T. Tynjala, and P. Sarkomaa. Cfd simulation of gravitational sedimentation and clustering effects on heat transfer of nano-ferrofluid. *PIERS Proceedings*, 2009.

[8] A. Jafari, T. Tynjälä, S. M. Mousavi, and P. Sarkomaa. Cfd simulation and evaluation of controllable parameters effect on thermomagnetic convection in ferrofluids using taguchi technique. *Computers & Fluids*, 37(10):1344–1353, 2008.

[9] M. Lajvardi, J. Moghimi-Rad, I. Hadi, A. Gavili, T. Dallali Isfahani, F. Zabihi, and J. Sabbaghzadeh. Experimental investigation for enhanced ferrofluid heat transfer under magnetic field effect. *Journal of Magnetism and Magnetic Materials*, 322(21):3508–3513, 2010.

[10] S. W. Charles. Aggregation in magnetic fluids and mangetic fluid composites. *Chemical Engineering Communications*, 67(1):145–180, 1988.

[11] S. W. Charles. *Ferrofluids*, volume 594 of *Lecture Notes in Physics*, chapter The Preparation of Magnetic Fluids, pages 3–18. Springer Berlin Heidelberg, 2002.

[12] J. Smit and H. P. J. Wijn. Ferrites: Physical properties of ferri-magnetic oxides in relation to their technical aplication. *Wiley Engineering & Material Science*, page 369, 1959.

[13] W. J. Schuele and V. D. Deetscreek. Preparation, growth, and study of ultrafine ferrite particles. *Journal of Applied Physics*, 32:235, 1961.

[14] J. L. Dormann and M. Nogues. Magnetic structures in substituted ferrites. *Journal of Physics: Condensed Matter*, 2(5):1223, 1990.

[15] S. S. Papell. Low viscosity magnetic fluid obtained by the collodial suspension of magnetic particles, 1965.

[16] S. Khalafalla and G. Reimers. Magnetofluids and their manufacture, 1973.

[17] P. L. Hariani, M. Faizal, R. Marsi, and D. Setiabudidaya. Synthesis and properties of Fe_3O_4 nanoparticles by co-precipitation method to removal procion dye. *International Journal of Enviromental Science and Development*, 4(3):336–340, 2013.

[18] R. Massart. Preparation of aqueous magnetic liquids in alkaline and acidic media. *Magnetics, IEEE Transactions*, 17(2):1247 – 1248, 1981.

[19] K. J. Davies, S. Wells, and S. W. Charles. The effect of temperature and oleate adsorption on the growth of maghemite particles. *Journal of Magnetism and Magnetic Materials*, 122(1–3):24–28, 1993.

[20] A. Bee, R. Massart, and S. Neveu. Synthesis of very fine maghemite particles. *Journal of Magnetism and Magnetic Materials*, 149(1–2):6–9, 1995.

[21] M. Gobe, K. Kon-No, K. Kandori, and A. Kitahara. Preparation and characterization of monodisperse magnetite sols in wo microemulsion. *Journal of Colloid and Interface Science*, 93(1):293–295, 1983.

[22] D. S. Mathew and R.-S. Juang. An overview of the structure and magnetism of spinel ferrite nanoparticles and their synthesis in microemulsions. *Chemical Engineering Journal*, 129(1–3):51–65, 2007.

[23] J. R. Thomas. Preparation and magnetic properties of colloidal cobalt particles. *Journal of Applied Physics*, 37(7):2914, 1966.

[24] P. H. Hess and P. H. Parker. Polymers for stabilization of colloidal cobalt particles. *Journal of Applied Polymer Science*, 10(12):1097–4628, 1966.

[25] R. Mailfert and A. Martinet. Flow regimes for a magnetic suspension under a rotating magnetic field. *J. Phys. France*, 34(2-3):197–201, 1973.

[26] R. W. Chantrell, J. Popplewell, and S. Charles. Measurements of particle size distribution parameters in ferrofluids. *Magnetics, IEEE Transactions on*, 14(5):975–977, 1978.

[27] M. Kilner, S. R. Hoon, D. B. Lambrick, J. Potton, and B. K. Tanner. Preparation and properties of metallic iron ferrofluids. *Magnetics, IEEE Transactions on*, 20(5):1735–1737, 1984.

[28] E. Papirer, P. Horny, H. Balard, R. Anthore, C. Petipas, and A. Martinet. The preparation of a ferrofluid by decomposition of dicobalt octacarbonyl: I. experimental parameters. *Journal of Colloid and Interface Science*, 94(1):207–219, 1983.

[29] E. Papirer, P. Horny, H. Balard, R. Anthore, C. Petipas, and A. Martinet. The preparation of a ferrofluid by decomposition of dicobalt octacarbonyl: II. nucleation and growth of particles. *Journal of Colloid and Interface Science*, 90:220–228, 1983.

[30] S. R. Hoon, M. Kilner, G. J. Russell, and B. K. Tanner. Preparation and properties of nickel ferrofluids. *Journal of Magnetism and Magnetic Materials*, 39(1–2):107–110, 1983.

[31] D. B. Lambrick, N. Mason, S. R. Hoon, and M. Kilner. Preparation and properties of ni-fe magnetic fluids. *Journal of Magnetism and Magnetic Materials*, 65(2–3):257–260, 1987.

[32] I. Nakatani and T. Furubayashi. Iron-nitride magnetic fluids prepared by plasma cvd technique and their magnetic properties. *Journal of Magnetism and Magnetic Materials*, 85(1–3):11–13, 1990.

[33] I. Nakatani, M. Hijikata, and K. Ozawa. Iron-nitride magnetic fluids prepared by vapor-liquid reaction and their magnetic properties. *Journal of Magnetism and Magnetic Materials*, 122(1–3):10–14, 1993.

[34] J. A. Lopez-Perez, M. A. Lopez-Quintela, J. Mira, and J. Rivas. Preparation of magnetic fluids with particles obtained in microemulsions. *Magnetics, IEEE Transactions on*, 33(5):4359–4362, 1997.

[35] I. Capek. Preparation of metal nanoparticles in water-in-oil (w/o) microemulsions. *Advances in Colloid and Interface Science*, 110(1–2):49–74, 2004.

[36] M. A. López-Quintela. Synthesis of nanomaterials in microemulsions: formation mechanisms and growth control. *Current Opinion in Colloid & Interface Science*, 8(2):137–144, 2003.

[37] A. L. Oppegard, F. J. Darnell, and H. C. Miller. Magnetic properties of single-domain iron and iron-cobalt particles prepared by borohydride reduction. *Journal of Applied Physics*, 32(3):S184, 1961.

[38] G. Akashi and M. Fujuyama. Process for the production of magnetic substances, 1969.

[39] S. Harada, T. Yamanashi, and M. Ugaji. Preparation and magnetic properties of cobalt alloy particles. *Magnetics, IEEE Transactions on*, 8(3):468–470, 1972.

[40] S. W. Charles and B. Issari. Preparation and properties of small acicular particles of cobalt. *Journal of Magnetism and Magnetic Materials*, 54–57, Part 2(0):743–744, 1986.

[41] P. C. Scholten. Some material problems in magnetic fluids. *Chemical Engineering Communications*, 67(1):331–340, 1988.

[42] J. E. Wyman. Ferrofluid composition and method of making the same, 1984.

[43] W. R. Bottenberg and M. S. Chagnon. Low vapor-pressure ferrofluids and methode of making same, 1982.

[44] M. S. Chagnon. Stable ferrofluid compositions and method of making same, 1982.

[45] J.-C. Bacri, R. Perzynski, D. Salin, V. Cabuil, and R. Massart. Ionic ferrofluids: A crossing of chemistry and physics. *Journal of Magnetism and Magnetic Materials*, 85(1–3):27–32, 1990.

[46] R. W. Chantrell, A. Bradbury, J. Popplewell, and S. W. Charles. Agglomerate formation in a magnetic fluid. *Journal of Applied Physics*, 53(3):2742, 1982.

[47] A. F. Pshenichnikov. Equilibrium magnetization of concentrated ferrofluids. *Journal of Magnetism and Magnetic Materials*, 145:319–326, 1994.

[48] A. F. Pshenichnikov and V. V. Mekhononshin. Equilibrium magnetization and microstructure of the system of superparamagnetic interacting particles: numerical simulation. *Journal of Magnetism and Magnetic Materials*, 213:357–369, 1999.

[49] B. A. Finlayson. Convective instability of ferromagnetic fluids. *J. Fluid Mech.*, 40(4):753–767, 1970.

[50] I. Nkurikiyimfura and Z. Pan Y. Wang and. Heat transfer enhancement by magnetic nanofluids – A review. *Renewable and Sustainable Energy Reviews*, 21:548–561, 2620 2013.

[51] J. Frenkel. *The kinetic theory of liquids*. Dover Publications, New York 1955.

[52] E. Blums, A. Cebers, and M. M. Maiorov. *Magnetic Fluids*. Walter de Gruyter & Co., Berlin, 1997.

[53] Y. Martsenyuk, L. Raikher, and M. I. Shliomis. On the kinetics of magnetization 2625 of suspensions of ferromagnetic particles. *Sov. Phys. JETP*, 38(2):413–6, 1974.

[54] L. Néel. Le champ coercitif d'une poudre ferromagnetique cubique a grains anisotropes. *C. R. Acad. Sci. Paris*, 224(664):1550–1, 1947.

[55] L. Néel. Effect of thermal fluctuations on the magnetisation of small particles. *Rev. Mod. Phys.*, 25(293), 1953.

2630 [56] T. K. McNab, Fox R. A., and J. F. Boyle. Some magnetic properties of magnetite (Fe_3O_4) microcrystals. *Journal of Applied Physics*, 39(12):5703–11, 1968.

[57] S. Soleimani, M. Sheikholeslami, D. D. Ganji, and M. Gorji-Bandpay. Natural convection heat transfer in a nanofluid filled semi-annulus enclosure. *International Communications in Heat and Mass Transfer*, 39(4):565–574, 2012.

2635 [58] H. Aminfar, M. Mohammadpourfard, and Y. Narmani Kahnamouei. A 3D numerical simulation of mixed convection of a magnetic nanofluid in the presence of non-uniform magnetic field in a vertical tube using two phase mixture model. *Journal of Magnetism and Magnetic Materials*, 323(15):1963–1972, 2011.

[59] H. Aminfar, M. Mohammadpourfard, and S. Ahangar Zonouzi. Numerical study 2640 of the ferrofluid flow and heat transfer through a rectangular duct in the presence of a non-uniform transverse magnetic field. *Journal of Magnetism and Magnetic Materials*, 327:31–42, 2013.

[60] H. Aminfar, M. Mohammadpourfard, and Y. Narmani Kahnamouei. Numerical study of magnetic field effects on the mixed convection of a magnetic nanofluid in 2645 a curved tube. *International Journal of Mechanical Sciences*, 78:81–90, 2014.

[61] B. C. Pak and Y. I. Cho. Hydrodynamic and Heat Transfer Study of Dispersed Fluids With Submicron Metallic Oxide Particles. *Experimental Heat Transfer*, 11(2):151–170, 1998.

[62] A. A. G. Nnanna, T. Fistrovich, K. Malinski, and S. U. S. Choi. Thermal Transport Phenomena in Buoyancy-Driven Nanofluids. *Proceedings of ASME IMEC*, 4:571–578, 2004.

[63] Y. Xuan and W. Roetzel. Conceptions for heat transfer correlation of nanofluids. *International Journal of Heat and Mass Transfer*, 43(19):3701–3707, 2000.

[64] J. A. Eastman, S. R. Phillpot, S. U. S. Choi, and P. Keblinski. Thermal Transport in Nanofluids. *Annu. Rev. Mater. Res.*, 34:219–246, 2004.

[65] S. J. Palm, G. Roy, and C. T. Nguyen. Heat transfer enhancement with the use of nanofluids in radial flow cooling systems considering temperature-dependent properties. *Applied Thermal Engineering*, 26(17-18):2209–2218, 2006.

[66] K. Khanafer, K. Vafai, and M. Lightstone. Buoyancy-driven heat transfer enhancement in a two-dimensional enclosure utilizing nanofluids. *International Journal of Heat and Mass Transfer*, 46(19):3639–3653, 2003.

[67] J. Philip and P. D. Shima. Thermal properties of nanofluids. *Advances in Colloid and Interface Science*, 183–184(0):30–45, 2012.

[68] W.-G. Früh. Heat transfer enhancement by thermomagnetic convection. In P Jansens, A. Stankiewicz, and A. Green, editors, *Sustainable (Bio)Chemical Process Technology*, pages 47–56, Cranfield, 2005. BHR Group Ltd.

[69] D. A. G. Bruggeman. Berechnung Verschiedener Physikalischer Konstanten von Heterogenen Substanzen, I. Dielektrizitatskonstanten und Leitfahigkeiten der Mischkorper aus Isotropen Substanzen. *Annalen der Physik*, 5(24):636–679, 1935.

[70] C. H. Chon, K. D. Kihm, S. P. Lee, and S. U. S. Choi. Empirical correlation finding the role of temperature and particle size for nanofluid (Al_2O_3) thermal conductivity enhancement. *Applied Physics Letters*, 87(15):1–3, 2005.

[71] R. L. Hamilton and O. K. Crosser. Thermal Conductivity of Heterogeneous Two-Com Ponent Systems. *I & EC Fundumentals*, 1(3):187–191, 1959.

[72] S. P. Jang and S. U. S. Choi. Role of Brownian motion in the enhanced thermal conductivity of nanofluids. *Applied Physics Letters*, 84(21):4316–4318, 2004.

[73] J. Koo and C. Kleinstreuer. A new thermal conductivity model for nanofluids. *Journal of Nanoparticle Research*, 6(6):577–588, 2004.

[74] J. C. Maxwell-Garnett. Colours in metal glasses and in metallic film. *Philos. Trans. Roy. Soc.*, A 203:385–420, 1904.

[75] F. J. Wasp. *Solid-liquid slurry pipeline transportation*. Trans. Tech., 1977.

[76] A. Einstein. On the movement of small particles suspended in a stationary liquid dedemand by the molecular kinetic theory of heat. *Annalen der Physik*, 17(549-560), 1905.

[77] A. Einstein. *Investigation of the theory of the Brownian movement*. Dover Publications, New York, 1956.

[78] R. E. Rosensweig, J. W. Nestor, and R. S. Timmins. Ferrohydrodynamic fluids for direct conversion of heat energy. *Mater. Assoc. Energy Convers. Proc. Symp. AIChE-I Chem. Eng. Ser. 5*, pages 104–18, 1965.

[79] J. P. McTague. Magnetoviscousity of magnetic colloids. *Journal of Chemical Physics*, 51(1):133–36, January 1969.

[80] W. F. Hall and S. N. Busenberg. Viscosity of magnetic suspensions. *Journal of Chemical Physics*, 51(1):137–144, January 1969.

[81] S. Odenbach and S. Thurm. *Ferrofluids*, chapter Magnetoviscous Effects in Ferrofluids, pages 185–201. Springer -Verlag Berlin Heidelberg, 2002.

[82] M. I. Shliomis. Effective viscosity of magnetic suspensions. *Sov. Phys. JETP*, 34(6):1291–4, 1972.

[83] G. K. Batchelor. The effect of Brownian motion on the bulk stress in a suspension of spherical particles. *Journal of Fluid Mechanics*, 83:97–117, 11 1977.

[84] H. C. Brinkman. The Viscosity of Concentrated Suspensions and Solutions. *Journal of Chemical Physics*, 20(4):571–581, 1952.

[85] L. A. Dávalos-Orozco and L. F. Del Castillo. Hydrodynamic behavior of suspensions of polar particles. In P Somasundara, editor, *Encyclopedia of Surface and Colloid Science*, chapter Hydrodynam, pages 353–375. Marcel Denkker, New York, 2003.

[86] A. L. Graham. On the viscosity of suspensions of solid spheres. *Applied Scientific Research*, 37(3):275–286, 1981.

[87] S. P. Jang, J. H. Lee, K. S. Hwang, and S. U. S. Choi. Particle concentration and tube size dependence of viscosities of Al_2O_3 -water nanofluids flowing through micro- and minitubes. *Applied Physics Letters*, 91(24):1–4, 2007.

[88] S. El Bécaye Maiga, S. J. Palm, C. T. Nguyen, G. Roy, and N. Galanis. Heat transfer enhancement by using nanofluids in forced convection flows. *International Journal of Heat and Fluid Flow*, 26(4 SPEC. ISS.):530–546, 2005.

[89] N. Masoumi, N. Sohrabi, and A. Behzadmehr. A new model for calculating the effective viscosity of nanofluids. *Journal of Physics D: Applied Physics*, 42(5):055501, 2009.

[90] C. T. Nguyen, F. Desgranges, N. Galanis, G. Roy, T. Maré, S. Boucher, and H. Angue Mintsa. Viscosity data for Al_2O_3-water nanofluid-hysteresis: is heat transfer enhancement using nanofluids reliable? *International Journal of Thermal Sciences*, 47(2):103–111, 2008.

[91] R. Ganguly, S. Sen, and I. K. Puri. Heat transfer augmentation using a magnetic fluid under the influence of a line dipole. *Journal of Magnetism and Magnetic Materials*, 271:63–73, 2004.

[92] A. Lange and S. Odenbach. Thermomagnetic convection in magnetic fluids subjected to spatially modulated magnetic fields. *Physics Procedia*, 9:171–175, 2010.

[93] M. Heckert, L. Sprenger, A. Lange, and S. Odenbach. Experimental determination of the critical Rayleigh number for thermomagnetic convection with focus on fluid composition. *Journal of Magnetism and Magnetic Materials*, 381:337–343, 2015.

[94] L. Schwab, U. Hildebrandt, and K. Stierstadt. Magnetic Bénard convection. *Journal of Magnetism and Magnetic Materials*, 39:113–114, 1983.

[95] L. Schwab and K. Stierstadt. Field-induced wavevector-selection by magnetic Bénard-convection. *Journal of Magnetism and Magnetic Materials*, 65(2):315 – 316, 1987.

[96] P. J. Stiles and M. Kagan. Thermoconvective instability of a horizontal layer of ferrofluid in a strong vertical magnetic field. *Journal of Magnetism and Magnetic Materials*, 85:196–198, 1990.

[97] P. J. Blennerhassett, F. Lin, and P. J. Stiles. Heat transfer through strongly magnetized ferrofluids. *Proceedings of the Royal Society A: Mathematical, Physical and Engineering Sciences*, 433(1):165–177, 1991.

[98] P. J. Stiles and M. Kagan. Thermoconvective instability of a ferrofluid in a strong magnetic field. *Journal of Colloid and Interface Science*, 134:435–448, 1990.

[99] A. Lange. Thermal convection of magnetic fluids in a cylindrical geometry. *Journal of Magnetism and Magnetic Materials*, 252:194–196, 2002.

[100] A. Lange. Kelvin force and thermal convection in a layer of magnetic fluid. *Journal of Magnetism and Magnetic Materials*, 241:327–329, 2002.

[101] M. S. Krakov and I. V. Nikiforov. To the influence of uniform magnetic field on thermomagnetic convection in square cavity. *Journal of Magnetism and Magnetic Materials*, 252:209–211, 2002.

[102] M. S. Krakov, I. V. Nikiforov, and S. Kamiyama. Three-dimensional thermomagnetic convection in a cubic cavity in the presence of an external uniform magnetic field. *Magnetohydrodynamics*, 40:285–296, 2004.

[103] M. S. Krakov, I. V. Nikiforov, and A. G. Reks. Influence of the uniform magnetic field on natural convection in cubic enclosure: experiment and numerical simulation. *Journal of Magnetism and Magnetic Materials*, 289:272–274, 2005.

[104] H. Yamaguchi, I. Kobori, Y. Uehata, and K. Shimada. Natural convection of magnetic fluid in a rectangular box. *Journal of Magnetism and Magnetic Materials*, 201:264–267, 1998.

[105] H. Yamaguchi, X.-D. Niu, X.-R. Zhang, and K. Yoshikawa. Experimental and numerical investigation of natural convection of magnetic fluids in a cubic cavity. *Journal of Magnetism and Magnetic Materials*, 321:3665–3670, 2009.

[106] H. Yamaguchi, X.-R. Zhang, X.-D. Niu, and K. Yoshikawa. Thermomagnetic natural convection of thermo-sensitive magnetic fluid in cubic cavity with heat generation object inside. *Journal of Magnetism and Magnetic Materials*, 322:698–704, 1010.

[107] T. Bednarz, E. Fornalik, T. Tagawa, H. Ozoe, and Janusz S. Szmyd. Experimental and numerical analyses of magnetic convection of paramagnetic fluid in a cube heated and cooled from opposing verticals walls. *International Journal of Thermal Sciences*, 44(10):933–43, 2005.

[108] T. Bednarz, E. Fornalik, and T. Tagawa. Convection of paramagnetic fluid in a cube heated and cooled from side walls and placed below a superconducting magnet - comparison between experiment. *Thermal Science and Engineering*, 14(4):107–14, 2006.

[109] T. Bednarz, E. Fornalik, H. Ozoe, J. S. Szmyd, J. C. Patterson, and C. Lei. Influence of a horizontal magnetic field on the natural convection of paramagnetic fluid in a cube heated and cooled from two vertical side walls. *International Journal of Thermal Sciences*, 47(6):668–79, 2008.

[110] T. P. Bednarz, C. Lei, J. C. Patterson, and H. Ozoe. Effects of a transverse, horizontal magnetic field on natural convection of a paramagnetic fluid in a cube. *International Journal of Thermal Sciences*, 48(1):26–33, 2009.

[111] T. Bednarz, C. Lei, J. C. Patterson, and H. Ozoe. Suppressing Rayleigh-Bénard convection in a cube using a strong magnetic field - Experimental heat transfer rate measurements and flow visualization. *International Communications in Heat and Mass Transfer*, 36(2):97–102, 2009.

[112] T. P. Bednarz, J. C. Patterson, C. Lei, and H. Ozoe. Enhancing natural convection in a cube using a strong magnetic field - Experimental heat transfer rate measurements and flow visualization. *International Communications in Heat and Mass Transfer*, 36(8):781–6, 2009.

[113] C.-W. Wen and W.-P. Shu. Natural convection of magnetic fluid in a rectangular Hele-Shaw cell. *Journal of Magnetism and Magnetic Materials*, 289:299–302, 2005.

[114] C.-W. Wen and W.-P. Shu. Natural convection of magnetic fluid in a rectangular Hele-Shaw cell of different aspect ratios. *Physics Procedia*, 9:181–185, 2010. 12th International Conference on Magnetic Fluids ICMF12, 1 - 5 Aug 2010, Sendai, Japan.

[115] E. Fornalik, P. Filar, T. Tagawa, H. Ozoe, and J. S. Szmyd. Experimental study on the magnetic convection in a vertical cylinder. *Experimental Thermal and Fluid Science*, 29(8):971–980, 2005.

[116] E. Fornalik, P. Filar, T. Tagawa, H. Ozoe, and J. S. Szmyd. Effect of a magnetic field on the convection of paramagnetic fluid in unstable and stable thermosyphon-like configurations. *International Journal of Heat and Mass Transfer*, 49(15-16):2642–2651, 2006.

[117] A. Bozhko and G. Putin. Heat transfer and flow patterns in ferrofluid convection. *Magnetohydrodynamics*, 39(2):147–168, 2003.

[118] A. Bozhko, G. Putin, T. Tynjälä, M. Dabagh Meshin, and P. Jalali. On pattern formation in ferrocolloid convection. *Journal of Physics: Conference Series*, 64:012008, 2007.

[119] A. A. Bozhko, G. F. Putin, and T. Tynja. Experimental and numerical investigation of wave ferrofluid convection. *Journal of Magnetism and Magnetic Materials*, 316:433–435, 2007.

[120] A. Jafari, T. Tynjälä, S. M. Mousavi, and P. Sarkomaa. Simulation of heat transfer in a ferrofluid using computational fluid dynamics technique. *International Journal of Heat and Fluid Flow*, 29(4):1197–1202, 2008.

[121] T. Völker, E. Blums, and S. Odenbach. Determination of the Soret coefficient of magnetic particles in a ferrofluid from the steady and unsteady part of the seperation curve. *International Journal of Heat and Mass Transfer*, 47:4315–25, 2004.

[122] M. I. Shliomis and B. L. Smorodin. Convective instability of magnetized ferrofluid. *Journal of Magnetism and Magnetic Materials*, 252:197–202, 2002.

[123] M. S. Krakov and I. V. Nikiforov. Thermomagnetic convection in a porous enclosure in the presence of outer uniform magnetic field. *Journal of Magnetism and Magnetic Materials*, 289:278–280, 2005.

[124] X.-R. Zhang, L.-C. Jin, X.-D. Niu, and H. Yamaguchi. Lattice Boltzmann simulation for magnetic fluids in porous medium. *Physics Procedia*, 9(2):162–166, 2010.

[125] L. Jin, X. Zhang, and X. Niu. Lattice Boltzmann simulation for temperature-sensitive magnetic fluids in a porous square cavity. *Journal of Magnetism and Magnetic Materials*, 324(1):44–51, 2012.

[126] L. Jin and X.-R. Zhang. Analysis of temperature-sensitive magnetic fluids in a porous square cavity depending on different porousity and Darcy number. *Applied Thermal Engineering*, 50:1–11, 2013.

[127] T. Tagawa, R. Shigemitsu, and H. Ozoe. Magnetizing force modeled and numerically solved for natural convection of air in a cubic enclosure: Effect of the direction of the magnetic field. *International Journal of Heat and Mass Transfer*, 45(2):267–277, 2001.

[128] T. Tagawa, A. Ujihara, and H. Ozoe. Numerical computation for Rayleigh-Bénard convection of water in a magnetic field. *International Journal of Heat and Mass Transfer*, 46(21):4097–4104, 2003.

[129] R. A. Curtis. Flows and wave propagation in ferrofluids. *Physics of Fluids*, 14(10):2096–2102, 1971.

[130] D. P. Lalas and S. Carmi. Thermoconvective stability of ferrofluids. *Physics of Fluids*, 14(2):436–438, 1971.

[131] T.-C. Jue. Analysis of combined thermal and magnetic convection ferrofluid flow in a cavity. *International Journal in Heat and Mass Transfer*, 33:846–852, 2006.

[132] C. Tangthieng, B. A. Finlayson, J. Maulbetsch, and T. Cader. Heat transfer enhancement in ferrofluids subjected to steady magnetic fields. *Journal of Magnetism and Magnetic Materials*, 201(1-3):252–255, 1999.

[133] B. M. Berkovsky, V. E. Fertman, V. K. Polevikov, and S. V. Isaev. Heat transfer across vertical ferrofluid layers. *International Journal of Heat and Mass Transfer*, 19:981–986, 1976.

[134] T. Sawada, H. Kikura, and T. Tanahashi. Visualization of wall temperature distribution caused by natural convection in a cubic enclosure. *International Journal of Applied Electromagnetics in Materials*, 4:329–335, 1994.

[135] S. M. Snyder, T. Cader, and B. A. Finlayson. Finite element model of magnetoconvection of a ferrofluid. *Journal of Magnetism and Magnetic Materials*, 262:269–279, 2003.

[136] A. Bouhrour and D. Kalache. Thermomagnetic convection of a magnetic nanofluid influenced by a magnetic field. *Thermal Science*, pages 1–12, 2015.

[137] S. Odenbach. Microgravity research as a tool for the investigation of effects in magnetic Fluids. *Journal of Magnetism and Magnetic Materials*, 201:149–154, 1999.

[138] S. Odenbach. Microgravity experiments on thermomagnetic convection in magnetic fluids. *Journal of Magnetism and Magnetic Materials*, 149:155–157, 1995.

[139] R. Ganguly, S. Sen, and I. K. Puri. Thermomagnetic convection in a square enclosure using a line dipole. *Physics of Fluids*, 16(7):2228–2236, July 2004.

[140] A. Mukhopadhyay, R. Ganguly, S. Sen, and I. K. Puri. A scaling analysis to characterize thermomagnetic convection. *International Journal of Heat and Mass Transfer*, 48:3485–3492, 2005.

[141] S. Banerjee, A. Mukhopadhyay, S. sen, and R. Ganguly. Effects of the dipole position on thermomagnetic convection in a locally heated shallow enclosure: Thermodynamic and transport analysis. *Numerical Heat Transfer, Part A*, 57:496–519, 2010.

[142] M. Ashouri, B. Ebrahimi, M. B. Shafii, M. H. Saidi, and M. S. Saidi. Correlation for Nusselt number in pure magnetic convection ferrofluid flow in a square cavity by a numerical investigation. *Journal of Magnetism and Magnetic Materials*, 322(22):3607–3613, 2010.

[143] W.-G. Früh. Using magnetic fluids to simulate convection in a central force field in the laboratory. *Nonlinear Processes in Geophysics*, 12:877–889, 2005.

[144] D. Zablockis, V. Frishfelds, and E. Blums. Numerical investigation of thermomagnetic convection in a heated cylinder under the magnetic field of a solenoid. *Journal of Physics: Condensed Matter*, 20(20):204134, 2008.

[145] D. Zablotsky, A. Mezulis, and E. Blums. Surface cooling based on the thermomagnetic convection: Numerical simulation and experiment. *International Journal of Heat and Mass Transfer*, 52(23-24):5302–5308, 2009.

[146] E. Blums, A. Mezulis, and G. Kronkalns. Magnetoconvective heat transfer from a cylinder under the influence of a nonuniform magnetic field. *Journal of Physics: Condensed Matter*, 20(20):204128, 2008.

[147] T. Tynjälä and J. Ritvanen. Simulations of thermo-magnetic convection in an annulus between two concentric cylinders. *Indian Journal of Engineering and Materials Sciences*, 11(4):283–288, 2004.

[148] C. M. Chang, W. T. Cheng, W. J. Liu, H. W. Cheng, C. E. Huang, and S. W. Du. Thermal flow of fluid with magnetic particles in the presence of magnetic field. *International Communications in Heat and Mass Transfer*, 2010.

[149] M. Sheikholeslami and M. Gorji-Bandpy. Free convection of ferrofluid in a cavity heated from below in the presence of an external magnetic field. *Powder Technology*, 256:490–498, 2014.

[150] G. H. R. Kefayati. Lattice Boltzmann simulation of natural convection kerosene / cobalt ferrofluid. *Iranian Journal of Science and Technology, Transactions of Mechanical Engineering*, 37:107–118, 2013.

[151] G. H. R. Kefayati. Natural convection of ferrofluid in a linearly heated cavity utilizing LBM. *Journal of Molecular Liquids*, 191:1–9, 2014.

[152] G. H. R. Kefayati. Simulation of Ferrofluid Heat Dissipation Effect on Natural Convection at an Inclined Cavity Filled with Kerosene / Cobalt Utilizing the Lattice Boltzm. *Numerical Heat Transfer , Part A : Applications An International Journal of Computation and Methodology*, 7782(August 2016), 2014.

[153] F. Selimefendigil, H. F. Öztop, and K. Al-salem. Natural convection of ferro fluids in partially heated square enclosures. *Journal of Magnetism and Magnetic Materials*, 372:122–133, 2014.

[154] F. Selimefendigil and H. F. Öztop. Numerical Study and POD-Based Prediction of Natural Convection in a Ferrofluids - Filled Triangular Cavity with Generalized Neural Networks. *Numerical Heat Transfer , Part A : Applications An International Journal of Computation and Methodology*, 7782(August 2016):1136–1161, 2015.

[155] J. Qi, N. I. Wakayama, and A. Yabe. Magnetic control of thermal convection in electrically non-conducting or low-conducting paramagnetic fluids. *International Journal of Heat and Mass Transfer*, 44(16):3043–3052, 2001.

[156] L. B. Wang and N. I. Wakayama. Control of natural convection in non- and low-conducting diamagnetic fluids in a cubical enclosure using inhomogeneous magnetic fields with different directions. *Chemical Engineering Science*, 57(11):1867–1876, 2002.

[157] T. Strek and H. Jopek. Computer simulation of heat transfer through a ferrofluid. *physica status solidi (b)*, 1037(3):1027–1037, 2007.

[158] T. Strek. Finite element simulation of heat transfer in ferrofluid. *Modelling and Simulation, Giuseppe Petrone and Giuliano Cammarata (Ed.), InTech,*, page 320, 2008.

[159] E. Aursand, M. A. Gjennestad, K. Yngve, and H. Lund. Potential of enhancing a natural convection loop with a thermomagnetically pumped ferro fluid. *Journal of Magnetism and Magnetic Materials*, 417:148–159, 2016.

[160] Z. Fang, R. O. Handley, Y. Liu, and M. Yang. FEA Simulation of Passive Ferrofluid Cooling Systems. *Proceedings of the COMSOL Conference 2010 Boston*, pages 1–4, 2010.

[161] A. Ghofrani, M. H. Dibaei, A. Hakim Sima, and M. B. Shafii. Experimental investigation on laminar forced convection heat transfer of ferrofluids under an alternating magnetic field. *Experimental Thermal and Fluid Science*, 49:193–200, 2013.

[162] M. Goharkhah and M. Ashjaee. Effect of an alternating nonuniform magnetic field on ferrofluid flow and heat transfer in a channel. *Journal of Magnetism and Magnetic Materials*, 362:80–89, 2014.

[163] M. Ghasemian, Z. Najafian Ashrafi, M. Goharkhah, and M. Ashjaee. Heat transfer characteristics of Fe_3O_4 ferrofluid flowing in a mini channel under constant and alternating magnetic fields. *Journal of Magnetism and Magnetic Materials*, 381:158–167, 2015.

[164] M. Goharkhah, A. Salarian, M. Ashjaee, and M. Shahabadi. Convective heat transfer characteristics of magnetite nanofluid under the influence of constant and alternating magnetic field. *Powder Technology*, 274:258–267, 2015.

[165] A. Shahsavar, M. Saghafian, M. R. Salimpour, and M. B. Shafii. Experimental investigation on laminar forced convective heat transfer of ferrofluid loaded with carbon nanotubes under constant and alternating magnetic fields. *Experimental Thermal and Fluid Science*, 76:1–11, 2016.

[166] H. R. Goshayeshi, M. Goodarzi, M. R. Safaei, and M. Dahari. Experimental study on the effect of inclination angle on heat transfer enhancement of a ferrofluid in a closed loop oscillating heat pipe under magnetic field. *Experimental Thermal and Fluid Science*, 74:265–270, 2016.

[167] M. Goharkhah, M. Ashjaee, and M. Shahabadi. Experimental investigation on convective heat transfer and hydrodynamic characteristics of magnetite nanofluid under the influence of an alternating magnetic field. *International Journal of Thermal Sciences*, 99:113–124, 2016.

[168] P. Kaloni and J. Lou. Convective instability of magnetic fluids under alternating magnetic fields. *Physical Review E*, 71(6):066311, 2005.

[169] A. V. Belyaev and B. L. Smorodin. Convection of a Ferrofluid in an alternating magnetic field. *Journal of Applied Mechanics and Technical Physics*, 50(4):558–565, 2009.

[170] K. H. Kim and J. M. Hyun. Buoyant convection in a cubical enclosure under time-periodic magnetizing force. *International Journal of Heat and Mass Transfer*, 47(24):5211–5218, 2004.

[171] D. G. Kang and J. M. Hyun. Buoyant convection in an enclosure under time-periodic magnetizing force. *International Journal of Heat and Mass Transfer*, 50(3-4):605–615, 2007.

[172] J. Gastelurrutia, J. C. Ramos, G. S. Larraona, A. Rivas, J. Izagirre, and L. del Rao. Numerical modelling of natural convection of oil inside distribution transformers. *Applied Thermal Engineering*, 31(4):493–505, 2011.

[173] J. Gastelurrutia, J. C. Ramos, A. Rivas, G. S. Larraona, J. Izagirre, and L. del Rao. Zonal thermal model of distribution transformer cooling. *Applied Thermal Engineering*, 31:4024–4035, 2011.

[174] J.-. Mufuta and E. van den Bulck. Modelling of the mixed convection in the windings of a disc-type power transformer. *Applied Thermal Engineering*, 20(5):417–437, 2000.

[175] N. El. Wakil, N. Chereches, and J. Padet. Numerical study of heat transfer and fluid flow in a power transformer. *International Journal of Thermal Sciences*, 45:615–626, 2006.

[176] J. Zhang, X. Li, and M. Vance. Experiments and modeling of heat transfer in oil transformer winding with zigzag cooling ducts. *Applied Thermal Engineering*, 28(1):36–48, 2008.

[177] A. M. Morega, L. Pislaru-Danescu, V. Stoica, F. Nouras, and F. D. Stoian. A Novel, Ferrofluid-Cooled Transformer. Electromagnetic Field and Heat Transfer by Numerical Simulation. In *International Coference on Optimization of Electrical and Electronic Equipment*, pages 140–146, 2010.

[178] A. M. Morega, M. Morega, and J. B. Dumitru. Magnetic field flow interactions in a miniature electric power transformer with magnetic nanofluid core and solenoid type coils. *The journal Revue Roumaine des Sciences Techniques*, pages 25–34, 2013.

[179] L. Pislaru-Danescu, A. M. Morega, M. Morega, V. Stoica, O. M. Marinica, F. Nouras, N. Paduraru, I. Borbath, and T. Borbath. Prototyping a ferrofluid-cooled transformer. *Industry Applications, IEEE Transactions on*, 49(3):1289–1298, 2013.

[180] D. J. Tritton. *Physical Fluid Dynamics*. Oxford Science Publ. Clarendon Press, 1988.

[181] H. W. Müller and A. Engel. Dissipation in ferrofluids: Mesoscopic versus hydrodynamic theory. *Phys. Rev.*, 60(6):7001–9, 1999.

[182] T. Tynjälä. *Theoretical and Numerical Study of Thermomagnetic Convection in Magnetic Fluids*. Thesis, Department of Energy and Environmental Technology, Lappeenranta University of Technology, Lappeenranta, 2005.

[183] S. Banerjee, A. Mukhopadhyay, S. sen, and R. Ganguly. Thermomagnetic convection in square and shallow enclosure for electronics cooling. *Numerical Heat Transfer*, 55:931–951, 2009.

[184] T. L. Bergman, A. S. Lavine, Incropera F. P., and D. P. Dewitt. *Fundamental of Heat and Mass Transfer*. Johm Wiley & Sons, Inc., 2011.

[185] J. H. Lienhard IV and J. H. Lienhard V. *A heat transfer textbook*. Phlogiston Press, 2008.

[186] T. E. Faber. *Fluid Dynamics for Physicists*. Cambridge University Press, Cambridge, 1995.

[187] COMSOL Multiphysics ®. User's Guide, Version 4.4, November 2013.

[188] E. Guyon, J.-P. Hulin, L. Petit, and C. D. Mitescu. *Physical Hydrodynamics*. Oxford University Press, 2001.

[189] A. Jennings. *Matrix Computation for Engineers and Scientists*. Wiley, Chichester, 1977.

[190] C. A. J. Fletcher. *Computational Techniques for Fluid Dynamics*. Springer-Verlag, Berlin Heidelberg New York, 2nd edition, 1991.

[191] T. von Larcher and C. Egbers. Experiments on transitions of baroclinic waves in a differentially heated rotating annulus. *Nonlinear Processes in Geophysics*, 12(6):1033–1041, 2005.

[192] G. M. Carlomagno and G. Cardone. Infrared thermography for convective heat transfer measurements. *Experiments in Fluids*, 49(6):1187–1218, 2010.

[193] D. de Vahl Davis. Natural convection of air in a square cavity a bench mark numerical solution. *International Journal for Numerical Methods in Fluids*, 3:249–264, 1983.

[194] FLIR ®. DATA Sheet FLIR T620bx, April 2016.